Qualitative-portable to quantitative-laboratory LIBS

Jozef Rakovsky

▶ **To cite this version:**

Jozef Rakovsky. Qualitative-portable to quantitative-laboratory LIBS. Other. Université de Bourgogne, 2012. English. NNT : 2012DIJOS031 . tel-00825462

HAL Id: tel-00825462

https://theses.hal.science/tel-00825462

Submitted on 23 May 2013

HAL is a multi-disciplinary open access archive for the deposit and dissemination of scientific research documents, whether they are published or not. The documents may come from teaching and research institutions in France or abroad, or from public or private research centers.

L'archive ouverte pluridisciplinaire **HAL**, est destinée au dépôt et à la diffusion de documents scientifiques de niveau recherche, publiés ou non, émanant des établissements d'enseignement et de recherche français ou étrangers, des laboratoires publics ou privés.

UNIVERSITE DE BOURGOGNE
Laboratoire Interdisciplinaire Carnot de Bourgogne
et
COMENIUS UNIVERSITY
Faculty of Mathematics, Physics and Informatics

THÈSE
Pour obtenir le grade de
Docteur de l'Université de Bourgogne
Discipline : Physique
par

RAKOVSKÝ Jozef

24/09/2012

Qualitative-portable to quantitative-laboratory LIBS

Directeur de thèse
MUSSET Olivier
et
VEIS Pavel

Jury
M. MATEJČÍK, Štefan, Professeur, Président du jury
M. KANICKÝ Viktor, Professeur
M. MUSSET Olivier, Maître de conférence
M. NOGA Jozef, Professeur
M. PEDARNING Johannes, Professeur
M. UHER Pavel, Professeur
M. UHEREK František, Professeur
M. VEIS Pavel, Professeur

Acknowledgements

I would like to gratefully acknowledge the helpful efforts of all my colleges both in Bratislava and in Dijon. In particular I would like to thank my supervisors assoc. prof. Olivier Musset and prof. Pavel Veis for sharing of their knowledge and experiences during my PhD.

I thank my family, friends and Nelinka.

Préface

La spectroscopie sur plasma induit par laser (LIBS) propose une possibilité d'analyse rapide des composants de la matière sans préparation des échantillons. Pour cette raison, elle est attractive dans tous les cas où la détection des composants rapide sans préparation est exigée. Comme dans d'autres domaines, le progrès technique et scientifique perfectionne et diffuse de différents équipements et appareils fondés sur la méthode de LIBS. La spectroscopie résolue en temps est fournie par le spectrograph équipé d'une caméra rapide à l'aide duquel les spectres à large bande peuvent être obtenus dans une seule exposition par les spectromètres à large bande. Des sources laser plus petites et moins lourdes avec des spectromètres compacts peuvent être installées dans un appareil portable qui permet une utilisation à l'extérieur. Les ordinateurs proposent un traitement des données rapide. Installé sur le prochain rover de NASA destiné pour l'exploration de la planète Mars, l'instrument nommé ChemCam représente un exemple particulier de la haute technologie de LIBS appliquée. Néanmoins, il reste toujours des défis dans ce domaine et nous espérons donc que la thèse présente sera utile pour ceux qui s'intéressent à la LIBS.

Le projet de la thèse représente une collaboration entre le Département de la physique expérimentale à l'Université Comenius à Bratislava et le Laboratoire interdisciplinaire Carnot de Bourgogne de l'Université de Bourgogne à Dijon. L'objectif de ce projet était de réunir les expériences de ces deux laboratoires : l'expérience de la construction de laser de Dijon avec celle de la spectroscopie de Bratislava. Ces deux expériences sont fondamentales pour LIBS.

A Bratislava, le travail a été dirigé par le prof. Pavel Veis et il s'est concentré sur LIBS dans les conditions de laboratoire. La spectroscopie résolue en temps à bande large a été utilisée dans la recherche. Pour obtenir des spectres exigés, la réponse spectrale du système optique a été déterminée ce qui a été utilisé plus tard pour les corrections. La recherche du phénomène

d'auto-absorption a commencé dans la dernière période du travail, avec le but d'utiliser ce phénomène, généralement conçu comme négatif, pour déterminer les composants de la matière.

A Dijon, le travail a été dirigé par Dr. Olivier Musset et il a été orienté vers le développement de l'appareil de LIBS utilisable à l'extérieur. Un petit laser qui avait été développé dans le laboratoire a été implanté dans cet appareil. Le développement a été terminé avec succès et c'étaient les mesures de test qui ont été effectuées dans la dernière partie de la thèse présente. Les échantillons géologiques ont été utilisés pour tester l'appareil portable. Ces tests ont été effectués dans une coopération étroite avec les géologues.

Le premier chapitre présente une introduction de base sur LIBS. Elle est divisée en plusieurs parties concernant le plasma induit par laser, le claquage introduit par laser et l'évolution de plasma après le claquage. Il y a aussi une partie sur l'équilibre thermodynamique local incorporée dans le texte. Cette partie décrit l'importance de LTE et les possibilités de la détermination de cet état.

Le deuxième chapitre aborde le développement de l'appareil portable de LIBS. Dans l'introduction, de différentes sortes d'appareils de LIBS sont présentés ainsi que leurs usages possibles. Par la suite, l'appareil portable de LIBS développé à Dijon est décrit successivement, avec les caractéristiques brèves du software développé. Des usages possibles de cet appareil ainsi que ses limites sont présentés dans la dernière partie de ce chapitre en considération des résultats obtenus pendant les mesures de test.

Le troisième chapitre traite les applications possibles d'appareil de LIBS créé dans le laboratoire. Le processus de la réponse de mesure spectral et ses résultats sont présentés et utilisés par la suite dans les parties suivantes dans le processus de la détermination des paramètres de plasma. Les composants des échantillons utilisés ont été déterminés par la méthode sans calibration et cela avec l'objectif de choisir une location dans le plasma où les résultats soient les plus représentatifs.

Le dernier chapitre porte sur le phénomène d'auto-absorption. Un modèle simple et une théorie de base y sont présentés avec la proposition d'usage positif possible de ce phénomène. Une expérience simple et ses résultats sont présentés à la fin de ce chapitre. Finalement, il y a des discussions sur des possibilités et des perspectives de la méthode proposée.

Preface

Laser Induced Breakdown Spectroscopy (LIBS) offers possibility for fast detection of sample composition without its preparation. For this reason it is attractive anywhere where the fast detection and no sample preparation are needed. As in many other branches the technical and scientific progress improves and spreads the possibilities of LIBS based devices and laboratory apparatuses. The time-resolved spectroscopy is allowed by spectrograph equipped with fast camera, broadband spectra can be acquired in single exposition by broadband spectrometers. Smaller and lighter laser sources together with compact spectrometers can be implemented to portable device and can be used out of laboratory. Computers offer quick data processing. The device named ChemCam installed on the NASA's next Mars rover, curiosity, is good example of high technology application in LIBS. However, there are still challenges and we hope that this work will be fruitful for anyone who is interested in the LIBS.

The project of presented thesis was performed as a joint supervision project between the Department of Experimental Physics at Comenius University in Bratislava and Laboratiore Interdisciplinaire Carnot de Bourgogne at Université de Bourgogne in Dijon. The aim of the project was to join experience from both laboratories, experience in laser constructions from Dijon and experience with spectroscopy from Bratislava. The both are essential for LIBS.

In Bratislava the work was coordinated by prof. Pavel Veis and it was focused on LIBS under the laboratory conditions. The time-resolved broadband spectrometry was used in the research. In order to achieve required spectra, the spectral response of the optical system was determined which was later used for the corrections. The research of self-absorption phenomena started in the last period with aim to use this effect, usually considered as negative, for the composition determination.

In Dijon the work was supervised by Dr. Olivier Musset and directed toward development of LIBS device which could be used out of laboratory. The small

laser which was previously developed in the laboratory was implemented in the device. The development was successfully finished and testing process began in the last period of the thesis. The geological samples have been used for the testing process which was performed in deep cooperation with geologists.

The first chapter comprises a brief introduction to LIBS. It is divided into some parts about laser induced plasma, laser induced breakdown and evolution of the plasma after breakdown. The section dealing with local thermodynamic equilibrium is also included. The section describes importance of LTE and the possibilities to determine this state.

The second chapter is dedicated to the developed portable LIBS device. In the introduction, different type of LIBS devices are presented with their possibilities. Then the portable device developed in Dijon is described part by part with brief characteristic of developed software. The device possibilities and limits are sketched in the last section of the chapter with respect to results obtained in the testing process.

The third chapter deals with capabilities of LIBS apparatus which was set up in the laboratory. The process of spectral response measurement and its results are presented and consequently used in next sections in process of plasma parameters determination. The composition of used samples are determined by using of calibration free method with aim to choose proper location in the plasma for which results are the most representative.

The last chapter includes introduction to the subject of self-absorption phenomena. The simple model and basic theory are presented with suggestion how to use the phenomena in positive way. The simple experiment and its results are presented at the end of the chapter together with discussion about the possibilities and perspectives of the suggested method.

Contents

List of Figures

List of Tables

Chapter 1

Laser Induced Breakdown Spectroscopy

1.1 Introduction

Laser Induced Breakdown Spectroscopy (LIBS) or Laser Induce Plasma Spectroscopy (LIPS) is method used to determine the composition of investigated samples. There are lot of methods capable of determining the sample composition like OES ICP, MS ICP, analyses based on XRF, NMR or EPR, chemical analyses and so on. Some of them observe the radiation coming from the plasma which contains sample's species. For example in the case of the popular OES IPC the plasma is formed and sustained by delivering energy from the alternating current, which is producing a magnetic field absorbed by plasma. The plasma is produced in the gas where transportation of sample atoms was done somehow previously. The radiation from the plasma can be then analysed by its dispersion in the spectrometer and then atomic emission lines of sample atoms can be recognised and identified.

In the LIBS the source of energy for the plasma creation is not alternating current but high power laser pulse. Such a pulse is generated by pulsed laser focusing a pulse onto sample surface (see fig.1.1). On the surface density of the pulse power is high enough to start breakdown and to create free electrons. Free electrons absorb the rest of the laser energy via inverse bremsstrahlung phenomena and create laser induced plasma (LIP). This processes are accompanied by removing of small amount of sample material (ablation) causing a crater creation. Removed material compose the plasma and its radiation thus contains characteristic atomic and ionic emission lines of the sample's species. The lines can be identified and composition of the sample can be determined.

As it can be seen the preparation of sample and plasma creation is done in the same step. The special sample preparation is not needed.

The simplicity of LIBS apparatus and almost no sample preparation is big advantage in comparison to other analytical methods, but there are also some drawbacks. As sample preparation and plasma generation is done by the same laser pulse, stoichiometry of plasma is not necessary same as the stoichiometry of the sample. If one try to make quantitative composition determination from emission lines it is not sure that it is the right one. This is usually referenced as matrix effect and this is big challenge in LIBS community. Additionally some processes inside the plasma can negatively influence emission lines intensities. So the intensities are not longer proportional to concentration of the element in the plasma and not even in a sample. Such a process, for example, is self-absorption phenomena.

LIBS with respect to no sample preparation and an apparatus simplicity has big benefit especially in a conditions where sample preparation is very difficult or impossible to perform with regard to needed results. The industrial usage is frequently very profitable because of the price and rapidity of the method. Fast lasers, computers and small portable spectrometers development in last 20 years are hopeful for the LIBS portable device application and on-site measurements. Such a device can be really light and portable. This topic is described in chapter 2 with presentation of portable device developed in our laboratory with some application and its results.

There are thousands of publicised articles about LIP and LIBS and a couple of books [86, 72, 26, 94, 62] which summarize contemporary knowledges and experiences in the LIBS.

1.2 Laser Induced Plasma

Very soon after the first laser development by T.H.Maiman in 1960 [67] the breakdown similar to spark's was observed in the location where laser light was focused [18, 31]. Such a phenomena is called Laser Induced Breakdown (LIB) and in [86] it is defined as generation of practically totally ionized gas by the end of pulse. Generally, to consider ionized gas to be plasma it should fulfil an equation

$$N_D = \frac{4\pi}{3} h^3 n_0 \geq 1 \tag{1.1}$$

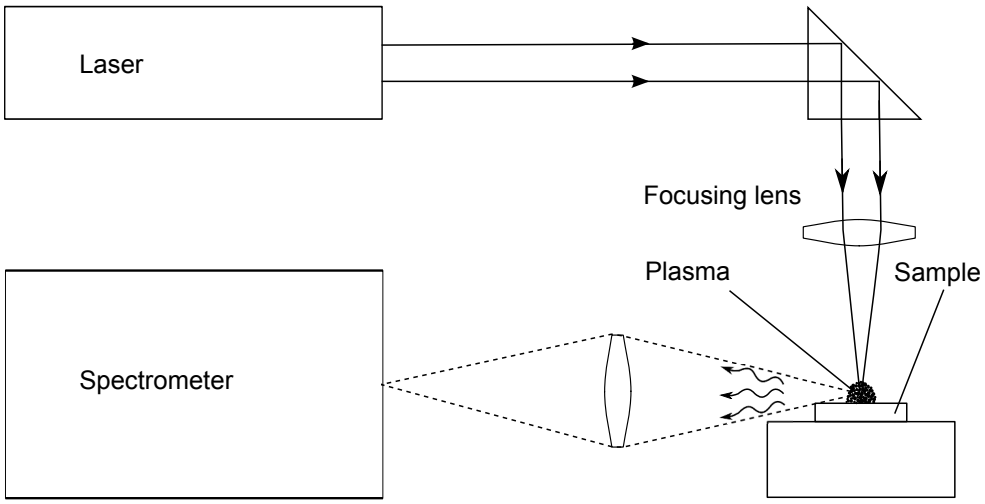

Figure 1.1: Scheme of LIBS apparatus.

where n_0 (m^{-3}) is the concentration of electrons and ions pairs and h is Debye length which can be evaluated by expression

$$h = \sqrt{\frac{\varepsilon_0 k T_e}{e^2 n_0}} \tag{1.2}$$

where T_e (K) is the electrons temperature, ε_0 is permittivity of vacuum, k is Boltzmann constant and e (C) is elementary charge. Satisfying of the expression 1.1 means that ionized gas is ideal plasma and Debye-Hückel theory about the shielding of ions by electrons inside of ionized gas is valid [69]. In figure 1.2 the border between the ideal and non-ideal plasma can be seen with respect to density and temperature of electrons. Plasma is ideal or non-ideal above or below line respectively. For common LIP, the temperature and the density of electrons satisfy expression 1.1 and so it is considered to be ideal plasma.

1.3 Laser Induced Breakdown

Energy distribution to LIP as well as to an other type of discharges comes from free electrons which gain kinetic energy from electromagnetic field. The free electrons can be generated in the LIP by two different ways:

- by Multiphoton ionization effect (MPI)
- by collisions electrons with neutrals

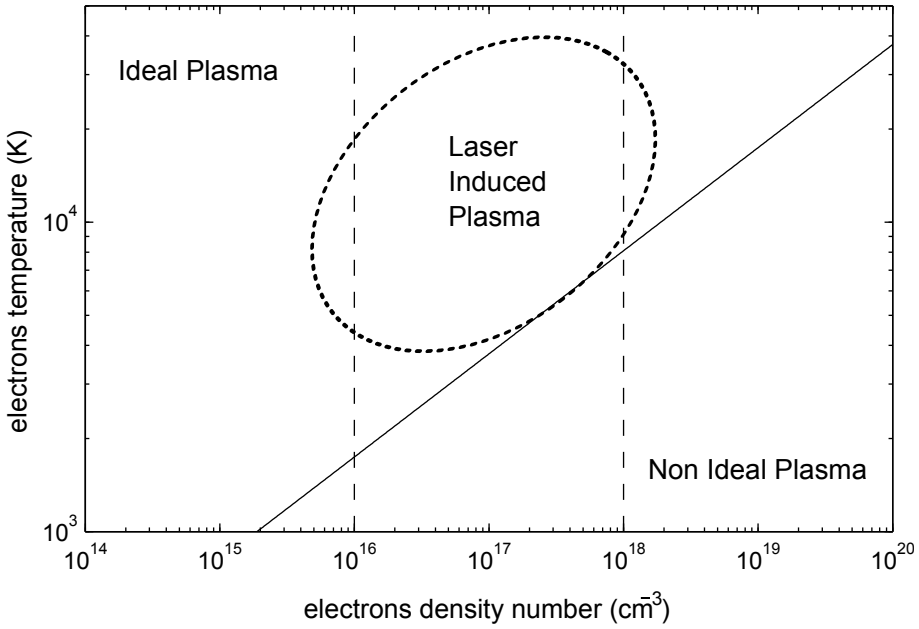

Figure 1.2: Ideal and non-ideal plasma with respect to the density number and temperature of electrons. The LIP plasma marked by circle is ideal plasma.

If we calculate the energy of the photon for common used Nd:YAG laser lasing on wavelength 1064 nm by using equation

$$E = h\frac{c}{\lambda} \tag{1.3}$$

where h is Plank's constant, c is speed of light in the vacuum and λ is wavelength, we get energy of 1.17 eV. The photon energy is not enough high to ionize atoms by its absorption[1]. Even by multiplying of basic laser frequency with 4th harmonics generator to obtain photons on wavelength 266 nm with the energy 4.16 eV, it is not possible to ionize most of atoms in the periodical table immediately by absorption. But by absorption of more photons by one electron via MPI it is possible to ionize atoms even by photons with energy lower than the ionization energy. Such a process is described by the reaction:

$$M + mh\nu \rightarrow M^+ + e \tag{1.4}$$

where m is the number of absorbed photons by one electron to create ion-electron pair. For Nd:YAG laser with wavelength 1064 nm absorption of 12 photons is needed to ionize nitrogen [12] and such a process has very low

[1]Cs and Fr are elements with lower ionization energy with values 3.8939 and 4.0727 eV respectively [76]

probability.

The collisional ionization is process when electrons with kinetic energy which is high enough collide inelastic with neutral atoms resulting in ion and free electron production, what is described by equation:

$$M + e \rightarrow M^{+} + e + e \tag{1.5}$$

If there is a source of the energy for electrons the process expand exponentially and becomes a cascade ionization. Such a type of ionization is usually observed in the classic discharges like glow discharge where electrons are accelerated by electric field coming from electrodes supplied with high voltage. In case of LIP the situation is different and more like in arc discharge where the electrons are thermalized and some amount of them coming from end of energetic distribution function have thermal kinetic energy high enough to ionize atoms.

It is clear that the collisional type of ionization needs primary seed electrons which will produce further electrons via collisions. Usually the seed electrons are produced by cosmic rays or by radiation from natural radioactivity in common discharges. In LIP the seed electrons for cascade ionization can also be generate by MPI or by thermal ionization. The thermal ionization is only possible in solid samples or in the gas contaminated by small particles as it was presented in [63]. The irradiation threshold 3.10^9 Wcm^{-2} was reached in the air without the particles in contrast to lower irradiation threshold 10^8 Wcm^{-2} with the particles. As was proved the natural dust in the air helps to induce the breakdown.

The laser induced breakdown can be very complicated and can be composed of the mentioned or other effects. Generally gas breakdown threshold irradiation value is higher then the threshold value in solids or liquids. In all this work LIP is assumed to be induced on the solid surfaces, where typical values of used irradiances for plasma generation are in range 10^8–10^{10} Wcm^{-2}.

1.4 Evolution after breakdown

There are free electrons in a plasma volume after breakdown. If not all energy of the laser pulse was consumed in the breakdown phase and if pulse is lasting after breakdown, free electrons absorbs the rest of pulse energy by inverse Bremsstrahlung. By this process the plasma heats up which leads to further ionization and to rising of electron concentration. The concentration is not going to rise infinitely and will stop when it becomes as high as critical

concentration described by the equation

$$\omega_p = \sqrt{\frac{e^2 n_0}{\varepsilon_0 m_e}} \tag{1.6}$$

where ω_p (Hz) is plasma frequency, e is elementary charge, ε_0 is permittivity of vacuum, m_e (kg) is electron mass and n_0 is concentration [69]. The critical concentration is considered as the concentration in which plasma frequency is above certain value. Above the value, plasma starts to be no longer transparent for incident light of laser. An useful expression for evaluation of such a concentration from the incident wavelength is:

$$n_c = \frac{10^{21}}{\lambda^2} \tag{1.7}$$

where λ is in microns and n_c is in cm^{-3} [69]. Because of plasma shielding the laser pulse is not able to reach the sample surface and lower parts of plasma any more. The spreading of plasma toward laser direction starts. As it can be seen the high energies in pulses do not necessarily eventuate to better plasma quality and can lead to wasting laser power or in worst case to unwanted plasma properties like low correlation between the plasma and sample composition.

A shock wave is formed after breakdown whose velocity was measured in [70] with value described by expression:

$$v(t) = \frac{2}{5}\left(\frac{E}{\rho}\right)^{\frac{1}{5}} t^{-\frac{3}{2}} \tag{1.8}$$

where E is proportional to the energy generating the shock wave and ρ is density of gas.

The shock wave power determine whether absorption zone will be generated by the shock wave or not during the plasma formation. If irradiance in air is higher then 8.10^8 Wcm^{-2}, the shock wave is able to ionize air high enough to produce electrons densities to reach the critical concentration [86]. With the critical concentration incoming laser pulse will be absorbed by this upper part of plum feeding father strong shock wave propagation and avoiding laser pulse to reach inner part of plasma. This regime of LIP formation is called laser-supported detonation (LSD).

If the irradiance is lower then value set forth above, plasma formation is different. Plasma formation starts in the vapours at the sample surface and continues with extension toward laser by gaining energy from inverse

Bremsstrahlung from laser pulse. But the shock wave is not strong enough to ionize ambient gas to level needed for absorption. So the shock wave is separated from the plasma and the laser reaches inner parts of plasma and can supply the energy for farther heating. Plasma expands and acts as piston to surrounding gas and mostly contains atoms from initial phase of the plasma formation [9]. The regime is usually referenced as laser-support combustion (LSC).

LSC is more suitable for LIBS application then LSD because composition of formed plasma is more probably representative in respect to sample composition.

1.5 Local Thermodynamic Equilibrium

Generally, for determination of atomic state distribution function (ASDF) in a plasma, all collisional and radiative processes with their rates have to be known. So the following collisional processes must be considered: collisional excitation and deexcitation, collisional ionization and three body recombination; and these radiative processes: photo-excitation, radiative decay and Bremsstrahlung process. If state of plasma can be fully or partly described by only macroscopic parameters (temperature, electron density), ASDF determination is not so complicated. Whether it is possible usually depends on a density number of electrons.

If the density of electrons is high enough, the collisional processes with electrons would prevail over the radiative processes, so equilibrium can be established and the temperature of the plasma can be defined. This state is referenced as local thermodynamics equilibrium (LTE). In such a state, probability of the excitation and deexcitation of plasma species is much more probable to be provided by collisions with electrons then by absorption or emission of photon. The LIP are generally considered to be in LTE however it is recommended to consider every experiments separately. LTE in LIP is desired because of possibility to express ASDF, necessary, for example, in composition and temperature determination in calibration free LIBS (CF-LIBS) (see section sec:CFLIBS).

Let us assume that all possible excitation end deexcitation process are in equilibrium expressed by equation

$$n_i \rho B_{ik} + n_i n_e C_{ik} = n_k \rho B_{ki} + n_k A_{ki} + n_k n_e C_{ki} \tag{1.9}$$

where ρ is radiation density and C_{ik}, C_{ki} are excitation and deexcitation collisional rates respectively, B_{ik}, B_{ki} and A_{ki} are Einstein's coefficients and n_i, n_k are populations of upper and lower states respectively. For low radiation density ρ we obtain that ASDF will be determined wholly by electrons collision, if

$$n_e \gg \frac{A_{ki}}{C_{ki}} \tag{1.10}$$

So if collisional deexcitation is much faster that spontaneous radiative deexcitation process, ASDF will obey Boltzmann distribution 3.2. The temperature of ASDF will be equal to the kinetic temperature of electrons described by Maxwell's distribution function for electron's velocities. The collisional rates can be calculated from expression

$$C_{ik} = n_e \left\langle v_e \sigma_{ik} \right\rangle \tag{1.11}$$

where v_e is incident velocity of electrons and σ is collisional cross-section which can be expressed by Born approximation as

$$\sigma_{ik} = \frac{2\pi^2}{\sqrt{3}} \frac{f_{ik}\overline{g}e^4}{\frac{1}{2}m_e v_e^2 \Delta E_{ki}} \tag{1.12}$$

where f_{ik} is absorption oscillator strength and $\overline{g}$ is effective Gaun factor usually determined empirically [104] and ΔE_{ki} is energy needed for transition. The spontaneous emission transition probabilities A_{ki} can be expressed by

$$A_{ki} = 8\pi^2 \frac{f_{ik}e^2 \Delta E_{ki}^2}{h^2 m_e c^3} \frac{g_k}{g_i} \tag{1.13}$$

where g_k and g_i are upper and lower state degeneracy respectively. Above expressions can be used for electron density number estimation needed for LTE [99, 29]. The final expression is usually referenced as McWhirter criterion and can be written as

$$n_e > 1.6 \cdot 10^{12} \sqrt{T} \Delta E_{ki} \tag{1.14}$$

where n_e is electron density number (cm^{-3}), T is temperature (K), and ΔE_{ki} is the highest energy difference (eV) for two adjacent levels which are considered. So if electron density number is high enough to satisfy McWhirter criteria, than plasma is in LTE.

For higher atomic energy levels closer to continuum, the energy gap is decreasing which causes in expression 1.12 increasing of the collisional rate. In contrast, emission rate is decreasing with the lower energy gap 1.13. So it is

easier to satisfy higher states level to be in LTE. Additionally if the expression 1.14 can be fulfilled for certain energy level and higher but not for lower, then such a plasma is referenced to be partly in LTE (pLTE).

It is worth to note that the McWhirter criterion is valid for homogeneous and static plasmas, so its applying to LIP without further consideration is not the guarantee of LTE. The problem is described more in detail in [45] and especially for LIP in the [29] and will be shortly discussed.

It is clear that the relaxation times for the processes which control equilibrium must be much more faster than characteristic time for thermodynamic parameters of plasma like temperature and electron density. So even if McWhirter criteria is fulfilled, if the electron density number change in time shorter than time needed for relaxation of atoms, the plasma is not any more in LTE. For assessing of LTE in plasma additional criteria must be considered. For the temperature T and electron density n_e the following expressions must be fulfilled:

$$\frac{T(t) - T(t + \tau_{rel})}{T(t)} \ll 1; \ \frac{n_e(t) - n_e(t + \tau_{rel})}{n_e(t)} \ll 1 \tag{1.15}$$

where τ_{rel} is time needed for relaxation to establish ionization end excitation equilibria [29]. The fulfilment of the above can be decided by comparison of time for the slowest collisional reaction with the characteristic time of thermodynamic plasma parameters.

For estimating the characteristic time, three different times can be considered, coming from three different phases of LIP evolution. The first one is breakdown, the phase with very fast evolution, with the times much shorter than that needed for the relaxation. Also ionization degree is high causing that Saha equation is not describing ion concentrations in the plasma. Next evolution stage is plasma expansion, when the plasma is not any more fed with laser pulse energy. In this stage the plasma is cooling mainly because of expansion but it is also referenced as not being in the LTE. The conclusion is based on equal or higher recombination times than the time for the plasma plum expansion.

When plasma expansion stops, plasma is cooled mainly by cold particles coming from plasma border. The process is slower than one in the expansion phase and can take longer time than the relaxation time of excitation and ionization processes. The slowest collisional process is collisional excitation from ground atomic state. So for estimation of the relaxation time expression

1.11 can be used

$$\tau_{rel} \approx \frac{1}{n_e \langle v_e \sigma_{12} \rangle} = \frac{6.3 \cdot 10^4}{n_e f_{12} \langle \bar{g} \rangle} \Delta E_{21} \sqrt{kT} \cdot e^{\frac{\Delta E_{21}}{kT}} \tag{1.16}$$

where both ΔE_{21} and kT are expressed in eV and n_e in cm^{-3} [29]. The expression is valid for complete ionization and must be multiplied by $N_{II}/(N_{II}+N_I)$ in case of partial ionization. The energy gap ΔE_{21} is related to first excited level of the resonance series which is the slowest one in collisional processes.

The above criteria was applied by Cristoforetti et al. in [30]. With aim to determine characteristic decay time of temperature and electron density spectra were acquired at various delay times ranging between 500 ns and 2 μs (gate ranging between 250 and 500 ns), allowing to calculate the temporal evolution of temperature and electron density and their decay times τ_T ($3.3 \cdot 10^{-6}$ s) and τ_{ne} ($1.5 \cdot 10^{-6}$ s). The lowest value among them was used for the computation. The relaxation time to reach equilibrium was estimated by the expression 1.16 to value $2 \cdot 10^{-9}$ s, $2.5 \cdot 10^{-5}$ s and $2.6 \cdot 10^{-5}$ s, for Al I, N I and O I respectively. The criteria is easily fulfilled for aluminium but is not fulfilled for nitrogen and oxygen atoms. So even if some element is in LTE some other element does not need to be in LTE even in the same location in plasma, so every component of plasma must be considered separately.

Because of inhomogeneity of plasma induced by laser pulse additional criteria must be considered to asses LTE. The disturbance of LTE in the inhomogeneous plasma is caused by strong gradients of thermodynamic parameters especially in the edge region of plasma. The consequence of this is diffusion of particles and so disturbance of the local parameters. The following expression have to be fulfilled for LTE

$$\frac{T(x) - T(x+\lambda_D)}{T(x)} \ll 1; \; \frac{n_e(x) - n_e(x+\lambda_D)}{n_e(x)} \ll 1 \tag{1.17}$$

where

$$\lambda = \sqrt{D \cdot \tau_{rel}} \tag{1.18}$$

is diffusion length in cm during the relaxation time [29]. For particles, the diffusion process with highest diffusion length is considered in inhomogeneous criteria and it is compared with plasma dimensions. The diffusion processes connected with resonance charge-exchange collisions are the process with the

highest diffusion coefficients [34] expressed by

$$D \approx 3 \cdot 10^{19} \frac{kT}{N_{II} M_A} \tag{1.19}$$

where kT is expressed in eV, and N_{II} is absolute number of density of ions in cm^{-3} and M_A is the relative mass ($M_H = 1$ for hydrogen atom). For evaluating the diffusion length λ by expression 1.18 the relaxation time τ_{rel} from the expression by 1.16 can be used.

From previous the importance of more critical attitude in LTE consideration, as only usage of McWhirter's criterion, is resulting. Additional two criteria should be used to asses LTE in LIP because of its transient and inhomogeneous character.

Chapter 2

Portable LIBS Device

2.1 Introduction

Portable LIBS devices and their on-site measurements possibilities are core topic of this chapter. Such a device has been developed in the laboratory at Burgundy University in Dijon in France, as a part of presented thesis.

The advantage of LIBS in comparison with other analytical methods is, that in most cases no sample preparation is required. Essentially, the sample is prepared by its ablation to an ambient atmosphere by the laser pulse. The apparatus are usually simple with two crucial devices. First one is a pulse laser for ablation, initiation of breakdown, and further heating of created plasma and second one is a spectrometer for spectroscopic analyse of radiation coming from the plasma. For data recording, its processing and laser-spectrometer synchronization some additional devices are needed. All the devices can be quite small, compact, and powered by batteries nowadays and hence implemented to transportable LIBS apparatus in order to provide on-site measurements. The transportable LIBS devices are usually divided to this three types:

- Stand of Detection LIBS
- Remote/Fibre-Optic LIBS
- Portable LIBS

They differ in dimensions, weight, in the way how they deliver the laser pulse to sample or how they collect radiation coming from plasma. Generally only the Portable LIBS can be transported by man itself.

The stand of detection device type is used where it is not possible reach sample to distance allowing to touch it. In such a condition the laser pulse

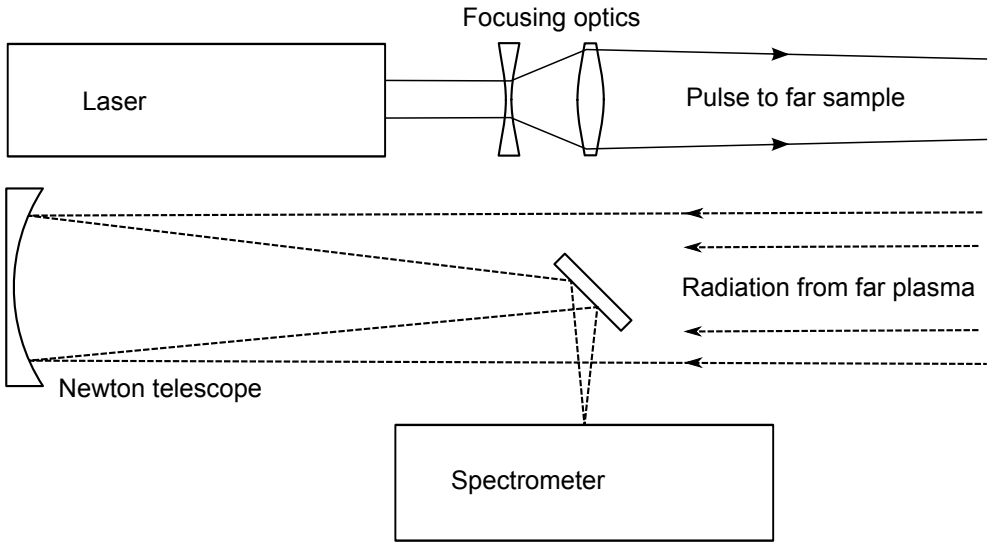

Figure 2.1: Stand off LIBS apparatus design.

must be delivered to long distance usually tens of meters through the air. Also the plasma radiation must be collected from the same distance. This gives higher demands on optics in device. First stand off LIBS measurement was performed on metals samples by Cremers [27] from distances 0.5 m to 2.4 m. Later, stand off LIBS devices for higher distances were presented [78], for the samples of environmental interest [65] and for cultural heritage ablation cleaning [46]. Using of double pulse excitation for hazardous materials detection was presented in [43]. Big goal for LIBS community is implementation of LIBS stand off device in Mars Science Laboratory on the rover Curiosity which will land on Mars on Aug. 6, 2012, Universal Time and Eastern Daylight Time [35, 25, 38, 60, 89, 107]. The device will be able to analyse samples distant up to 7 m from the rover.

Scheme of apparatus for the stand off LIBS is shown in figure 2.1. Collection of light is preformed by Newton telescope. The laser pulse is at first widened and then focused at far distance to the sample surface to create plasma.

In case of Remote/Fiber-Optic LIBS it is possible to reach sample and laser pulse is delivered to sample by fibre. The light from plasma is delivered to the device by fibre as well. The fibre can be long tens of meters so device itself can stay for example in a car and one can analyse samples around the car up to the distance of the fibre length [32, 28, 68, 37, 87, 109]. So the device with spectrometer and laser does not need to be so light and small as in the case of portable LIBS device.

The portable LIBS device is considered to have dimensions and weight al-

lowing it to be transported by man itself. In the year 1996 a compact suitcase system with weight 14.6 kg was presented [111]. The system was later used as a base for next one [105], which was used for geochemical analysis in [48, 47] and for hazardous material detection [33]. Few commercial portable LIBS systems are nowadays available on the market: Easy LIBS from IVEA©(which integrates the compact laser developed in our lab) [51], PL100-GEO from Applied Spectra© [82], LIBSCAN 25 from Applied Photonics© [2], Porta-LIBS-2000 from StellarNet Inc.© [110], and IDEALIBS from Bertin Technologies©. Most of them are heavy (up to 25 kg) and transportable rather than portable. In the lightest systems, lasers are either very expensive to attain high performance with reduced volume or if costs are lower, performance is reduced.

Next sections present portable LIBS device developed in Dijon's laboratory at Burgundy University at Laboratoire interdisciplinaire Carnot de Bourgogne. The device was created with aim to make it really transportable and as light and as small as it is possible, with ability to be used outside for couple of hours without external source of power. Testing measurements on geological samples are presented in the end of chapter.

2.2 Dijon's portable LIBS device

2.2.1 General description

A pulsed Nd^{3+}:YAG flash lamp laser, emitting at the fundamental wavelength of 1064 nm and actively Q-switched (with double pulse capability), was used as the laser source of the portable LIBS system (see [44] for more details about main characteristics). The energy distributed in one pulse is up to 40 mJ, with a duration time of 4.5 ns and a repetition rate up to 1 Hz. No advantage was recognized in applying a double pulse regime [11, 103] for our samples, so that the laser always operated in single pulse mode in the later presented experiment. As the beam quality M^2 is about 14, a telescope with a magnifying factor of 2 was used in combination with a focusing lens of short focal length of 50 mm. Such an optical arrangement produces a laser spot less than 500 μm (typically 350 μm) in diameter. Two crossed red laser beams, associated with four white LED lighting the sample surface, and a compact color camera, allow to the operator to choose the shot position. The radiation from plasma generated by the laser shot is collected with an aspheric lens (from Ocean Optics), directly coupled to a transport fibre. A small chamber is situated between the focus point of the laser and the collecting lens. This chamber is

Figure 2.2: Portable LIBS device developed in Dijon's laboratory.

separated from the laser arrangement by a fuse UV-silica plate. Two O-rings are placed between the sample and the chamber, and between the chamber and the silica window. This closed volume allows various gases, pressures and air flows to be used. As a consequence, this configuration notably improves shot-to-shot stability and signal intensity [36]. It also reduces optic contamination by removing dust produced by laser ablation.

All these optical elements are mounted within a gun-shaped box, designed for comfortable handling (see Figure 2.2). Two color screens are installed at the back of the gun. They display the laser settings and the picture from the camera. The 'laser gun' is connected by an umbilical to a second box containing the spectrometer, the batteries, a computer, a small pump, and a filter (see figure 2.3). Inside the umbilical, there is a fibre transmitting light to the spectrometer, space for exhausting the sample chamber, and several wires to power and control the laser. The spectrometer is a small Czerny-Turner Ocean Optics HR 2000+. Its bandwidth ranges from 200 nm to 650 nm in wavelength, with an optical resolution of 0.4 nm (spectral resolution of about 1000). It possesses triggering capabilities with minimal integration time of 1 ms. A single broadband spectrometer with low spectral resolution was preferred to several narrowband spectrometers with high spectral resolution in

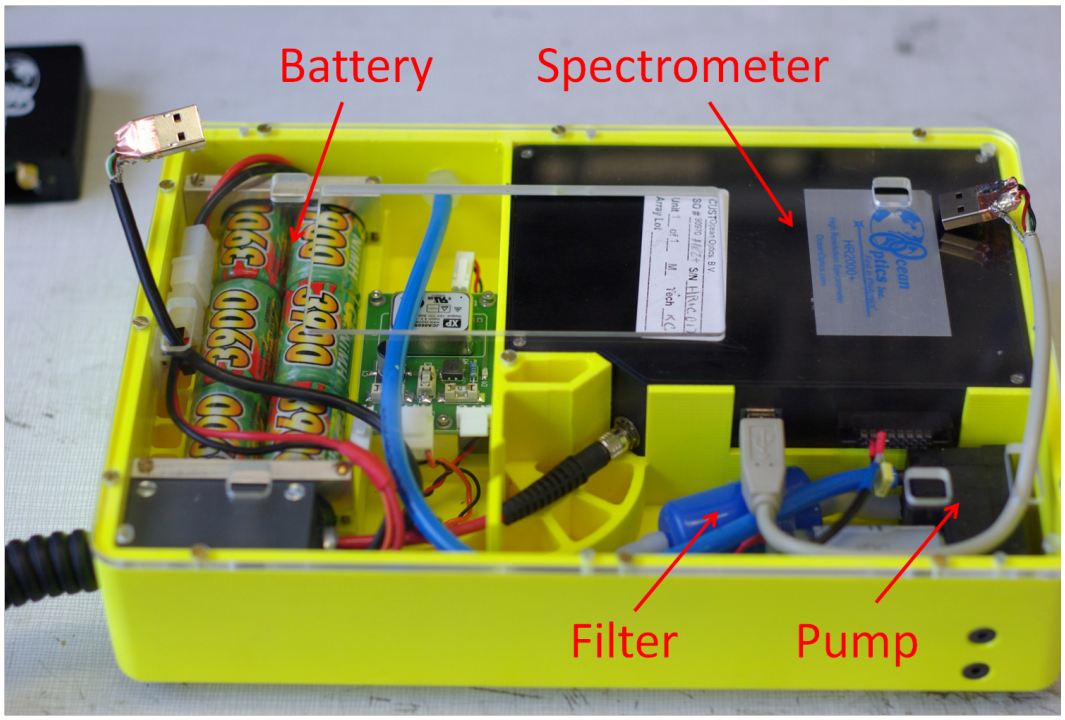

Figure 2.3: The part with spectrometer of the portable LIBS device.

order to maintain volume, weight and cost as low as possible. Our configuration offers a large spectrum allowing several elements to be measured. The overall control of the system is provided by a small touch screen computer. The software for acquisition and spectra processing was especially developed for this LIBS system. It provides automatic correction of the background, the thermal shift of spectral line positions, and the calibration of the spectrometer. It also possesses an automatic detection mode able to associate spectral lines to their corresponding chemical elements. The system is completely autonomous. Its working time is limited by the computer and the battery lifetime of about 6 hours. The total weight of the system is 5 kg.

2.2.2 Laser

The laser used in the portable LIBS device has Nd^{3+}:YAG crystal as active medium, which is optically pumped by flash lamp. The laser pulses are generated by modulating of resonator quality by so called quality switching (QS). The Pockel cell (PC) element is used for this purpose. PC is a crystal based on Pockel's electro-optic effect, therefore can be used as quarter-wave plate driven by high voltage. The scheme of laser set-up design is shown on the figure 2.4.

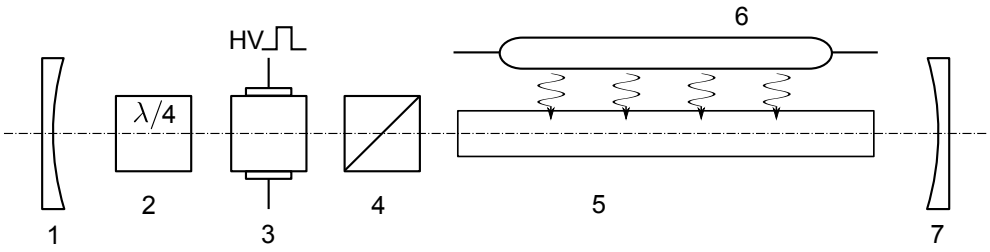

Figure 2.4: The set-up of laser used in the portable LIBS device with parts: 1-front mirror, 2-quarter-wave plate, 3-Pockel cell, 4-B Brewster polariser, 5-Nd:YAG crystal, 6-flash lamp and 7-rear mirror.

wave length	1064 nm
energy	40 mJ
pulse duration	4.5 ns
spot size	0.5 mm
irradiation	$4{\cdot}10^9$ W·cm^{-2}
repetition rate	1 Hz

Table 2.1: Typical laser values.

Working principle of the laser is following. When PC is without voltage it behaves like it being not there. So linearly polarised light after passing quarter-wave plate becomes circular polarized and when it pass it again after reflecting from the front mirror, it becomes linearly polarized again but in perpendicular direction as previously. Because of this it cannot pass the polariser, therefore oscillations will not start. But if PC is powered by high voltage it starts to behave like a quarter-wave plate and the polarization plane will be same as the polarization plane of polariser, therefore light can reach active medium and oscillations can start. The resonator will lase through the front mirror which is only partially reflecting (output coupler).

Two voltage pulses can be possibly generate and power the PC in order to generate two laser pulses for one flash lamp blink as it is depicted on figure 2.5. Energy distributed in the pulses varies in accordance to the delay between pulses. The delay of the second from first pulse must be in orders of 10 μs to be enough energy distributed in the second pulse.

Pumping energy evolution vs. output energy of the laser have been measured and it is shown in the figure 2.6. From the plot, it can be seen that saturation is reached at approximately 5 J of pumping energy with the output energy ≈45 mJ. The beam quality M^2 factor is ≈14 and beam diameter 3≈mm. The typical values under which the laser was used in the potable LIBS device for geological samples are summarized in table 2.1.

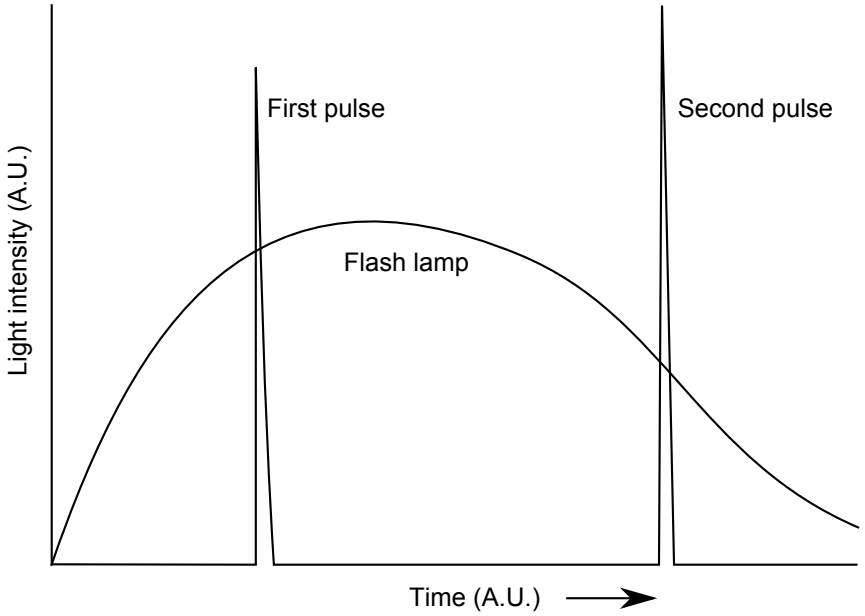

Figure 2.5: Double pulse regime of the laser.

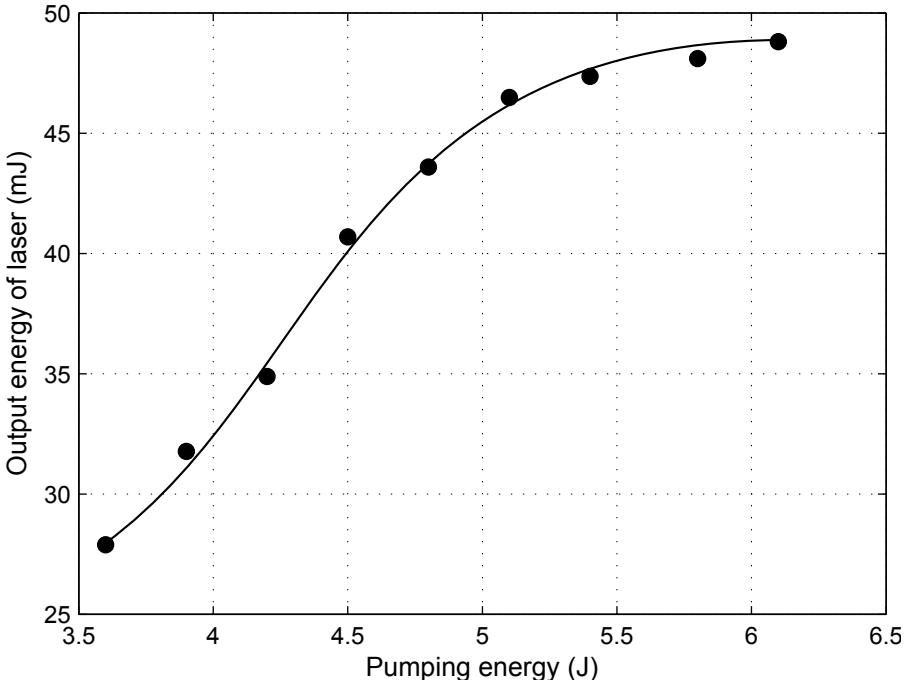

Figure 2.6: Pumping energy vs. output energy of the laser.

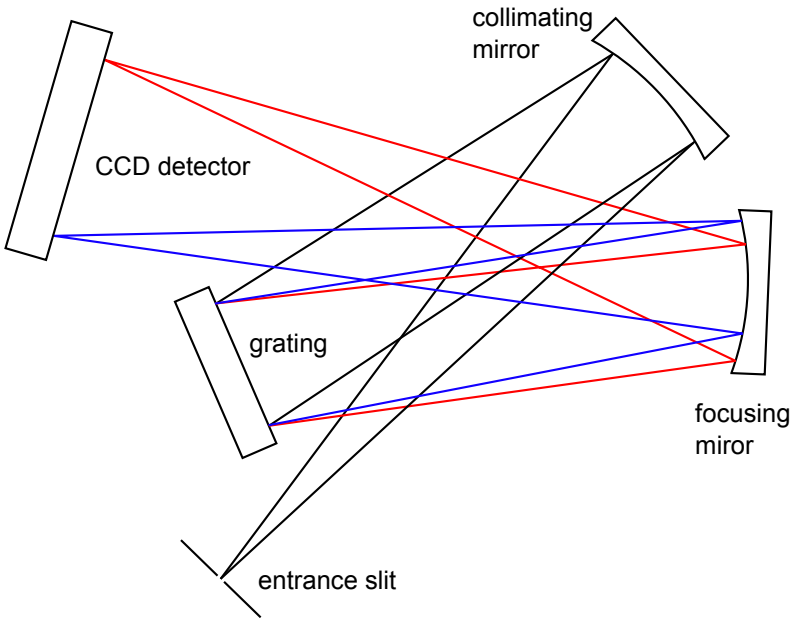

Figure 2.7: Crossed Czerny-Turner design used in the used HR 2000+ spectrometer.

2.2.3 Spectrometer

For the spectroscopic analyses the small compact spectrometer HR 2000+ from company Ocean Optics was used[77]. The spectrometer is implemented to the device as it is shown on figure 2.3. It is powered by the small computer used for acquisition and analysing of spectra. The spectrometer's spectral range is 200–650 nm and its resolution <0.7 nm. Minimal integration time for spectra acquisition is 1 ms.

The spectrometer is designed as symmetrical crossed Czerny-Turner optical design. The design scheme shown in the figure 2.7, where two different wavelength from border of the spectral range are presented by different color. The spectrometer's aperture is f/4 and focal length 101.6 mm. Linear silicon CCD-array with 2048 pixels and dimensions 14μm x 200μm is used as detector[81].

Figure 2.8 shows full width at half maximum (FWHM) of the instrument function measured for different emission atomic lines from three different light sources. As first source the HgCd low pressure discharge lamp was used. As second HeNe laser where only one line was obtained. And as third source, the LIP from different samples with no special criteria for choosing of the lines was used. In all cases lines have been fitted by Gaussian profile to estimate FWHM. Broadening of all lines is approximately same for same wavelength

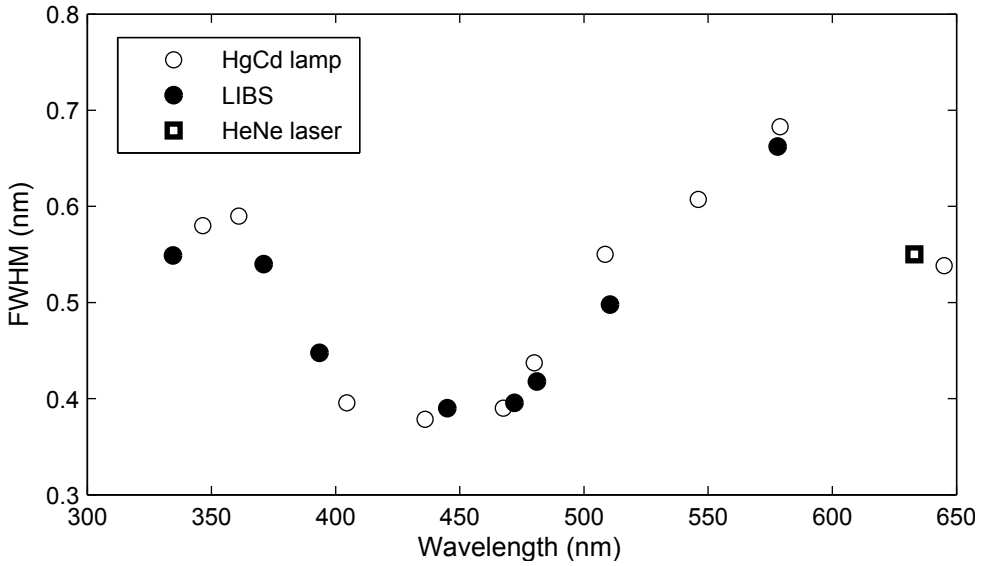

Figure 2.8: Instrument function FWHM of used spectrometer determined from different source of lines.

and is cause by convolution of instrumental function with real line profile. Even HeNe's and HgCd lamp's lines are narrow they are broadened equally as that coming from LIP spectra. So all broadening effects in LIP, like Stark or Doppler broadening are not distinguishable by the used spectrometer. The figure 2.9 shows comparison of spectra coming from the LIP acquired by two spectrometers with different resolution. In the spectra acquired by the compact one it is not possible to recognize Fe I and one Sr II lines. The self-reversal shape of Ca I line is not possible to recognized as well.

Additional drawback is exposed by long exposition time so it is not possible to make time resolvable spectra. The spectrometer's shortest exposition time is 1 ms. The characteristic time for LIP evolution is about 1–10 μs what is much more shorter than the exposition time. Hence the acquired spectrum is integrated through all the plasma evolution.

Because of thermal noise which is usually decreased by cooling of detector, the signal to noise ratio from the UV part of the spectral range, where the sensitivity of spectrometer is very low, is also very low. Because the noise is random signal its level can be decreased by averaging lot of spectra. The evolution of such a averaging is shown on the figure 2.10. Of course there is big difference in 1 and 50 number of averaged spectra, but it is not always possible to make accumulation of such amount of spectra from same point of the sample as it will be presented in section 2.4.2.

During the usage of the spectrometer problems with flowing of background

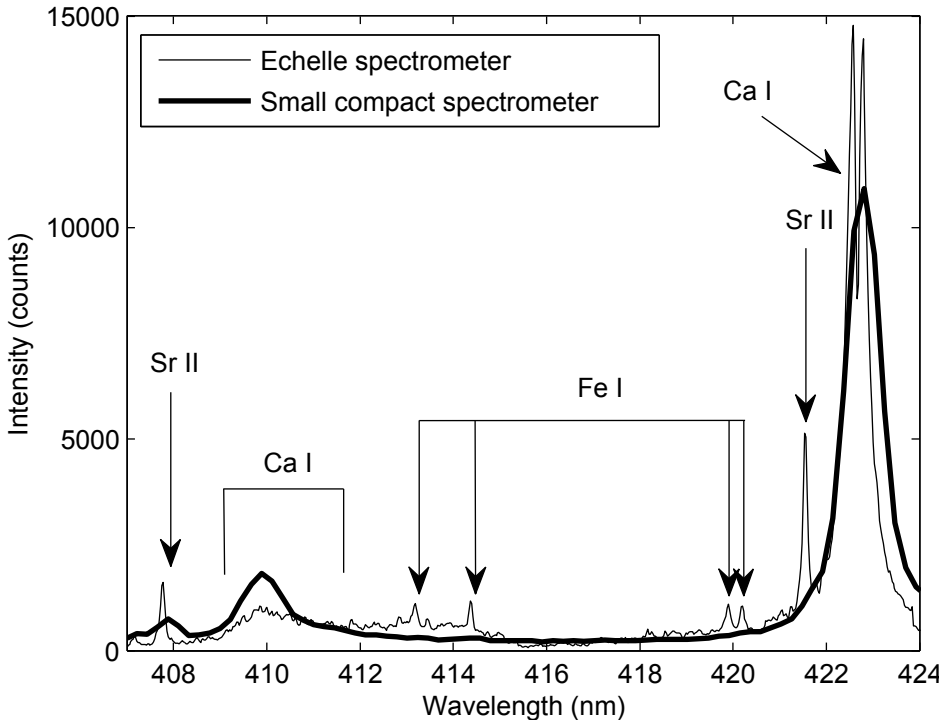

Figure 2.9: Comparison of spectra of same LIP measured by Echelle type spectrometer and small compact spectrometer used in the portable LIBS device.

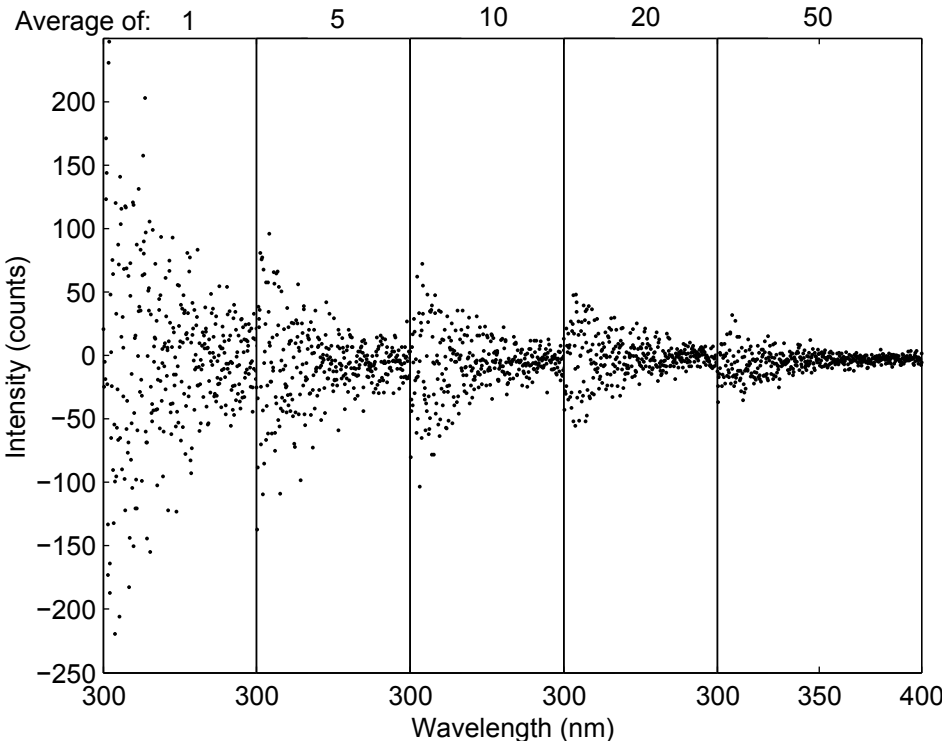

Figure 2.10: Evolution of noise in part of spectral range of the spectrometer with 1, 5, 10, 20 and 50 number of averages.

in time and strong shifting of lines wavelengths with temperature have been recognized. Both problems have been solved by developed software and will be described in next section 2.11.

2.2.4 Software

For comfortable on site usage of the developed portable LIBS device a software for acquisition and data processing was developed. LabView 9.0 development environment was used for this purpose. The software is optimized for screen resolution 1024 x 600 pixels, to resolution of the small laptop integrated to do device. Process of acquisition of spectra can be controlled and data visualized.

The presented software is registered and protected in France by The Agency for the Protection of Programs (Agence pour la protection des programmes - APP) under the name: *Logiciel ICB-LIBS de pilotage d'un système laser LIBS portable permettant l'acquisition, le traitement et l'analyse LIBS sur site* and under registration number (Inter Deposit Digital Number - IDDN): *FR.001.170003.000.S.P.2012.000.10800*. A brief software manual is presented in appendix B.

It is possible to display position of atomic emission lines for various elements. For this purpose Kurucz-Harvard [57] and NIST [75] atomic spectra database have been implemented. From the databases coefficient like transition probability for spontaneous emission, degeneracy and energy of upper state is used for theoretical intensity calculation. The temperature for corrections in accordance of Boltzmann distribution can be adjusted. So elements lines are not defined only by positions but also by the theoretical intensities presented with line height (see 2.11).

The correction of the spectrometer's spectral response is implemented in the software, therefore the lines in the spectra can be recognized more reliable, even of low spectrometer resolution. Figure 2.11a) presents theoretical positions and intensities of some Ti I lines indicated by vertical yellow lines. They are in a good agreement with experimental spectra, presented by white line. The theoretically calculated intensities not necessarily fit every experimental lines. Some lines can be affected by processes in the LIP resulting in unpredictable line intensities. The figure 2.11 illustrates such an example. While the Al I and Ca II theoretical intensities are in good agreement with measured spectra in the range shown in figure b)the different theoretical lines for Ca II from figure c) are much more higher the experimental lines. This can be caused by strong self-absorption. Because the Ca II lines from figure b) and c) emit

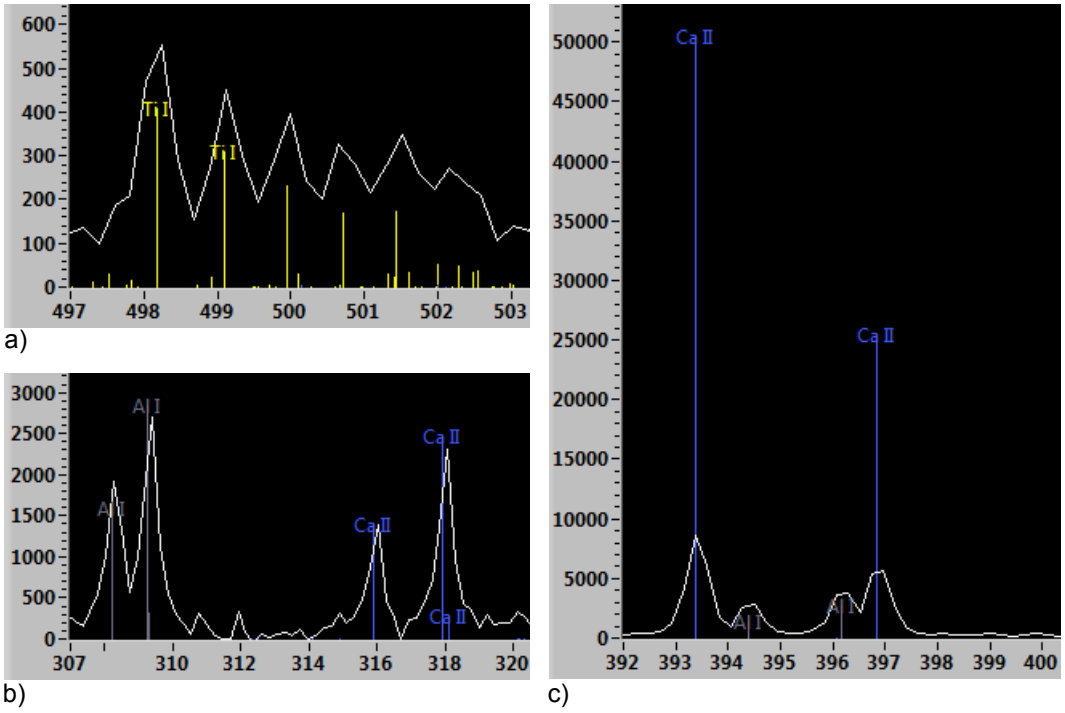

Figure 2.11: Screen shots from the software presenting the agreement of the theoretical lines with measured spectral lines calculated for temperature 10 000 K.

from different upper energy level, higher temperature (adjusted in program) can fit the theoretical to the experimental intensities. In the presented case we have set temperature to value 10 000 K but lines fit for temperature 15 000 K. The knowledge about the temperature value can help for spectral lines identification. But if transitions are from close energetic levels the temperature has low influence to relative intensity ratios as in case shown on the figure 2.11a) and b).

Figure 2.12 shows the part of the program responsible for correction of data from spectrometer. Because of background decreasing with time, the correction is needed and it is automatically subtracted by functions 1 and 2. Function 1 subtracts average of first 20 pixels from the linear CCD detector which are dark, and not used for spectra acquisition. Function 2 makes additional correction by subtraction of dark noise corrected by function 1. The dark noise waveform was obtained by averaging of 1000 dark noise spectra. The function 3 perform the spectral response correction of the spectrometer. It was derived from the spectral response of Echelle type spectrometer, with spectral response determined previously, as it is described in section 3.5.5.

The wavelengths positions in accordance of pixel numbers are assigned by

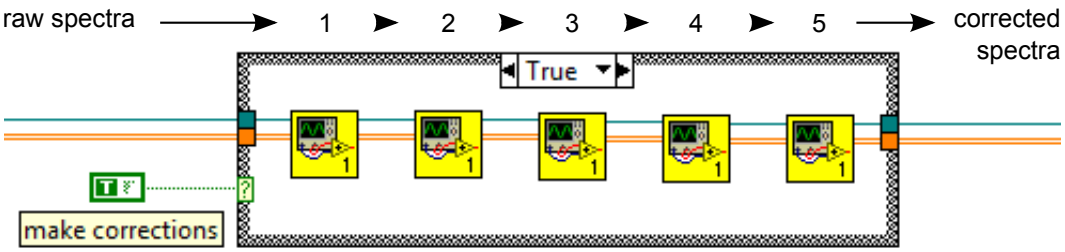

Figure 2.12: Part of program in LabView correcting raw spectra coming from the spectrometer.

the function marked as 4 (figure 2.12). The wavelength numbers to pixel numbers are associated by polynomial equation

$$\lambda_p = C_0 + C_1 p + C_2 p^2 + C_3 p^3 \tag{2.1}$$

where C_0, C_1, C_2 and C_3 are coefficients obtained in process of calibration by the fitting to know emission lines positions. As the coefficients are temperature dependent, calibration of the spectrometer before every measurement campaign or when temperature is changed is needed. Because the device is intend to be portable, with on-site measurement possibilities, the frequent calibration can be very uncomfortable. Therefore the automatic correction for spectra shifting have been implemented. Function of shift dependence vs. temperature was assumed to be polynomial:

$$\Delta\lambda = a_0 + a_1 p + a_2 p^2 \tag{2.2}$$

where coefficients a_0, a_1 and a_2 have been determined by fitting of measured peaks shifts for temperature range 20–37 °C. The value $\Delta\lambda$ is added to the values which are coming form the output of function marked as 3. The temperature is measured by sensor placed on the PCB (printed circuit board) of the spectrometer.

Last function perform restriction of spectral band with. Because very noisy UV part of spectra it is usually cut to range 300–650 nm.

Besides above mentioned properties of the software it is also able to automatically detect lines of elements, makes intensity calculation of selected peaks and providing they fit by Gauss, Lorentz or pseudo-Voigt profile. The pseudo-Voigt profile was used as it is described in [98, 50] by using of linear

combination of Gauss and Lorentz functions expressed by:

$$f_{pV}(x) = (1 - \eta) \cdot f_G(x, \gamma_G) + \eta \cdot f_L(x, \gamma_L) \tag{2.3}$$

where f_G and f_L are Gauss and Lorentz functions respectively. The maximum relative deviation from the real Voigt profile is <1.2 %.

2.3 Experiment

2.3.1 Introduction

In geosciences and archaeology, portable LIBS instruments have already been used to identify alteration layers in speleothems, using depth profiles of Sr and Ca [74], for in-situ analysis of bronze artefacts according to their compositional classification [39], and for quarry identification of historical building material [24]. A light LIBS system (ChemCam), representing less than 10 kg of the total payload, has been implemented in the rover Curiosity, which is en route for the planet Mars, with an expected arrival time in August 2012. There are also many papers on the capabilities of such a system to obtain immediate results without sample preparation or use of chemical reagents [91, 95].

In the present study, a portable LIBS was developed to make the instrument as small and light as possible. The aim is to assess its potential for Earth sciences as a tool for geologists in two circumstances: (i) to recognize volcanic eruption ash in sedimentary sequences (tephra layer) and (ii) to evaluate the fossilization processes of ammonites.

In event stratigraphy, volcanic eruptions and subsequent ash deposits are among the best chronostratigraphical markers. During the late Quaternary, the Eifel was the major volcanic complex in Germany. Two main tephra layers are related to this volcanic complex: the Ulmener Maar Tephra (UMT), and the Laacher See Tephra (LST), which produced the greatest geographical extension of ash fall. The age of the LST is 13 180 ± 40 calibrated years BP [17]. The eruption was multi-phased with 3 main ash falls [52, 56]. Its occurrence is recorded in the Jura mountains, located about 500 km from the source, as mm-thick dark layers in lake sediments [16, 106]. However, in the field, it is difficult to identify the origin of dark layers, which could either be LST or simply organic. In this case, the identification of tephra can be performed via the on-site measurement of magnetic susceptibility because ash particles are frequently more magnetic than the surrounding sediment, or possibly at the

laboratory via geochemical measurements. Conventional geochemical analyses are often destructive and time-consuming because of sample preparation. That is why geologists seek rapid, non-destructive spot analysis methods. Here, the capabilities of LIBS are evaluated and compared to those of a portable XRF, which generally fulfils the above-mentioned requirements.

Ammonites were cephalopods occurring from the Devonian to the Late Cretaceous, where they completely disappeared during the well-known mass extinction of the Cretaceous-Tertiary boundary [59]. They are among the most frequently used fossils for building a temporal framework based on organism assemblages (a method called biostratigraphy). Besides their chronological capabilities, ammonites belonged to ecological communities, which are nowadays studied to reconstruct paleoenvironments [108]. Their fossilization process is an important issue for such a purpose. Among the numerous modes of fossilization which may occur, diagenetic pyritization and phosphatization are common. In the phosphatization process, the original aragonite of the ammonite shell is changed into calcium phosphate by replacing carbon with phosphorus. In pyritization, dissolved iron originating from the surrounding sediment precipitates under the form of iron sulphide [71]. Sometimes the shell vanishes and only the internal mould remains. As this later process depends in part on the organic matter content, it may inform about paleoenvironmental conditions. With a portable LIBS, shooting at the same location provides elemental depth profiles, allowing the shell to be chemically distinguished from the internal mould sediment. Its use may help to recognize fossilization processes in the field, and to select specimens suitable for further complementary studies in the laboratory.

2.3.2 Cartography device

The tephra core sample was measured by scanning the surface in perpendicular direction to layer. Moving of the sample was provided automatically by the linear translation stages assembled in the Dijon's laboratory. The stages moves in 3 axes X, Y, Z perpendicular to each other with minimal step 6.25 μm for X, Y and 3,125 μm for the Z axis. The stepper motors for all axes are powered by drivers controlled by the computer via USB port converted to RS422.

For the stage controlling software was developed and its manual can be found in the appendix A. Every move is presented in the software by the command with relative coordinates indicated in a line in the list box. Is is possible to use external trigger command for synchronizing to external event.

It is also possible generate the voltage impulse by the command to trigger some device. Before running sequence of commands in the software they can be tested in simulated 3D space on the computer's display to avoid unwanted behaviour.

For testing purpose, element cartography map of the part of meteorite surface was done. The sample was part of bigger meteorite cut and polished in dimensions approximately 70x70 mm and thickness 5 mm. The acquired maps are presented on the figure 2.13 for Ca, Fe, Sr, Al, Na and Mg elements. Lowest layer is the picture of the meteorite surface measured by the portable LIBS device on the area of 10x10 mm and matrix 20x20 points (0.5 mm for one step). Every point was averaged from 5 shots.

Ca I, Fe I, Sr II and Al I lines have been selected as separated single lines. The Mg I and Na I lines include near 3 and 2 respectively interacting lines of the related element with very close upper levels of transition. All intensity of the lines were normalized to its maximum value from the map for every element.

2.3.3 Tephra layer

A sampling campaign was undertaken in the deposits of the littoral platform of the lake du Val (Jura, France, 46° 37.917' N; 5° 48.825' E). The lake, with a surface area of 64 ha, is known to have received and archived the atmospheric inputs (i.e. tephra layer) resulting from the Laacher See volcano eruption. A 4.35 m sediment sequence, spanning the end of the Late Glacial and the entire Holocene, was recovered using a Russian peat corer (6 cm in diameter and 100 cm in length). The whole core sequence (figure 2.14), reconstructed by overlapping five core segments, highlights five main lithological units as follows, from the base to the top: (unit A) gray laminated clayey silt; (unit B) lacustrine chalk including the black Laacher See tephra layer at 3.67 m depth; (unit C) dark gray clayey silt; (unit D) a thick unit of lacustrine chalk with a dark organic layer at 2.96 m depth; (unit E) organic mire and peat. The core was logged at 5 mm increments with a Bartington MS2 point sensor for high-resolution magnetic susceptibility (MS) measurement. MS values are generally low (less than 10 SI), typical of carbonate deposits. A sharp peak, reaching 156.4 SI at 3.67 m depth, is nonetheless measured within a ≈5 mm black layer (figure 2.14). Such intensity at this depth in a lacustrine chalk unit (unit B) corresponds to the well-known volcanic magnetic minerals originating from the LST ash deposit recorded in the Jura Mountains [106]. The sedimentary

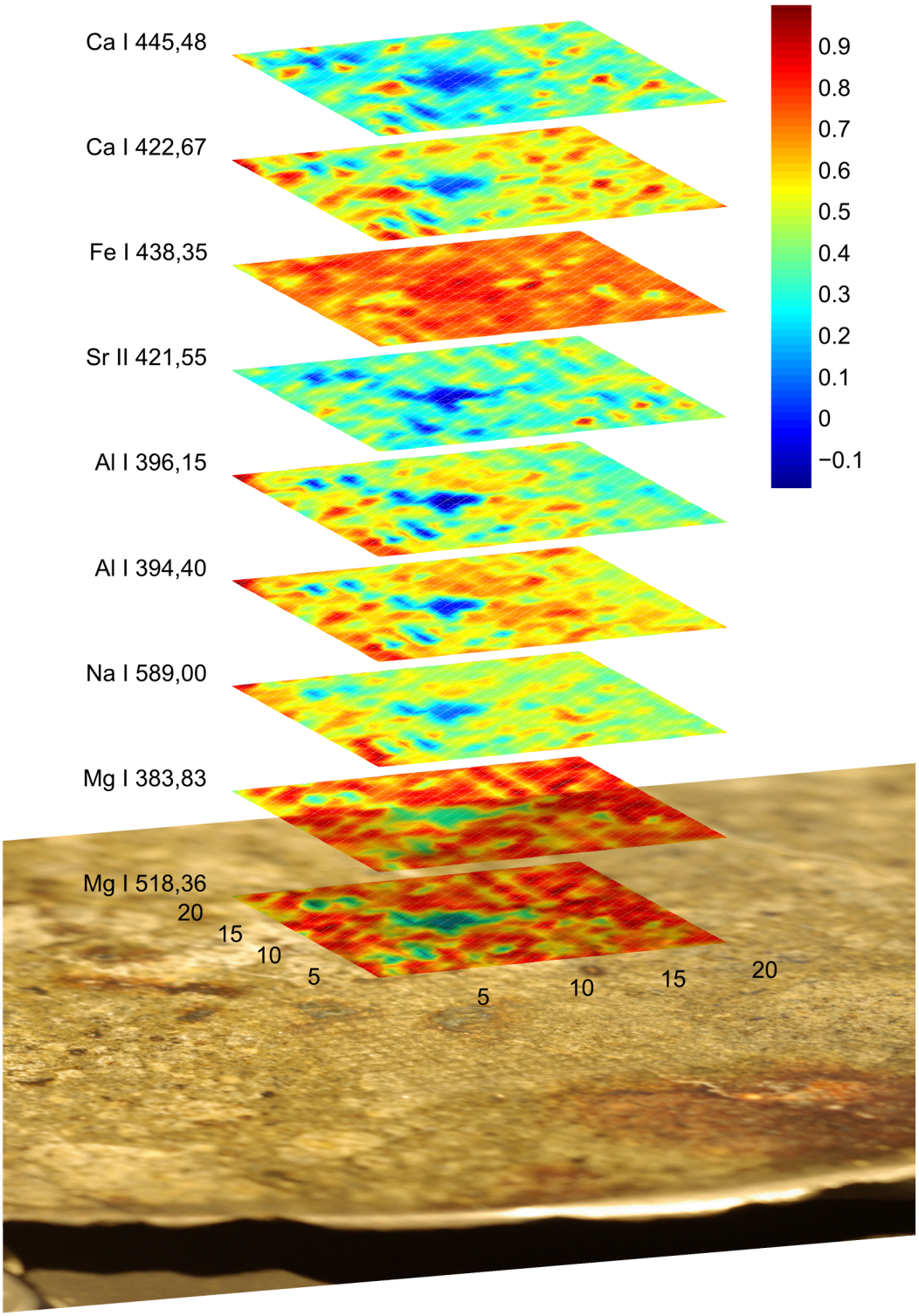

Figure 2.13: Different element cartography maps from the surface of the part of meteorite. The portable LIBS device and the translation stage was used for automated acquisition of 20x20 points with number accumulation 5 for each. The dimension of scanned area is 10x10 mm.

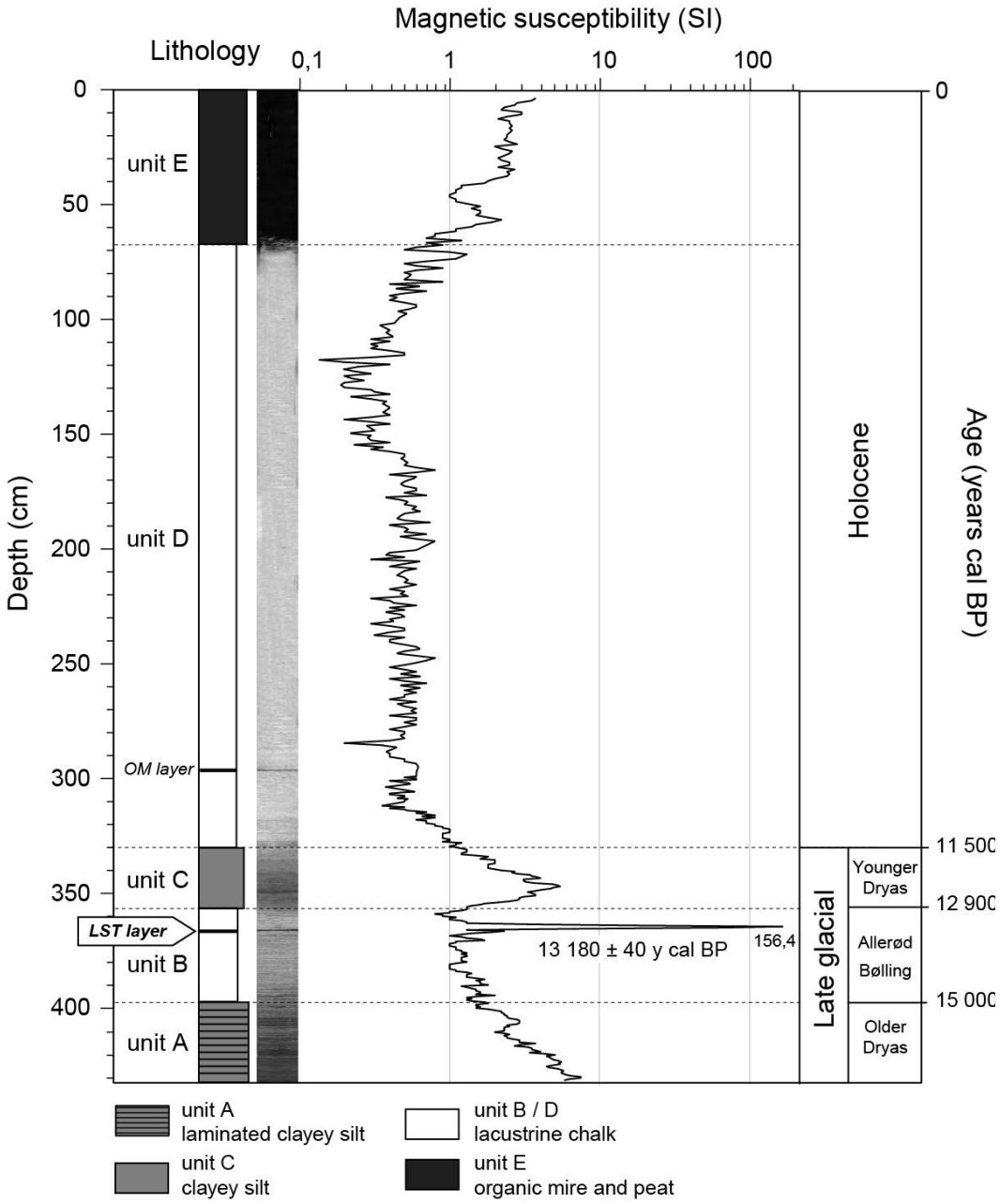

Figure 2.14: Lithology, magnetic susceptibility profile and chronology of the lake du Val core (Jura Mountains). The MS peak corresponds the LST position, at a depth of 3.67 m.

material presented a high water content (> 60 %). As a consequence, the laser pulse energy was in great part consumed by water evaporation processes [13], so that the spectroscopic signals were too low to provide measurements in humid conditions. The sedimentary sequence containing the LST was then cut into smaller pieces and dried at 50°C overnight. The drying process is also referenced to improve signal stability in the case of powder samples [58, 90]. For the spectra acquisition two different methods were used:

(a) Multiplying shots at a single location, then shifting locations by 1 mm along a line drawn perpendicularly to the tephra layer.

(b) Operating single shots, with locations distributed regularly over the surface in order to create a grid of points 0.5 mm apart perpendicular to the ash layer and 0.25 mm apart parallel to it.

In both cases, the laser was fixed in one position and the sample was moved by an automatic transition system. The system was triggered by a photodiode exposed to plasma emission. The acquired spectra were normalized to the sum of the whole spectrum intensity. The intensity of every selected spectral line for all acquired spectra was automatically integrated and background corrected by the software. The following elements and corresponding spectral lines were chosen: Al I-396.15 nm, Ca I-487.81 nm, Fe I-358.12 nm, Ti I-498.17 nm, Ba II-455.40 nm and Na I-589.00 nm. These lines were selected in order to avoid as much as possible interference from other elements. In the case of the Al I-396.15 nm line, there is however strong interference from the Ca II-396.85 nm line. Other possible Al lines exist at 308.22 nm and 309.27 nm, but the signal-to-noise ratios are too low in this part of the spectrum. An Fe line also interferes with the selected Ti line. Nonetheless, the lack of correlation between this Ti line intensity and the stronger Fe line suggests that measuring Ti-498.17 nm does not constitute a major drawback.

For comparison, a commercial portable XRF system - Delta Handheld XRF from Innov-X Systems - was also used. The device, which is originally hand held, was attached to a closed-beam workstation, and was controlled by dedicated software. Elemental quantification was carried out using an implemented 3-beam analysis method (integration time of 30 s for each beam) optimized for the analysis of heavy, transition and light elements in soils. Before the measurements, a calibration process was performed, as suggested by the manufacturer. It consists in a calibration check, blank (pure commercial SiO_2) measurement, and one or several measurements of certified reference materials

(CRMs): NIST 2781 & NIST 2702. Acquisition was performed on the sedimentary sequence in different positions, on a line of 50 mm, perpendicular to and centred on the tephra layer, with a step of 2.5 mm. The diameter of the measurement window is about 15 mm. Daily reproducibility was estimated under the basis of the values obtained on the CRM replicates. Relative standard deviations (RSDs%) of 2–10% were computed for lithophilic elements, such as Ti and Fe, while the RSD% of Ba was much higher, at about 35%. This value is a consequence of the high uncertainties related to each measurement, for which individual RSDs% vary between 20 and 40%, at a concentration level for Ba of 400-600 μg.g^{-1}- In order to obtain a significantly more precise Ba measurement for the Lasher See layer, the acquisition time was multiplied by 3 when approaching the tephra horizon. Certified values, when provided, allowed the accuracy of XRF measurements to be checked. The recovery was 156–181% for Ti and 110–120% for Fe. Such values lead to clear overestimations from a purely quantitative point of view, but as measurements were proved to be fairly reproducible, the examination of XRF-derived profiles should provide good indications of variability in chemical compositions along the sequence.

2.3.4 Ammonites

The ammonites were collected from the Belmont quarry, located close to Lyon, France. These outcrops are dated from the Lower to Middle Jurassic (Toarcian to Aalenian). The ammonites studied come from the Toarcian stage. One of the main interests of the quarry is that it offers the opportunity to test various modes of fossilization (pyritization and phosphatization). Five different ammonite species were selected:

Specimens A1 & A2. Dumortieria munda. They possess well preserved thin ribs, and are completely white. This type of fossilisation is generally considered as phosphatization, which may correspond to a chemical transformation of the initial aragonite (calcium carbonate) shell. They belong to the Pseudoradiosa Zone (Lower Jurassic).

Specimens B1 & B2. Hildoceras bifrons. They are black or dark red and are supposed to be pyritized on their external parts. They are fossilized as internal moulds (absence of external shell layers). They belong to the Bifrons Zone (Lower Jurassic).

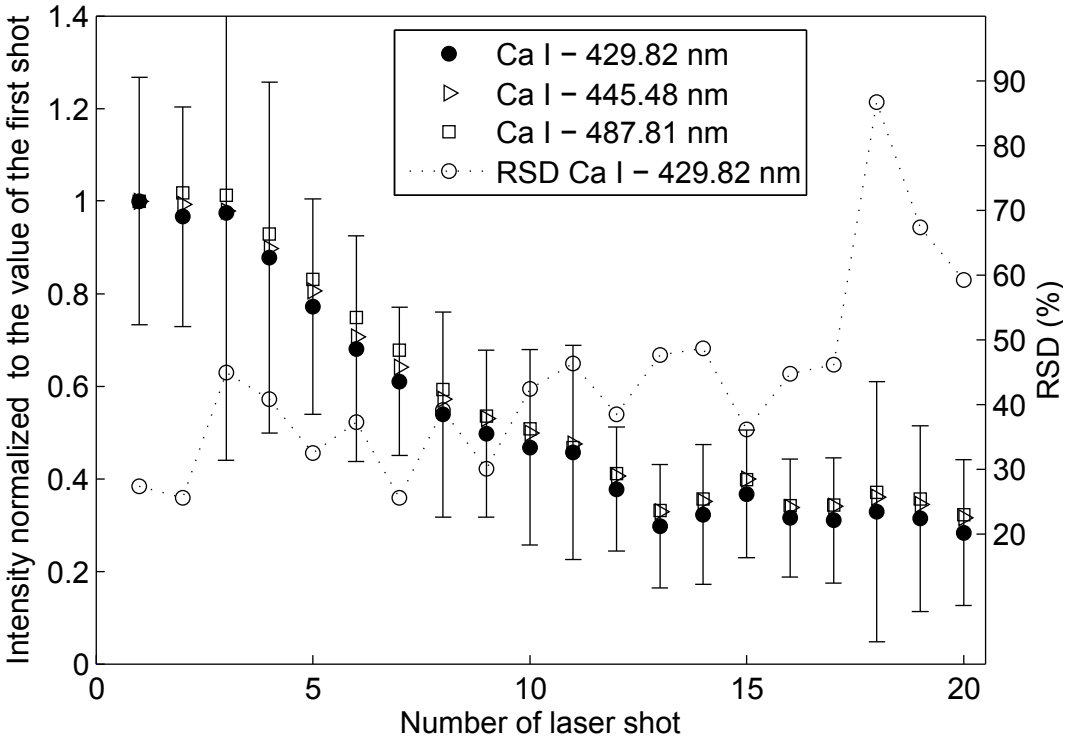

Figure 2.15: Intensity (normalized to the value of the first shot) and RSD% vs number of laser shots for three calcium lines. Tests were performed on the lacustrine chalk sample, shooting at the same location (the whole operation was repeated 15 times). Error bars correspond to the standard deviation for the Ca I-429.82 nm line.

Specimen B3. Hildoceras bifrons. It is grayish green without any visible shell layer. Therefore, the specimen seems to be an internal mould, totally composed of sediments. It belongs, like B1 and B2, to the Bifrons Zone (Lower Jurassic).

Specimen B4. Hammatoceras sp. It is grayish red, without any visible shell layer. Therefore, the specimen seems to be an internal mould, totally composed of sediments. It belongs to the Variabilis Zone (Lower Jurassic).

2.4 Results and discussion

2.4.1 Tephra layer

Preliminary tests were conducted on lacustrine chalk to optimize acquisition parameters (intensity and signal-to-noise ratio). Figure 2.15 exhibits the evolution of signal intensity and RSD% in relation to the number of shots performed

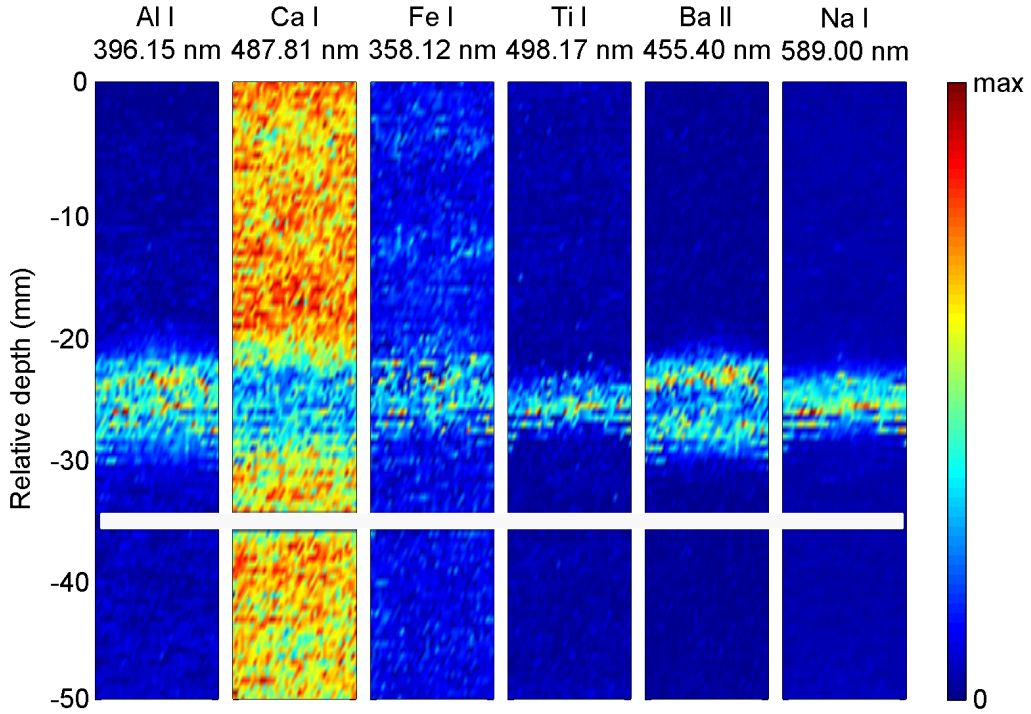

Figure 2.16: 2D elemental abundance map for a 50 mm (vertical) x 10 mm (horizontal) part of core centred to the tephra layer. The origin of the Y-axis corresponds to the depth 3.645 m of the original core. The white horizontal bar at ≈-35 mm of relative depth corresponds to a 2 mm-wide crack in the core where measurements were not possible. Laser was operated in single shot mode, producing a total of 100 x 40 points. Intensity of lines is depicted by a colour code.

at the same location. All line intensities fall to ≈30 % compared to the first shot, and stabilize after approximately 13 shots. The RSD% can reach more than 50% after 17 shots. After 20 shots the crater reaches approximately 1 mm in diameter and depth. Such a large volume of removed material is due to the specific nature of the sample (a powder), which is easily expelled by the shock wave from plasma expansion. The ablation of material from the focal point is responsible for the degradation in quality of the measurements. Accumulating shots in the same position did not improve signal intensity, signal-to-noise ratio, or RSD%, as initially expected. The best choice consists either in moving the laser spot to different but close locations after each shot (rastering), or in limiting the number of shots. A rastering procedure requires a precise displacement of the system that is hardly compatible with our portable, handheld system.

Several 2D elemental abundance maps were produced for a segment con-

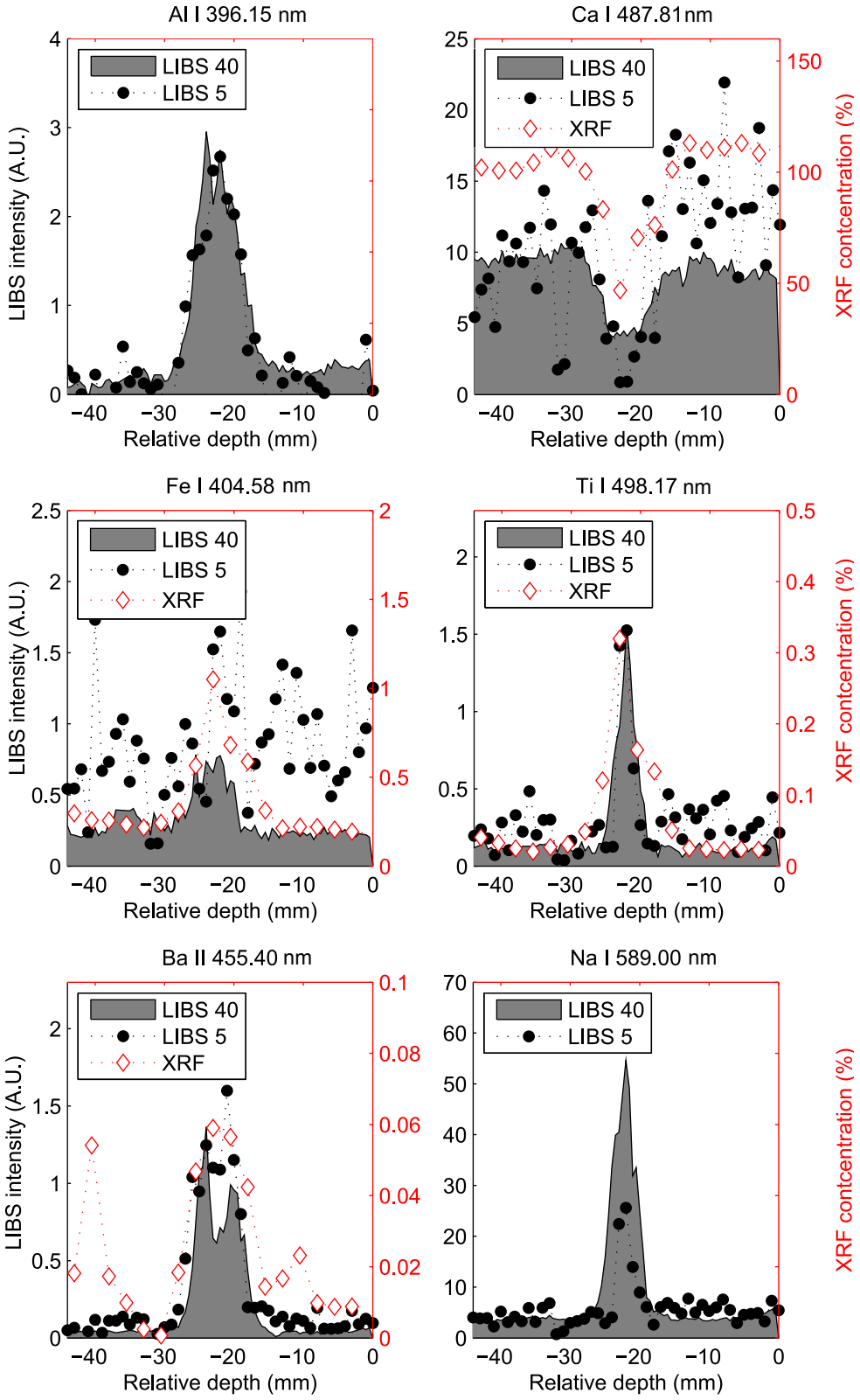

Figure 2.17: Line intensities Al, Ca, Fe, Ti, Ba and Na with depth. The origin of the Y-axis corresponds to the depth 3.645 m of the original core. LIBS-40 profiles are computed from the 2D elemental abundance maps (see text), LIBS-5 corresponds to the average of 5 shots from a same location. XRF measurements are provided for comparison. A.U.: arbitrary unit.

taining the tephra layer. The area of interest covers 50 mm (vertical) x 10 mm (horizontal) (figure 2.16). The tephra layer is clearly noticeable by a positive anomaly in Fe, Na and terrigeneous elements (Al, Ti, Ba), which are all strongly and positively correlated, and by a negative Ca anomaly, which can be taken as a surrogate of carbonaceous chalk content. Such behavior is even clearer in a section view performed by averaging all 40 horizontal points of the slice for each vertical position, namely LIBS-40 (figure 2.17). A one-dimensional (vertical) transect was performed as a test along the sedimentary sequence, using only 5 shots, namely LIBS-5 (2.17). With such settings, line intensities should decrease, at most, to approximately 70% of the first shot (figure 2.15), while the measured crater diameter does not exceed 0.3 mm. Using only 5 shots limits the acquisition time, but it is hoped that measurement quality will not be drastically degraded. The Ba, Al, Ti and Na profiles obtained by LIBS-5 are comparable to those computed from the map (LIBS-40), and therefore exploitable to detect the tephra layer. In contrast, Ca and Fe profiles become too noisy to be of real geological interest. XRF-derived Ti, Fe and Ca results are in good agreement with LIBS-40. For Ba, the situation is less clear because several positive anomalies, which are not detected with LIBS-5 and LIBS-40, are measured with XRF. To summarize, the tephra layer is characterized by high Ti, Ba Al, and Na content which can be easily detected by LIBS and by XRF for the first element. However, as the measurement window of the XRF has a diameter of approximately 1.5 cm, the Ti profile obtained by this method is over-smoothed in comparison with those deriving from spot analyses by LIBS. LIBS is able to distinguish two local maxima within the ash layer (which might be the result of post-depositional migration), while XRF measurements provide a single broad peak.

Simulations were performed from the elemental abundance maps to optimize the acquisition settings in the case of handheld measurements. Two circles of 5 mm in diameter were selected: one in the middle of the tephra layer and the other within the lacustrine chalk (figure 2.19). From 1 to 30 shots, replicated 1000 times, were simulated at random positions in both circles. The resulting mean values, with their 95% confidence intervals, are depicted in the figure 2.18. Except for Fe, differences between the tephra layer and the surrounding lacustrine chalk can be determined successfully by only 2 shots, except for Fe I-404.58 nm; nine shots are necessary to eliminate the overlap of the two 2-sigma error bars.

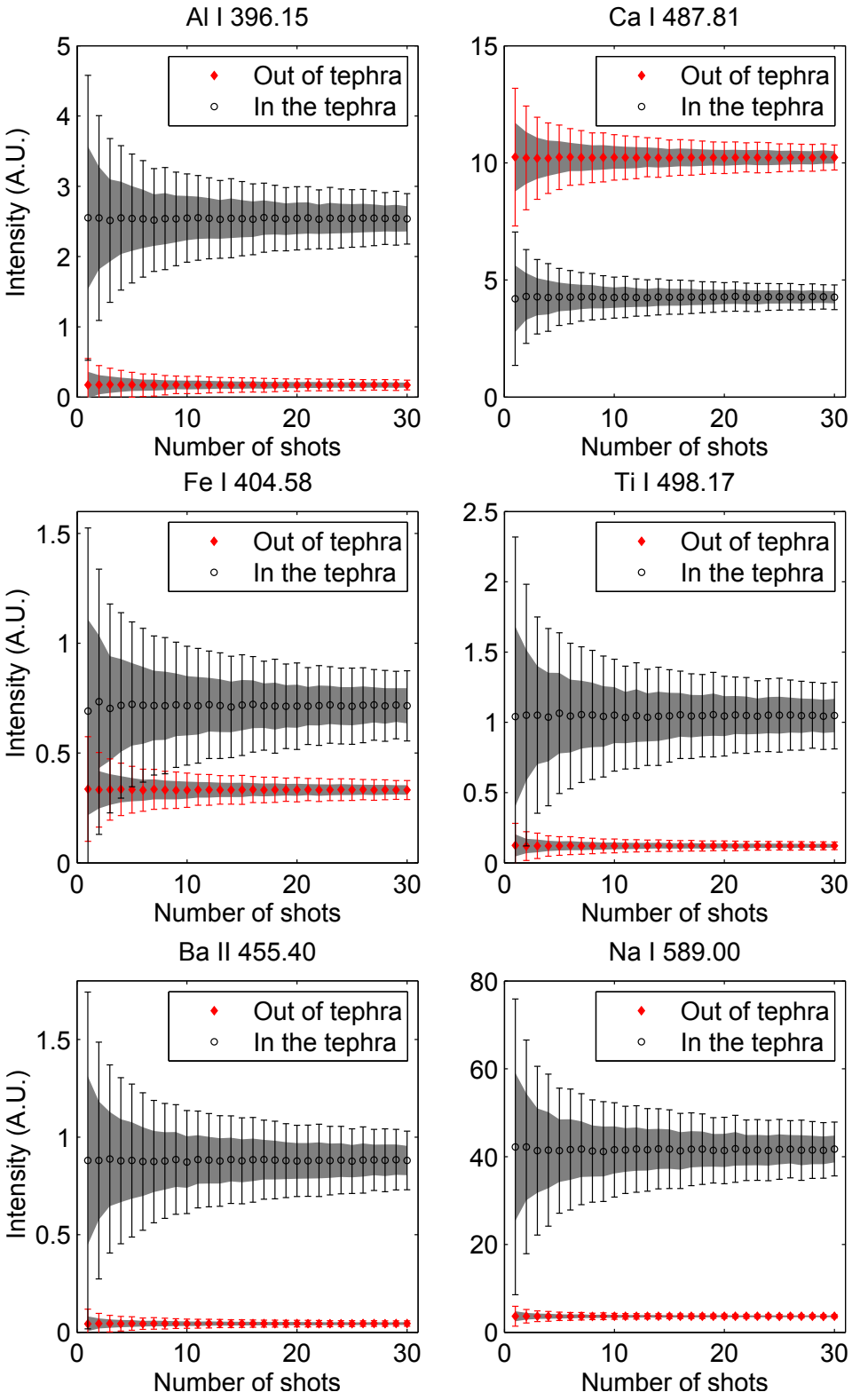

Figure 2.18: Mean line intensities, standard deviation (gray area) and 95% confidence interval of the mean in and out of the tephra following the number of simulated shots. For every number of shots, 1000 simulations were generated. A.U.: arbitrary unit.

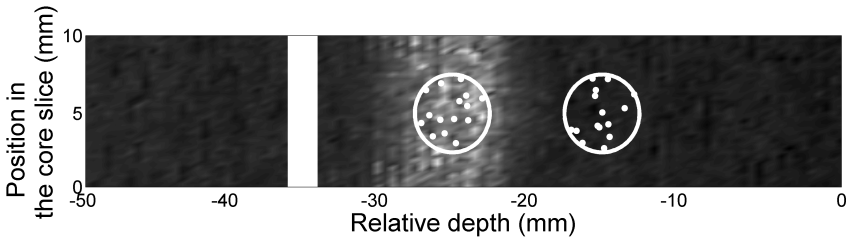

Figure 2.19: Position and dimension of circles in the slice core used to simulate random shooting in and out the tephra layer. The gray scale corresponds to Ca I-487.81 nm. Fifteen random shots, distributed on the both circle surfaces, are depicted as an example. The white vertical bar at -35 mm of relative depth corresponds to a 2 mm-wide crack in the core where measurements were not possible.

2.4.2 Ammonites

Phosphatization processes. The most straightforward approach to study the phosphatisation process would consist in monitoring phosphorus content. To test the possibility of phosphorus emission line detection, an InP wafer (for semiconductor industry) was used as a sample. The lines of this element are usually detected at the wavelengths of 253.65 nm, 255.32 nm [10], 213.62 nm, and 214.92 nm, or in deeper UV. As mentioned above, it was not possible to detect any phosphorus line in the 213.62–255.32 nm range with the InP wafer, because of the low signal-to-noise ratio. In the deeper UV part of the spectrum, the lines are also too weak to be detected. The situation did not improve when a greater number of shots was accumulated. As a result, it is not possible to determine the phosphatization process by direct determination using our portable LIBS system. Complementary measurements may however provide useful information. The white ammonites (Dumortieria munda, A1-figure 2.20 - & A2), assumed to be phosphatized, were measured by accumulating 10 laser shots at a single location both (i) on the white material constituting the shell, and (ii) on the red material filling the shell. High Ca peaks, more particularly the peak at Ca I-487.81 nm, are observed in the shell, while the presence of Fe-rich filling material is demonstrated by a notable peak at Fe I-495.76 nm (figure 2.21). The same behavior can be observed with Al (although not visible in this spectral range) and Ti, which are both only present in the infilling material.

Accumulating shots at the same position is equivalent to digging samples.

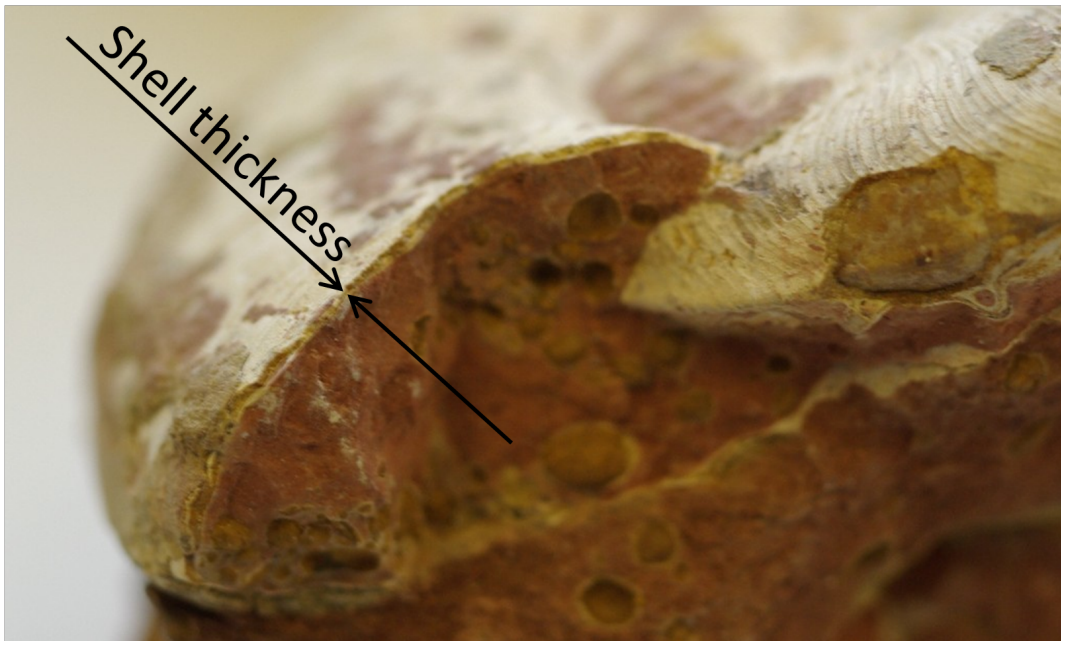

Figure 2.20: A1 sample ammonite. The shell and infilling material are visually distinguishable.

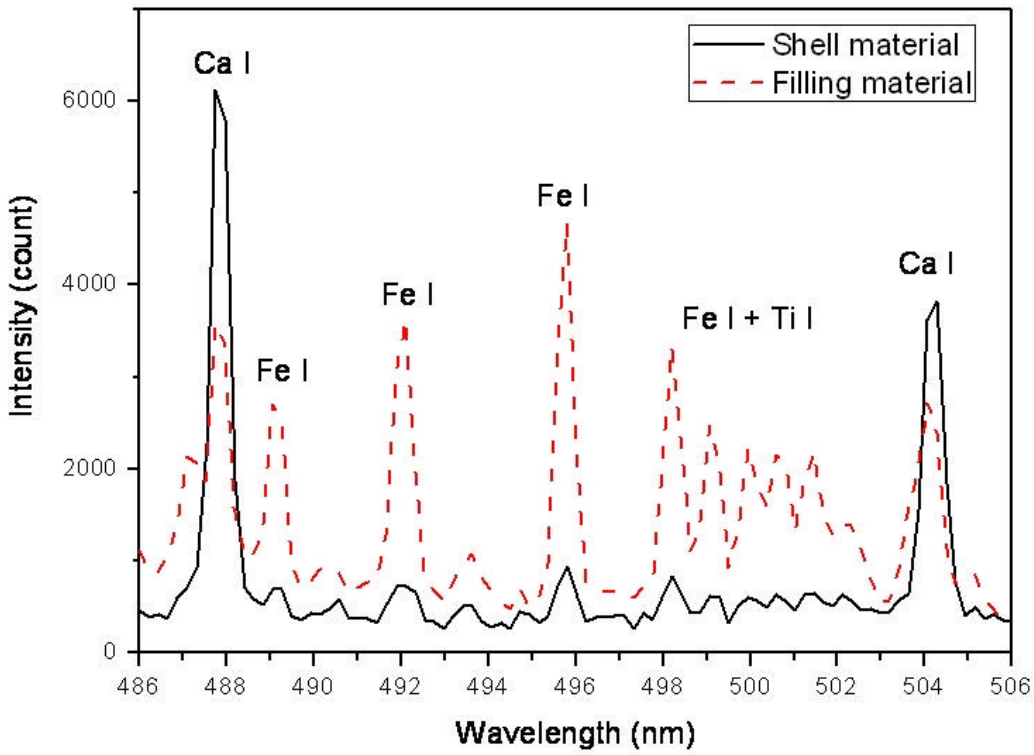

Figure 2.21: Intensity spectra of shell and infilling material for the ammonite A1. The spectral lines corresponding to Ca, Ti and Fe are reported.

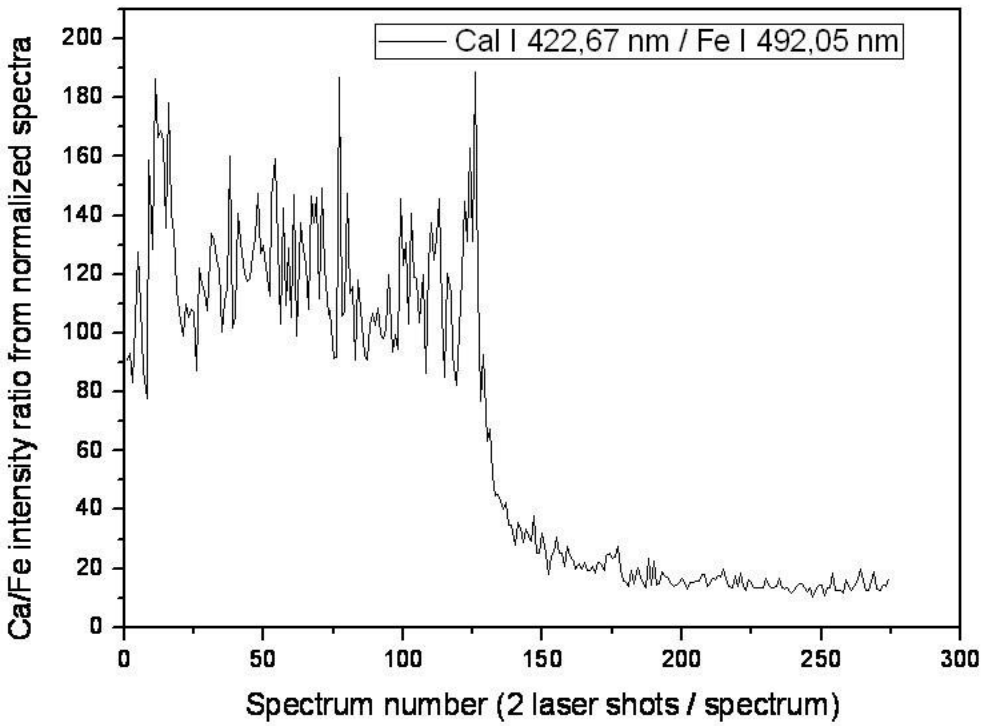

Figure 2.22: Ca I-422.67 nm / Fe I-492.05 nm line intensities ratio for 275 spectra, all acquired at the same locations on the white A1 ammonite. Intensities are obtained after accumulating two laser shots and normalizing to the total area.

It can therefore be considered as producing an elemental depth profile in relation to the ablation power of the laser. A total of 275 spectra, performed with 2 shots each, was acquired at the shell surface of the A1 specimen. The Ca I-422.67 nm *s* Fe I-492.05 nm intensity ratio was around 120 for the 130 first spectra, then decreased abruptly to ≈20 and remained steady up to the last spectra (figure 2.22). The breaking point around the #130 spectrum clearly illustrates the transition between the shell and the infilling material. As a result, shell and infilling material can easily be distinguished by their chemical signature using LIBS.

Pyritization processes. As with the white ammonites, shell and infilling material of the B1 specimen are chemically different in terms of Ca, Fe and Ti intensity lines (figure 2.23). The situation is however reversed as the shell is enriched in Fe, while the infilling material is Ca-dominated. For the am-

monites B1 (B1a & B1b) and B2, suspected of pyritization, elemental profiles exhibit similar patterns: Ca line intensities increase with the number of shots, while Fe mirrors the Ca variations (Figure 2.24). The negative correlation observed between Ca and Fe is perfectly compatible with the assumption which consists in replacing Ca by Fe during the pyritization process. The Ca and Fe profiles at B1a present however a lower slope. This is related to the greater thickness of the pyritized layer at that location. Line intensities do not drastically change with the number of shots for specimens B3 and B4 (figure 2.24). Such results are chemically in good agreement with our primary visual inspection, which suggested that each fossil was totally composed of homogeneous material, without any shell preservation.

2.5 Second layer

In the core two different layers have been observed, one at 3.67 m and second at 2.96 m depth. First one have been assigned to LST tephra as it is presented in section 2.3.3. Second one was considered to be probably organic layer. The measurement of cartography map similar to that described in section 2.3.3 have been performed with the slice core containing the second layer and compared with results obtained by tephra layer measurement. The spectra have been acquired by operating single shots, with locations distributed regularly over the surface in order to create a grid of points 0.5 mm apart perpendicular to the layer and 0.25 mm apart parallel to it. Grid of 40 x 40 points have been created.

The composition of both samples (tephra and unknown layer) have been analysed by independent laboratory with Fusion Inductively Coupled Plasma (FUS-ICP). Analyse have been done for 6 different locations in the core as it is marked by C4, C5 and C6 for tephra layer and C1, C2 and C3 for the second layer in the figure 2.25. The results are presented in the table 2.2.

LIBS Results from measurement of the slices cores for unknown layer and surrounding sediment is shown in the figure 2.26. The elements and emission lines for which the elemental abundance map is shown are same as it is presented in the section 2.4.1. The layer is clearly noticeable by a positive anomaly in Fe, Na and terrigeneous elements (Al, Ti, Ba), which are all strongly and positively correlated, and by a negative Ca anomaly, which can be taken as a surrogate of carbonaceous chalk content. Such behavior is even clearer in a section view performed by averaging all 40 horizontal points of the slice for

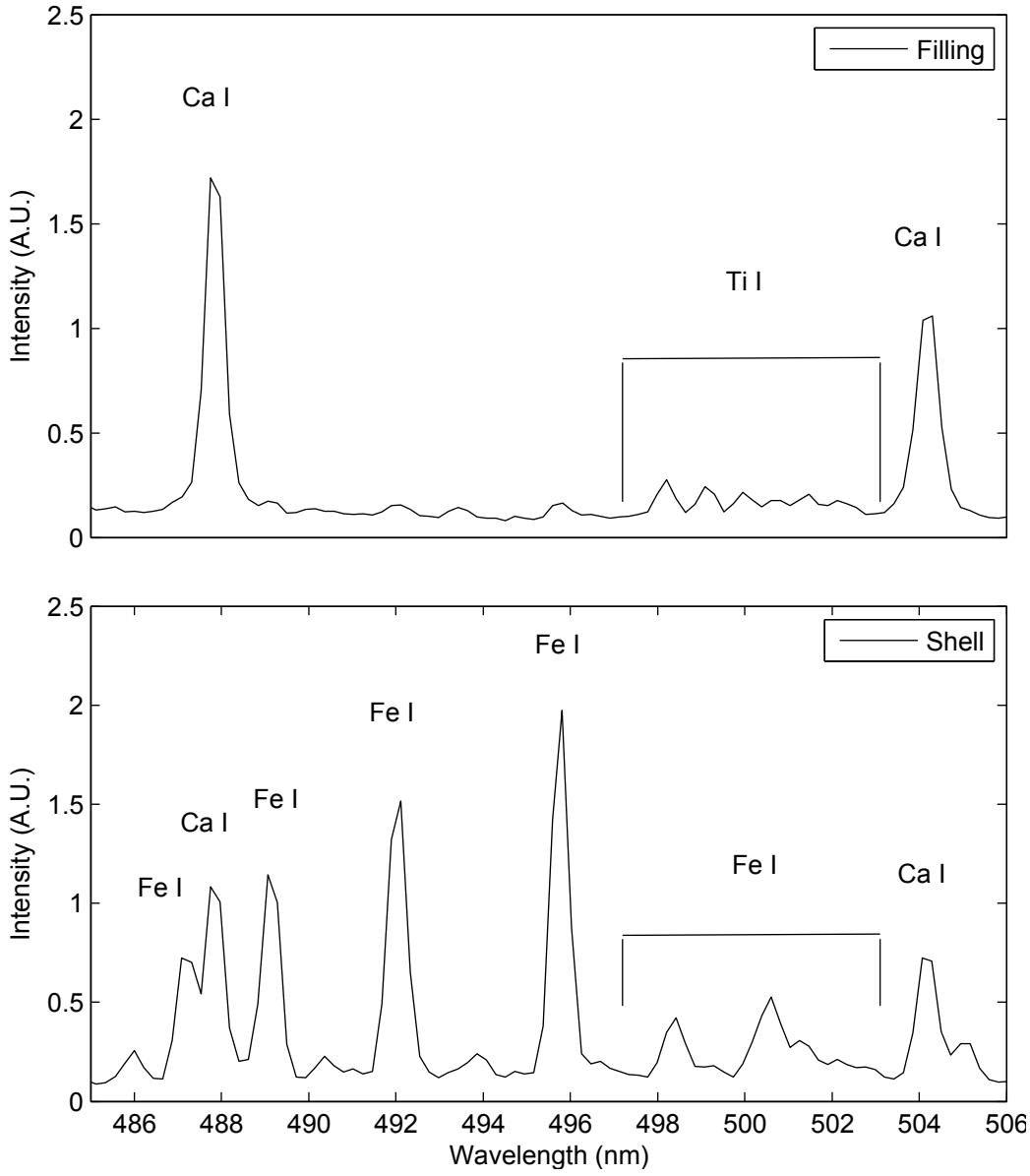

Figure 2.23: Intensity spectra of shell and infilling material for the ammonite B1. Each spectrum corresponds to the average of 25 shots. A.U.: arbitrary unit.

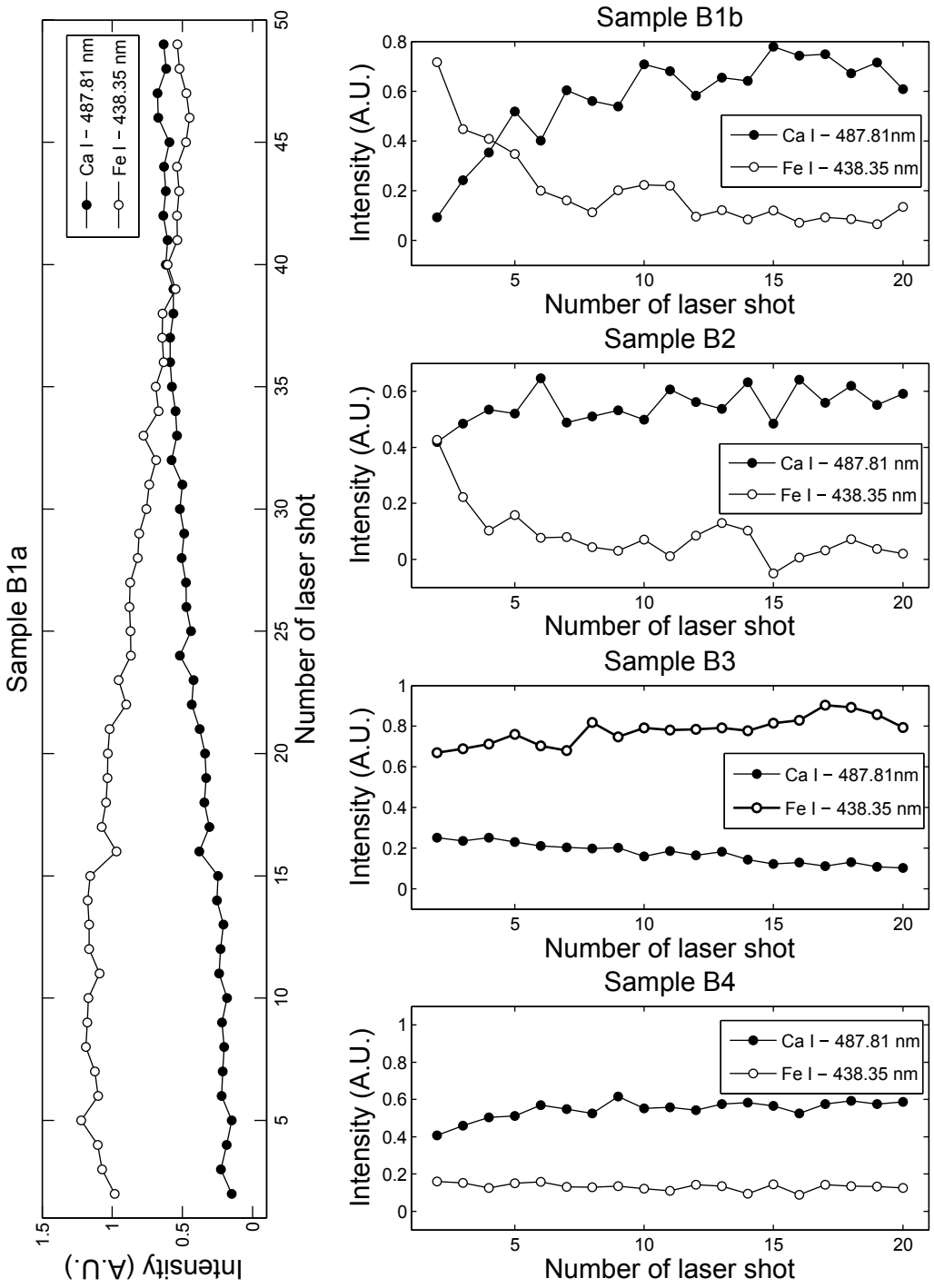

Figure 2.24: Intensity evolution of Fe I-438.35 nm and Ca I-487.81 nm lines as a function of the number of shots for ammonites B1, B2, B3 and B3. Shots were operated at two different locations for specimen B1 (named B1a and B1b). The first shot was systematically discarded because it was considered as a cleaning shot. A.U.: arbitrary unit.

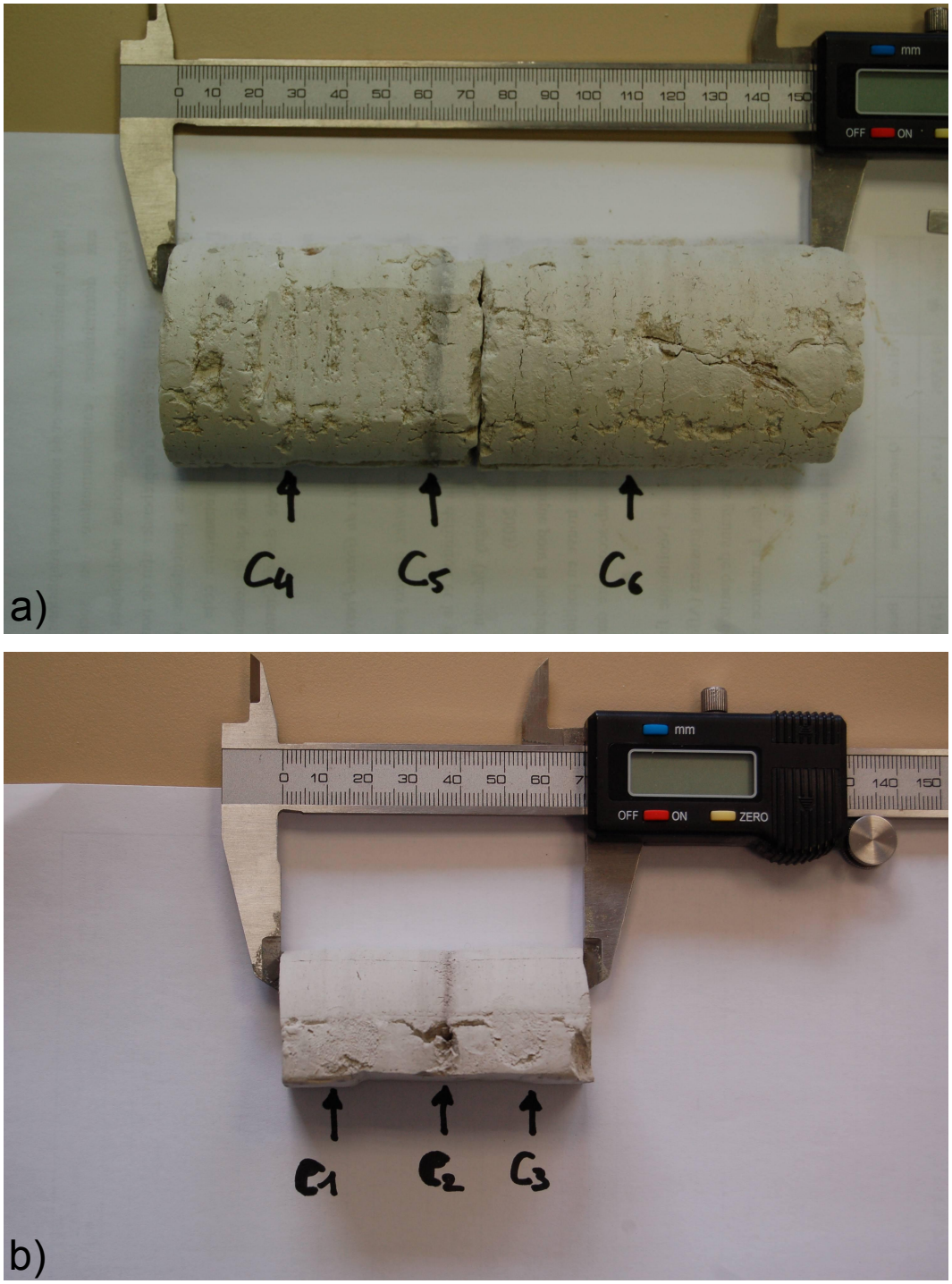

Figure 2.25: Pictures of a) Tephra and b) unknown layer in the sediment.

Analyte Symbol	Unit	Detection Limit	C1	C2	C3	C4	C5	C6
SiO_2	%	0.01	4.37	19.63	6.35	1.4	22.2	1.96
Al_2O_3	%	0.01	1.56	5.57	2.18	0.56	9.67	0.79
Fe_2O_3	%	0.01	0.76	1.54	0.86	0.28	1.49	0.4
MnO	%	0.001	0.012	0.016	0.014	0.008	0.021	0.009
MgO	%	0.01	0.52	1.7	0.67	0.35	0.54	0.38
CaO	%	0.01	51.61	34.9	48.58	52.61	33.88	52.6
Na_2O	%	0.01	0.05	0.16	0.05	0.01	0.79	0.02
K_2O	%	0.01	0.3	1.05	0.43	0.12	1.74	0.14
TiO_2	%	0.001	0.072	0.314	0.103	0.025	0.339	0.041
P_2O_5	%	0.01	0.02	0.05	0.02	< 0.01	0.07	< 0.01
Ba	ppm	2	34	123	42	17	654	24
Sr	ppm	2	144	148	142	143	461	155
Y	ppm	1	4	12	5	2	9	3
Sc	ppm	1	2	5	2	< 1	3	1
Zr	ppm	2	16	84	22	8	81	10
Be	ppm	1	< 1	1	< 1	< 1	1	< 1
V	ppm	5	23	72	27	11	37	11
LOI	%		40.32	33.84	37.72	40.57	27.53	42.42
Total	%	0.01	99.59	98.78	96.99	95.94	98.26	98.75

Table 2.2: Composition of the core with sediment measured in the 6 locations. C1, C3, C4 and C6 are located in surrounding lacustrine sediment, C5 is tephra layer and C2 unknown layer compositions.

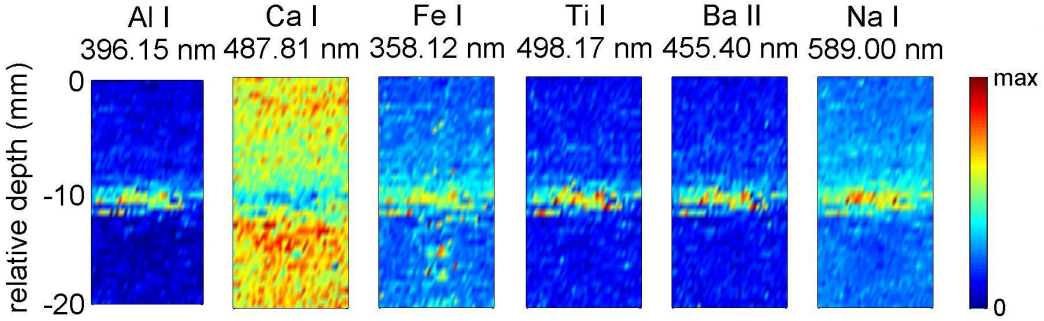

Figure 2.26: 2D elemental abundance map for a 20 mm (vertical) x 10 mm (horizontal) part of core centred to the unknown layer. The origin of the Y-axis corresponds to the depth 2.95 m of the original core. Laser was operated in single shot mode, producing a total of 40 x 40 points. Intensity of lines is depicted by a colour code

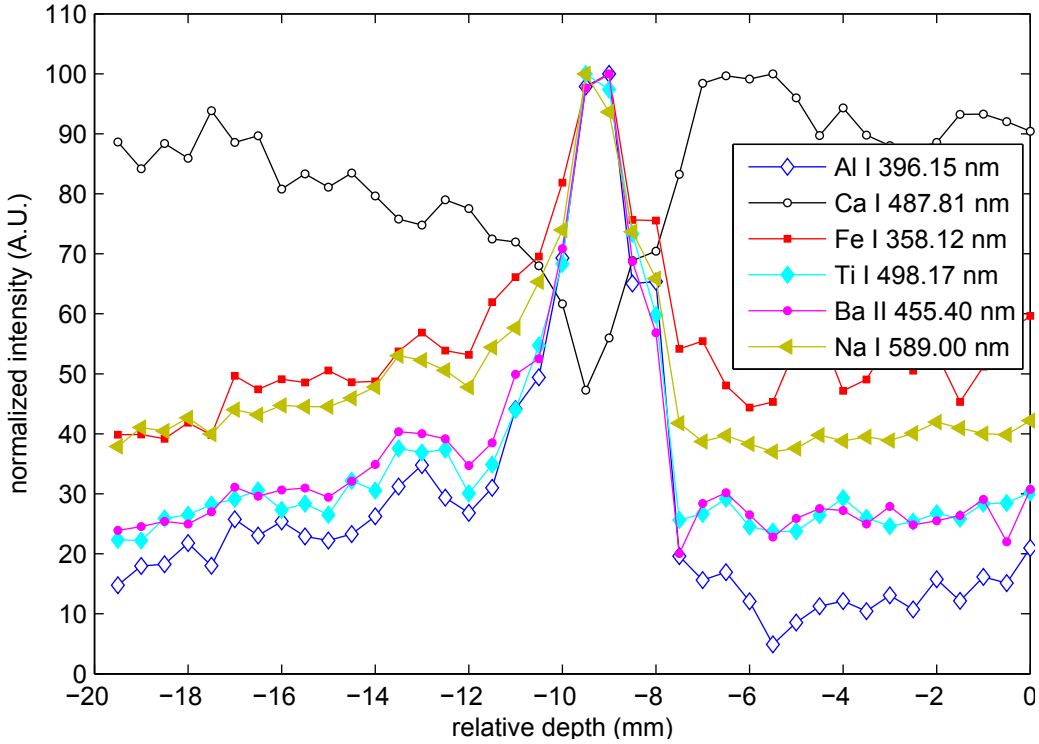

Figure 2.27: Profiles of the elemental abundance along slice core centred to unknown layer. The profiles are computed from the 2D elemental abundance maps from the figure 2.26.

each vertical position, shown in figure 2.27.

In comparison with results obtained for tephra layer presented in section 2.4.1 on the figures 2.16 and 2.17 the similar behavior for different elements can be seen. In case of the unknown layer its thickness is lower and can be estimated to ≈4 mm. From such a results the unknown layer is more probably originate from tephra than from organic sediments.

The similarity in tephra and unknown layers can be also observed in results obtained by ICP analyse. Behavior of concentration of all the detected elements is same in tephra and unknown layer. The layers are clearly noticeable by a positive anomaly in all elements except Ca with negative anomaly in both layers. This supports the consideration that the unknown layer is probably the tephra rather the organic origin. Such the conclusion would be interesting because to the best of our knowledge there is no publication be concerned with the second layer. But further analyses must be performed to verify origin of the unknown layer.

2.6 Conclusion

To the best of our knowledge, this is the first time that a portable LIBS system has been efficiently used to identify tephra layers in lacustrine chalks. A clear geochemical difference between the tephra layer and lacustrine chalks was observed for Al, Ca, Ti, Ba, and Na. For Fe, the difference becomes clear after 9 shots because the geochemical contrast between ash and the surrounding layers is low. The thickness of the ash layer appears different when assessed with Na and Ti (5 mm) and Al, Ca and Ba (10 mm), probably because of post-depositional migration of the latter group of elements. In any case, the LIBS system provides more accurate thickness determination than XRF because of the large acquisition window in the XRF. Al and Na were not successfully detected by XRF, whereas K, Cr, Mn, Co, Zn, Rb, Sr, and Zr, were determined by XRF, but not detected by the portable LIBS.

The resolution of the spectrometer and the sensitivity in the UV region is not adapted to the study of the phosphatization process. The pyritization process was chemically identified on precisely those 2 ammonite specimens that appeared as black or dark red to the naked eye. An interesting application - because of the spot analysis capacities of the LIBS - would be determining chemical shell patterns of several specimens from the same layer in order to study fossilization processes and their homogeneity.

Our portable LIBS system can therefore already be considered as a useful and practical on-site tool for geology. Semi-quantitative or quantitative measurements, long sought after by geoscientists, could be the next improvement to our portable LIBS.

Chapter 3

Laboratory LIBS

3.1 Introduction

The following sections will describe the possibility of temperature and composition determination of LIP by using several line intensities for one element. The lines are usually chosen from wide range of the analysed spectra whereby their relative intensities must be correct and not affected by optical system response. The methods are based upon measurement of line intensities and somehow comparison with their theoretical intensities calculation. The power emitted by unit volume into the unit solid angle ($\mathrm{Wm^{-3}sr^{-1}}$) by transition of atoms or ions from upper level j to lower level i is described by expression:

$$I_{ji} = \frac{hc}{4\pi\lambda_{ji}} A_{ji} n_j \tag{3.1}$$

where h is Plank constant, c is speed of light, λ is wavelength of photon emitted by transition, A_{ji} is Einstein coefficient for spontaneous emission and n_j is density population of upper level. Einstein coefficients are intrinsic properties of atomic transitions from upper to lower energetic level and they can be found in databases with certain precision [49, 57, 75]. Under assumption of LTE density number n_j can be expressed by Boltzmann expression:

$$n_j = n \frac{g_j}{Z(T)} e^{-\frac{E_j}{kT}} \tag{3.2}$$

describing population distribution of atomic or ionic states with energetic spectrum E_j with temperature T. The n is density number of specie for which distribution is calculated (atom or ion density number), g_j is degeneracy of j-th state and $Z(T)$ is a partition function. The partition function is defined

as:

$$Z(T) = \sum_{i=1}^{N} g_i e^{-\frac{E_i}{kT}} \tag{3.3}$$

where N is number of all possible states with degeneracy of states g_i and their energy E_i.

Because of high temperatures of LIP, high ionization degree is common. The ionization degree of plasma in LTE is described by Saha equation[45]:

$$\frac{n^r n_e}{n^{r-1}} = \frac{2Z^r(T)}{Z^{r-1}(T)} \frac{(2\pi m_e kT)^{3/2}}{h^3} e^{-\frac{E_\infty^{r-1} - \Delta E_\infty^{r-1}}{kT}} \tag{3.4}$$

where n^{r-1} and n^r are densities of atoms in ionization state $r-1$ and r respectively (index 0 for neutral atom), n_e is density of electrons, $Z^{r-1}(T)$ and $Z^r(T)$ are partition functions for ionization state for related ionization state respectively m_e is electron mass, E_∞^r is the ionization potential of state from $r-1$ to r and ΔE_∞^r is correction of the ionization energy in plasma [41].

For usage of Boltzmann and Saha expressions, LTE described in the section 1.5 is needed to be satisfied. Additionally, calculation of line intensities by 3.1 suggests plasma to be optically thin. If plasma is not optically thin, one needs to consider usage of Einstein B coefficients which are responsible for absorption and stimulated emission, sometimes referenced as a negative absorption. If the plasma is not in LTE, kinetics of reactions must be calculated with knowledge of rate constants for reactions, or different distribution which better describes the plasma must be used.

Commonly in process of measurement, experimental spectra are influenced by spectral response of used optical system. The influence of the optical system must be eliminate in order to successfully application of Boltzmann of Saha equation. The Echelle type of the spectrometer is used for spectra analyse in presented LIBS measurements in laboratory in Bratislava. Determination of its spectral response was processed and it is presented in section 3.5.

3.2 Boltzmann plot

When LIP is in LTE, the distribution of energetic levels of atoms and ions obeys Boltzmann distribution described by the formula 3.2. This means that only knowledge of the temperature T is needed to determine relative population in all states of atoms and ions. Even if the total density n is not known, by

making the ratio of Boltzmann expression for two different states we obtain:

$$\frac{n_j}{n_l} = \frac{g_j}{g_l} e^{\frac{E_j - E_l}{kT}} \tag{3.5}$$

the expression which is not longer dependent on total density and can be used for determination of ration for two different states. The ratio can be obtained also by measurement of emission line intensities related to transition from upper level n_j and n_l by using expression 3.1:

$$\frac{n_j}{n_l} = \frac{I_{ji}\lambda_{ji}A_{lk}}{I_{lk}\lambda_{lk}A_{ji}} \tag{3.6}$$

where A_{ji} and A_{lk} are related Einstein coefficients for upper and lower levels indexed j, l and i, k respectively. Connection of expression 3.5 and 3.6 will produce formula from which temperature of atom or ion electronic states can be determined:

$$T = \frac{E_j - E_l}{k \cdot ln\left(\frac{g_j}{g_l}\frac{I_{lk}\lambda_{lk}A_{ji}}{I_{ji}\lambda_{ji}A_{lk}}\right)} \tag{3.7}$$

However, the temperature determination from expression 3.7 is strongly influenced by the error which can be expressed as [8]:

$$\frac{\Delta T}{T} = \frac{kT}{E_j - E_l}\frac{\Delta R}{R} \tag{3.8}$$

$$R = \frac{g_j}{g_l}\frac{I_{lk}\lambda_{lk}A_{ji}}{I_{ji}\lambda_{ji}A_{lk}} \tag{3.9}$$

Line intensities in the process of measurement can be negatively influenced by interaction with some other lines, by self-absorption or by some other effects. The determination of line intensity from measured profile can include additional errors via process of area determination under the line profile (summing, background subtraction or fitting) The errors produced via uncertainties in Einstein coefficients are also possible.

To avoid such a big sensitivity of the error in temperature determination the usage of more than 2 lines in so called Boltzmann plot method is recommended [8]. If correction for spectral response of spectrometer was already done, from expression 3.6 and 3.5, following expression can be obtained:

$$\underbrace{ln\left(\frac{I_{ji}\lambda_{ji}}{A_{ji}g_j}\right)}_{\text{y}} = \underbrace{ln\left(\frac{hcn}{4\pi Z(T)}\right)}_{\text{q}} - \underbrace{\frac{1}{kT}E_j}_{\text{kx}} \tag{3.10}$$

which can be considered as a equation of line:

$$y = q + kx \tag{3.11}$$

where k is slope of the line not the Boltzmann constant. For multiple line intensities it is possible to obtain number of points and fit them by linear function expressed by equation 3.11. The fitted coefficient k (slope of line) can be used for evaluation of the temperature. The figure 3.1 shows such a Boltzmann plot for duralumin alloy sample with magnesium admixture. For temperature determination 8 neutral Mg lines have been used. The intensity of all lines from upper level 5.11 and 4.42 eV were corrected to self-absorption. The spectra was acquired from upper cold part of LIP (≈1.5mm from sample's surface) which is not so hot and temperature was determined to be ≈0.5 eV (5800 K).

The uncertainty in temperature determination performed by Boltzmann plot method is caused by uncertainty in determination of line intensities and by coefficients used in process of the intensity calculation. From the coefficients the most critical is Einstein coefficients of spontaneous emissions. The error can be less than 1%, but in the worst case it can reach tens of percents. Generally the uncertainty of temperature determination is coming from uncertainty of slope of fitted line determination. The high number of used lines with the high difference in the highest and lowest energy number (abscissa axis) should improve quality of fit and consequently temperature determination.

3.3 Saha-Boltzmann plot

At the end of the previous section, the high difference in energy of highest and lowest energy level in the ensemble of line intensities was suggested to improve the quality of Boltzmann plot fit. The energetic spectrum can by further extended to higher energies by combining ion and atom Boltzmann plots. For plotting of one mutual plot, the correction for relative concentration of ions with respect to atoms is necessary. Such a ratio is expressed by Saha equation 3.1.

If the density n in the Boltzmann expression 3.2 will be corrected by Saha equation 3.1 and intensity of line will be expressed by 3.1, the expression for

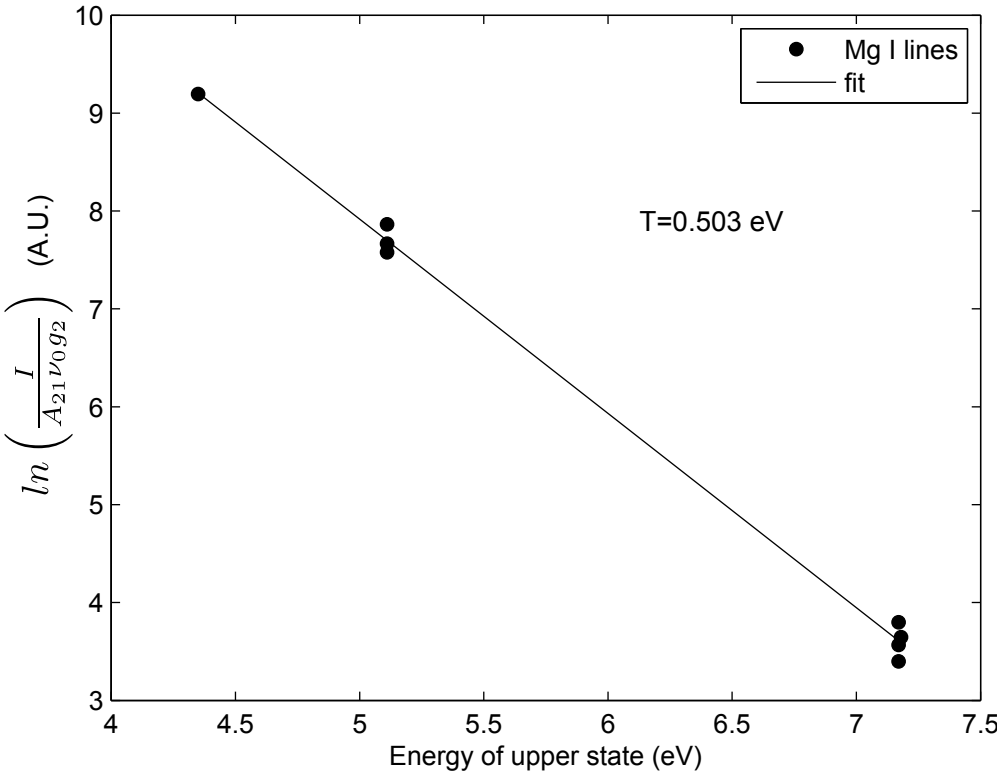

Figure 3.1: Boltzmann plot for duralumin sample. Temperature was determined by fitting of 8 Mg neutral lines.

Saha-Boltzmann plot can be obtained [8]:

$$\underbrace{ln\left(\frac{I^r_{ji}\lambda^r_{ji}}{A^r_{ji}g^r_j}\right) - rln\left(\frac{2\left(2\pi m_e kT\right)^{3/2}}{h^3 n_e}\right)}_{\text{y}} = \underbrace{ln\left(\frac{hcn^0}{4\pi Z^0(T)}\right)}_{\text{q}} - \underbrace{\frac{1}{kT}\left(E_j + E_\infty - \Delta E_\infty\right)}_{\text{kx}} \tag{3.12}$$

where n^0, $Z^0(T)$ are density number of neutral atoms and their partition function respectively and r is ionization state number. The second term on the right side of the equation is responsible for right shifting of the ion intensities with respect to neutrals. Saha-Boltzmann plot can contain more ionization states properly corrected by the term.

The temperature is usually determined in iterative approach of fitting intensities by linear function with respect to the temperature. The approach is possible, because the dependence of second term on the left side of equation 3.12 is slower than the $1/T$ on the right side of the equation. The function coefficients q and k are fitted as it is indicated by the under-braces 3.12.

An example of Saha-Boltzmann plot is shown in the figure 3.2. Two different slopes of lines fitted to neutral and ionic intensities are shown as solid and

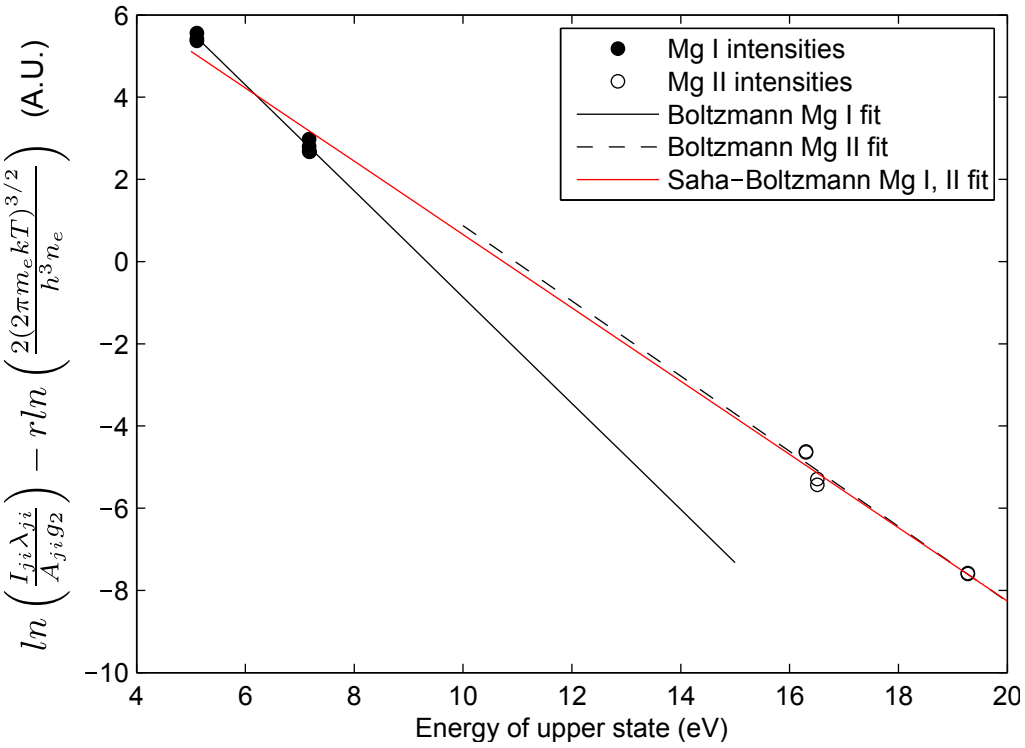

Figure 3.2: The Saha-Boltzmann plot for a duraluminium sample. The 7 Mg I and 6 Mg II lines were used for temperature determination. The Boltzmann plot temperatures for Mg I and Mg II are 0.77 eV and 1.09 eV respectively and for the Saha-Boltzmann plot the temperature 1.12 eV was determined.

dashed lines respectively. This indicates two different temperatures for neutrals and ions which differ from the one which was determined by Saha-Boltzmann plot represented by red line. Such a behaviour can be related to spatial integrated measurement of intensities rather than local measurement [3, 4, 5]. The temperature determined from intensities integrated in line of sight are referenced to be apparent temperatures.

3.4 CF-LIBS

The goal of the calibration free (CF) LIBS is to estimate a sample composition without previous calibration of compositions vs. emission line intensities. Such a possibility was first proposed by Ciucci et al. [23] and its application on aluminium alloy samples was presented. Subsequently, some other applications on aluminium [97, 61, 101, 23], cooper based [80, 40, 6, 22] or other alloys have been presented. The composition of various types of samples like meteorite [42] or coral skeleton [79] was determined by this method.

The conservation of sample stoichiometry in the plasma is important assumption of the method. Additionally, the LIP must be in LTE and optically thin. Under these assumptions temperature can be determined for investigated plasma from emission lines of different elements and ionization stages. Both expressions 3.10 and 3.12 contain in the q-term on the right site densities n or n^0. In the case of Boltzmann plot n relates to densities of considered specie (atom or ion), but in the case of Saha-Boltzmann plot n^0 relates to densities of neutral atoms of considered element. The densities can be expressed in term of concentrations as $n_i = c_i n$ where n is sum of all species densities occurred in LIP.

Let us assume that a sample is composed of N different elements. If Boltzmann plot is drawn for every specie (atom and ions), the interceptions q_i and q_j contain information about a relative concentration of i and j species as:

$$\frac{c_i}{c_j} = \frac{Z_i(T)}{Z_j(T)} e^{q_i - q_j} \tag{3.13}$$

where $Z(T)_i$ and $Z(T)_j$ are partition functions of species and c_i and c_j are their concentrations respectively. As $\sum_{i=1}^{N} c_i = 1$ previous expression can be written as:

$$c_i = \frac{Z_i(T) e^{q_i}}{\sum_{j=1}^{N} Z_j e^{q_j}} \tag{3.14}$$

from which the concentrations of all species can be determined. For determination of composition for some element only addition of neutral and ion species concentrations is needed.

Usually, not all species of all elements are successfully used for a Boltzmann plot construction. All missing species can be derived from other species of the same element if at least specie of the element one is present. For example if Boltmann plot for neutral atom is constructed and its concentration is determined, ion concentration can be also calculated. Such a calculation can be performed by Saha expression 3.1 but electron density number is needed. It can be obtained from Stark broadening phenomena [53, 55, 102], or again from Saha expression, when Boltzmann plots for two different species of the same element are available.

Also SB plot can be used for concentration calculations which are usually more accurate because of lower uncertainties in the interception determination as it was mentioned in section 3.3. Saha expression 3.1 needs to be used for derivation of densities of ions from neutral concentration. For this purpose electron densities number must be known which can be estimated as it was mentioned above. Combination of Boltzmann with SB plot for CFLIBS is possible with usage of Saha equation.

The figure 3.3 shows the plots calculated by Saha equation for magnesium and strontium to present the relative abundance evolution of ionization states with the temperature for three different electron densities. Evolution is very different for magnesium and strontium. Usually doubly ionized ions are not included in CFLIBS analyses, but whereas for magnesium for $n^e = 10^{17}$ cm^{-3} and $T = 1$ eV the abundance of doubly charged ions is negligible, for strontium the abundance reaches 80%. Such a high value can produce result in concentration which is not correct and so the doubly charged ions must be included in analyses. Their significance should be considered even in case of magnesium for high electron densities and high temperatures.

Low optical thickness was declared to be necessary for successful composition determination by CFLIBS. However, there are some publications treating low optical thickness by different ways and some of them are presented in section 4.1. Also publication about a correction in disproportion of plasma stoichiometry have been published [61].

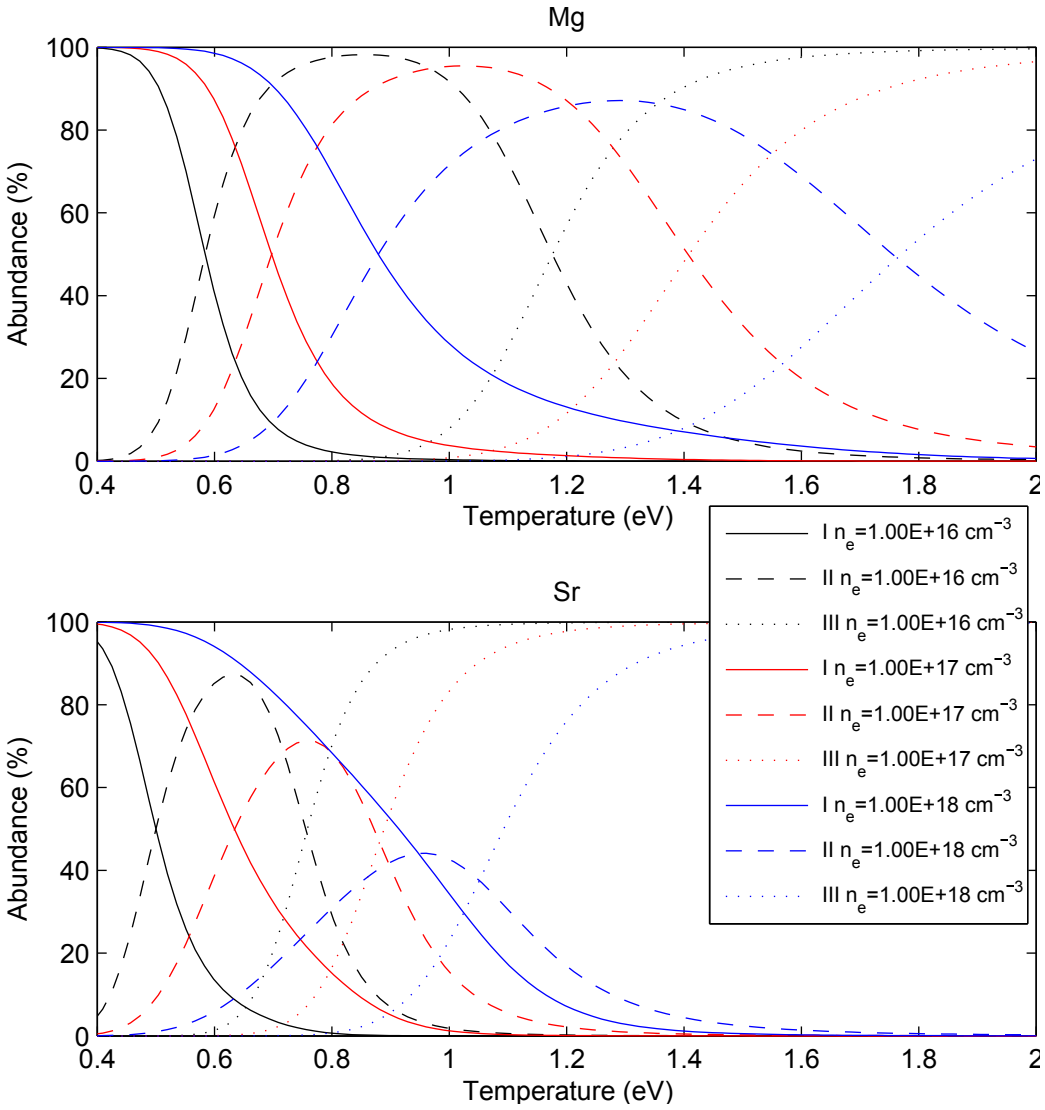

Figure 3.3: The relative abundance evolution of the magnesium and strontium neutrals, singly and double charged ions with respect to ionic temperature. The evolution is shown for electron densities 10^{16}, 10^{17} and 10^{18} cm^{-3}.

3.5 Measurement of Echelle's spectrometer spectral response.

3.5.1 Introduction

A spectral response measurement of an echelle-type spectrometer (Andor Mechelle ME5000 spectrograph coupled with Andor iStar DH734 camera) in the spectral range of 215 to 950 nm is described in this section. The Echelle type spectrometers are frequently used in LIBS applications because of their wide spectral band and high spectral resolution [64]. Such a spectrometer is also located at laboratory in Bratislava where it is used for research in LIBS. The aim was to have a spectrometer which will provide measurements of LIP with possibility to determine temperature by Boltzmann and Saha-Boltzmann plot and which will offer possibilities for quantitative analyses based on calibration free methods. For such a purpose all acquired spectra must be corrected with respect of spectral response of the spectrometer to provide proper relative intensity ratios in over all spectral band used in analyses. The presented procedure of calibrating was presented at the conference [88].

The spectral response of the echelle's type spectrometers contains lot of local maxima and minima within all its spectral range. A source of continuum radiation with known spectral distribution looks to be very useful for a determination of the response. Echelle's bandwidth easily ranges from ≈200 to ≈900 nm and there is no continuum source radiating in the whole range. Two different sources of the continuum radiation with overlapped region between 330 and 380 nm have been used in presented calibration process.

The tungsten filament lamp was used for the visible and near infrared part of the spectra in range of 330–950 nm. The lamp was considered as black body radiator and its temperature was determined. With known temperature the spectral radiation density ($\mathrm{Wm^{-2}nm^{-1}}$) can be described by Plank function [66]:

$$B(\lambda, T) = \frac{2\pi hc^2}{\lambda^5} \frac{1}{e^{-hc/\lambda kT} - 1} \tag{3.15}$$

where T is temperature of the black body radiator, λ is a wavelength and h, c and k is Planck constant, speed of light, and Boltzmann constant respectively. The temperature of the filament was determined as it is described later.

For the ultraviolet (UV) part of the spectra in range of 215–380 nm the deuterium arc lamp was used, whose spectral distribution is unfortunately not possible to describe in so simple way as the filament lamp's. There are

certified deuterium lamps with measured spectral distribution of its radiation available on the market, but they are very expensive. Because of the price, the calibration of uncalibrated deuterium lamp was performed in the laboratory in Bratislava.

The simulation of diatomic molecular spectra have been used for the temperature determination of the lamp's filament and for calibration of the deuterium lamp. The spectra were generated by a DC glow discharge in air at low pressure. Similar principle was used in [14] but additional spectrometer is used in presented calibration procedure. The goal was to eliminate complicated Echelle's spectral response with simpler spectral response of Czerny-Turner spectrometer.

3.5.2 Echelle type spectrometer

The advantage of echelle in comparison with classic Czerny-Truener designed spectrometers is high band width and high resolution. Such properties are achieved by dispersion of the light by two orthogonal elements. Incoming light is dispersed not only to one dimension but to two dimension, so the spectra is covering some surface (see figure 3.4). As dispersion elements optical prism and Echelle grating is used.

Echelle grating has step-like profile grooves. The grooves are covered by high reflecting coating. The angle between normal to grove and normal to grating is called blazed angle. When the addition of incident angle and dispersion angle is twice of blazed angle, efficiency of grating is maxima and can reach 70 % [64]. High spectral range can be covered by Echelle grating which is working in a high diffraction orders. One only needs to separate the wavelength in different orders to be distinguishable. The optical prism is used for this purpose.

3.5.3 Experimental

The fig. 3.5 shows the experimental apparatus with the light sources and spectrometers. As a source of molecular spectra containing the vibration-rotational structure, a DC glow discharge is used [15]. The discharge was maintained in the air under pressure of ≈2.5 Torr. In the discharge the radiation of NO, N_2 and OH diatomic molecules were dominant and covering all the spectral range needed for calibration (see fig.3.6). Their spectra have been simulated and used for the lamp's filament temperature determination and for calibrating of

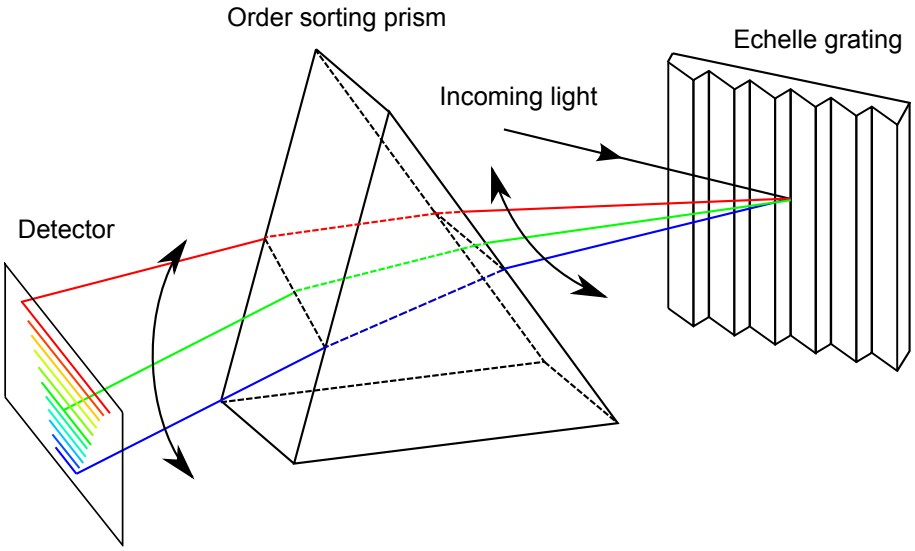

Figure 3.4: Scheme of echele spectrometer's dispersion system.

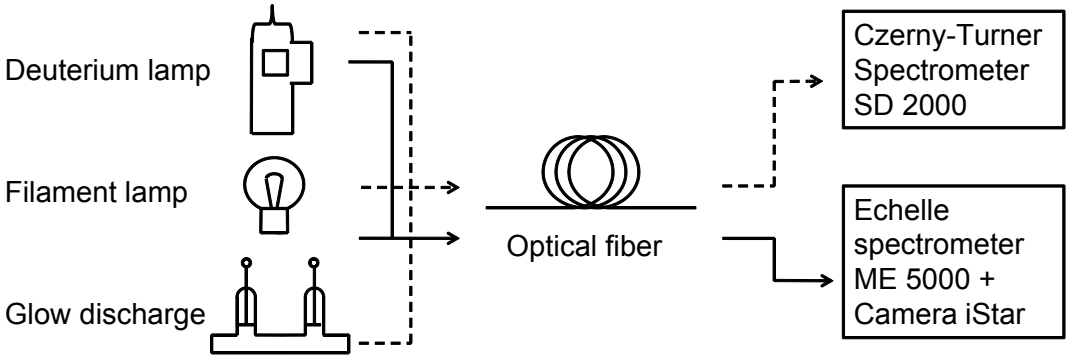

Figure 3.5: Scheme of the apparatus for spectral response measurement.

the deuterium lamp.

The radiation described by transition $NO\,(A^2\Sigma^+ \rightarrow X^2\Pi)$ (NOγ system) was dominant [14] for the NO molecules. So called Second positive system (2PS)was dominant for N_2 molecules and this system is described by transition $N_2\,(C^3\Pi_u \rightarrow B^3\Pi_u)$ [20]. Two systems are overlapped in the region between 280 and 320 nm with additional mixing of OH system with transition $OH\,(A^2\Sigma^+ \rightarrow X^2\Pi)$ as it can be seen in the figure 3.12.

Both spectra for NO_γ and OH systems have been simulated by LIFBASE software [1]. In case of NO_γ first six vibration bands have been simulated for rotation temperatures between 1400 and 2500 K with step of 100 K. The spectra have been exported separately for every vibration band. The exported data have been processed by developed computer program. The program generates

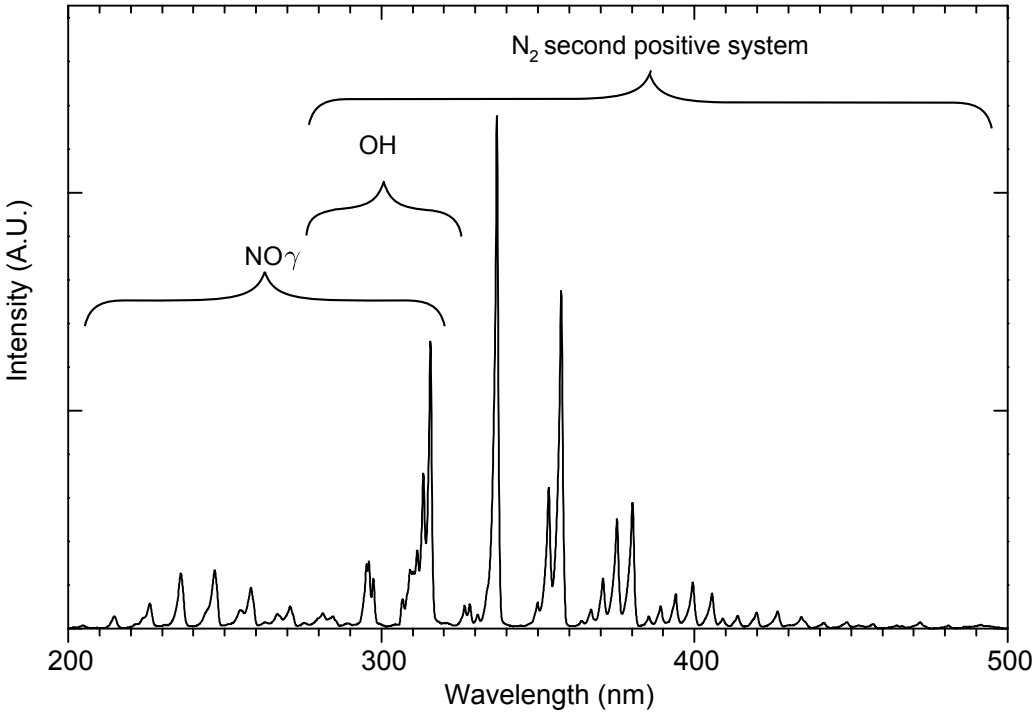

Figure 3.6: Spectra of the air in glow DC discharge with pressure of 2.5 Torr. There are three dominated molecular systems and they are marked above the spectra.

spectra for any rotation temperature T_r in range as they were exported from LIFBASE by interpolation. It also redistributes vibration-rotation population according to Boltzmann distribution related to some vibration temperature T_v. By generating of the spectra in this way, the program can fit them to experimental data by varying of T_r and T_v. For the OH system only two vibration bands have been generated for rotation temperatures between 300 and 2300K with step of 200 K.

The 2PS was also fitted by the developed program, but simulated data have been exported from Specair software [96]. Spectra have been exported with no separated vibration bands and temperatures have been determined in iterative process by fitting alternately T_r and T_v as it will be described later.

As the filament lamp a small bulb lamp was used, powered by 8 V and 4 A with nominal lamp voltage 6 V. The lamp was powering with higher voltage in order to reach high temperature of filament what results in higher radiation in UV part of spectra. The bulb was made of not special glass and it starts to be opaque for light from 340 nm down to lower wavelengths.

The deuterium lamp was powered by circuit as it is shown in the fig. 3.7. In order to prevent harm of the lamp and to increase its live time, flowing operation process was done :

1. Slow filament heating was needed, so current measured by $A1$ was raised slowly from 0 to 3 A (max. 3.5 A). The heating current indicated by $A2$ was 0 A and resistance was to its maximum value.

2. After reaching of the wanted current value, heating of the lamp filament was kept for ≈1 minute.

3. After 1 minute the anode current indicated by $A2$ was raised until discharge started to burn in the lamp.

4. The heating current was reduced to 2.5 A and the anode current was set to 0.3 A. The voltage indicated by V was ≈70 V.

5. The deuterium lamp was let to stabilize for 30 minutes.

In process of switching off:

1. The anode current was reduced to 0 A.

2. The heating current was slowly reduced to 0 A.

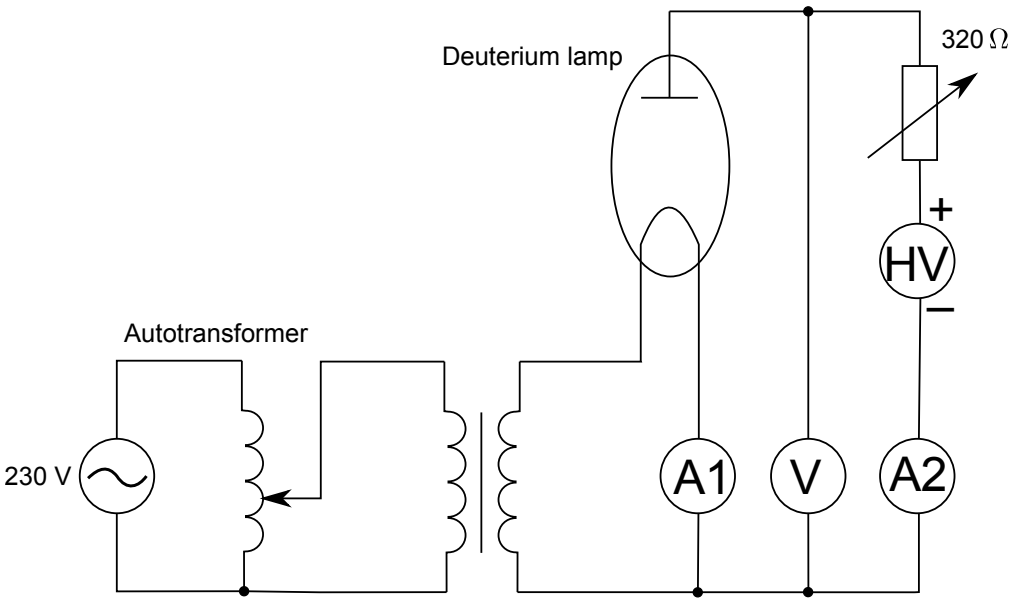

Figure 3.7: The circuit for powering of deuterium lamp.

Ocean Optics SD2000 Czerny-Turner type spectrometer was used as second spectrometer. Its spectral range is 200-550 nm and mean resolution ≈0.6 nm. All simulated spectra were convoluted by instrumental function obtained by measurement of the emission from HG-1 Mercury Argon Lamp from Ocean Optics. The emission lines are considered to be narrow enough in comparison with the instrumental function [92] of the spectrometer. The convolution with Hg line from 253.65 nm was performed for NO $_\gamma$ and OH spectra and convolution with line from 404.66 nm was used for 2PS spectra.

3.5.4 Measurement of spectral response.

Overall process of spectral response measurement of Echelle spectrometer is shown by diagram in the fig. 3.8. First stage of the process represents measurement of spectral response of SD2000 spectrometer and the tungsten filament lamp temperature determination. For this purpose simulation of molecular spectra and its fit to experimental data was done. In second step the deuterium lamp will be calibrated by using of the spectrometer SD2000. As the last step the reconstruction of Echelle's spectral response from the calibrated deuterium lamp and tungsten filament with known temperature will be done.

NO gamma fit The fit was performed in three steps. In the first step the fit of rotation temperature, vibration distribution and points of spline

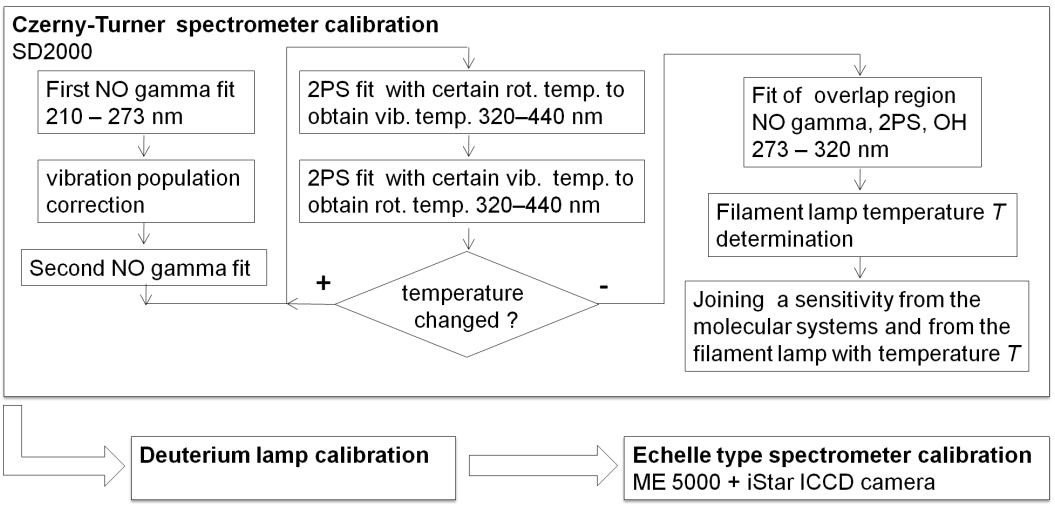

Figure 3.8: Block diagram for the calibration procedure. Spectral response of Czerny-Turner spectrometer was determined firstly. Subsequently, the relative radiation of the deuterium lamp was found and then the sensitivity calibration of Echelle spectrometer was done.

line in region 210-273 nm was done. The spline line was considered as the spectral response curve and it was used for correction of simulated spectra to fit the experimental data. It consisted of four points with fixed wavelength and variable y-coordinate used in the fit process (see 3.10).

Higher vibration states did not fit well and were apparently too intensive as it is marked by arrow on the left fig. 3.9. On the right fig. 3.9 the good agreement of first three vibration states with Boltzmann distribution can be seen. The assumption of Boltzmann distribution characterized by temperature T_v was applied in second step to reduce simulated intensities for two last vibration states. The difference between corrected and uncorrected vibration states can be seen on the right fig. 3.9.

In the third step new fit of NO_γ was applied with fixed vibration temperature 3400 K. The spectral response curve from fit and the first three vibration bands are shown in the 3.10. Rotation temperature was determined by fit to value 2140 K.

The difference in vibration and rotation temperatures is common for some of types of discharges even they can be described by one temperature separately [83, 20].

N_2 Second positive system fit Fit of the 2PS in the region between 320 and 440 nm was performed in iterative process presented by loop in the fig.3.8.

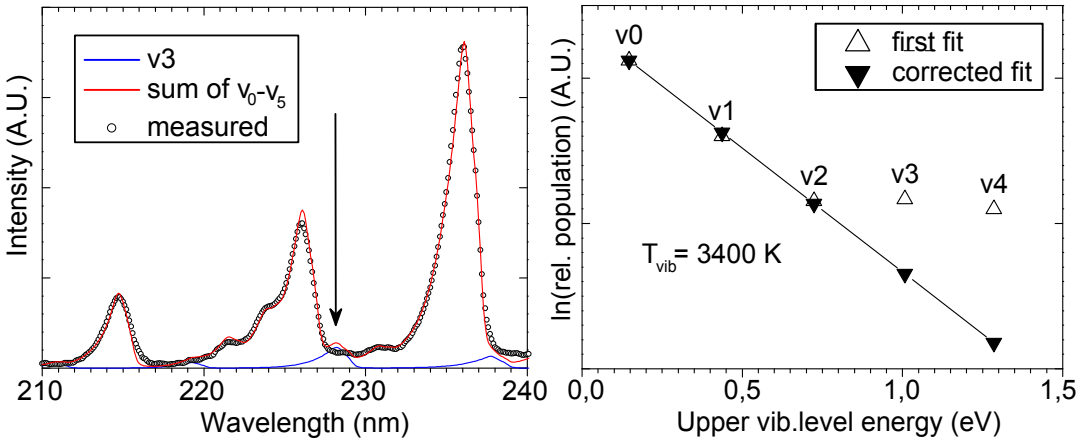

Figure 3.9: Left figure shows part of measured and simulated spectra of NOγ system. Sum of first six simulated vibration bands (v_0-v_5) is shown and a bad fit of 3^{rd} vibration band (v_3) is marked by the arrow. Uncorrected and by Boltzmann plot corrected (v_3 and v_4) population levels are shown on the right figure.

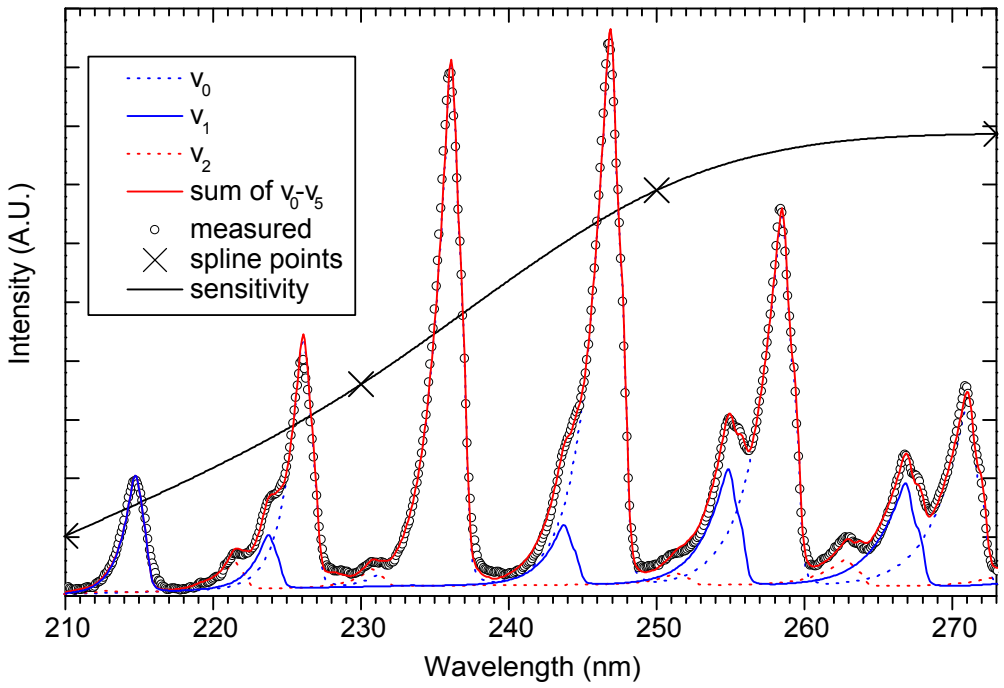

Figure 3.10: Fit of simulated (red line)and measured (circles) spectra of NOγ. First three vibration bands (v_0-v_2) are explicitly shown indicated as dashed blue, solid blue and dashed red line. Sensitivity correction is fitted by four spline points.

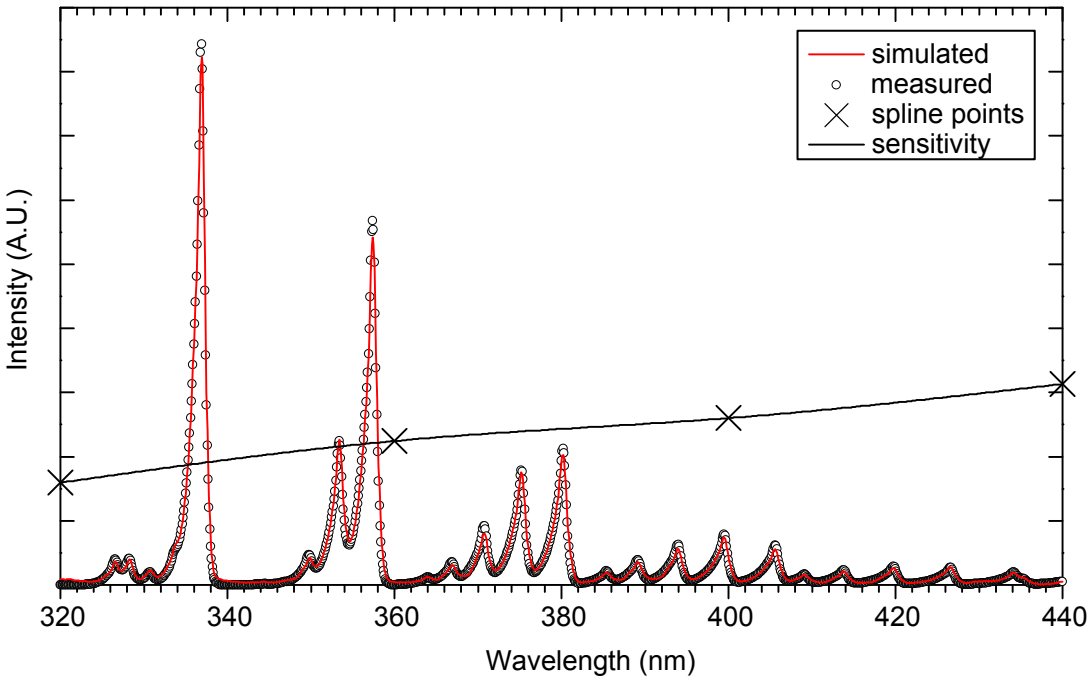

Figure 3.11: Fit of simulated (red line) and measured (circles) spectra of 2PS. Sensitivity correction is fitted by four spline points.

In the process the spectra in some range of temperature (T_r or T_v) were generated by Specair software and fitted by varying that temperature. For obtained fitted temperature new spectra for other temperature have been generated and the data used for fit. Obtained temperature was again used for spectra generating for the first temperature and the process was repeated until both temperatures have been stabilized. The rotation and vibration temperatures were determined to be 800 K and 5260 K respectively. The spectral response was fitted by spline line in same way as in NO_γ fit. Final simulation with fitted sensitivity response is shown in the fig.3.11.

Fit of overlap region The spline line and the ratio between intensity of NO_γ and 2PS in range form 260 to 320 nm was determined by fit with fixed rotation and vibration temperatures, determined previously. To improve the fit quality the OH system simulation was added as it is obviously presented (see 3.12).

Filament temperature determination The temperature of the filament of the tungsten filament lamp was determined for reconstruction of VIS part

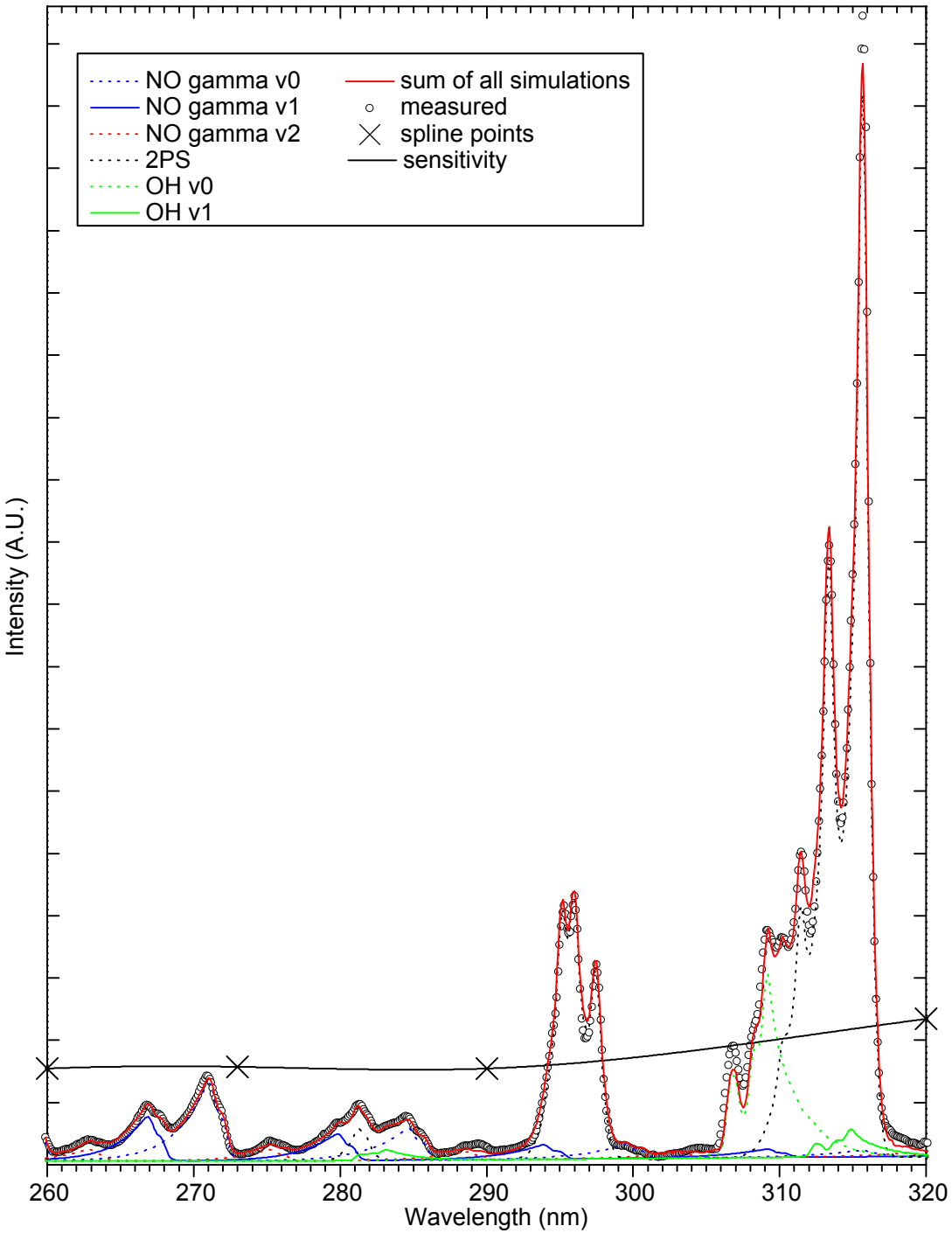

Figure 3.12: The spectra region of the three overlapped molecular systems. Simulation of the first three NOγ v_0-v_2 and first two OH v_0-v_1 and not separated second positive system's (2PS) vibration bands are shown. Sum of the all bands and its fit to experimental spectra are presented as red line and circle respectively with sensitivity correction curve fitted by four spline points.

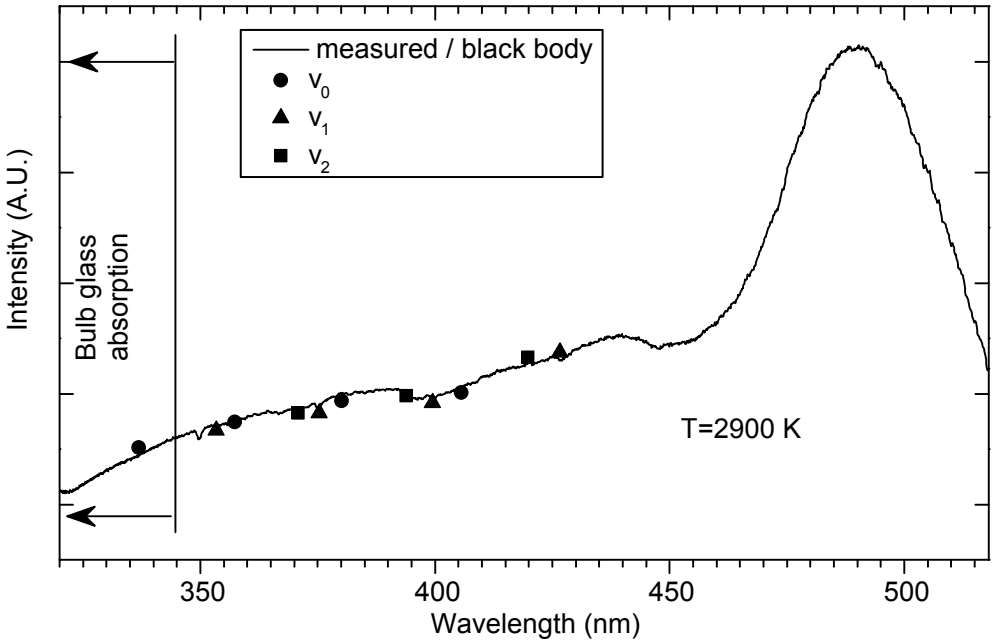

Figure 3.13: Filament temperature determination. Ratios of measured to simulated of first three vibration bands (v_0-v_2) of 2PS were scaled to fit them to sensitivity derived from filament radiation with simulated temperature also fitted.

of the spectral response. Ratios of simulated to measured intensities (averaged around the maximum of vibration band head) of the first three vibration bands were scaled independently to fit them to ratio of simulated to measured filament radiation with certain temperature, which was also fitted. That means that in process of fitting vibration transitions from same upper vibration state it was scaled by one coefficient and then ratio to measured intensities was done. The ratios were fitted to ratios determined from measured and simulated black body radiator with certain temperature which was also fitted to find the best temperature. The filament radiation was simulated by Plank law of black body radiator 3.15. Only transitions above 340 nm were taken for the fit, because of a strong bulb glass absorption starting from ≈340 nm to shorter wavelengths. The temperature of the filament was determined to a value of 2900 K (see fig.3.13).

Spectral response of SD2000 With UV and VIS sensitivity parts, it is possible to create a spectral response of the SD2000 spectrometer in its whole spectral range. The connection of the parts was done in wavelength ≈360 nm (see left fig.3.14). Consequently, by using the obtained spectral response, rel-

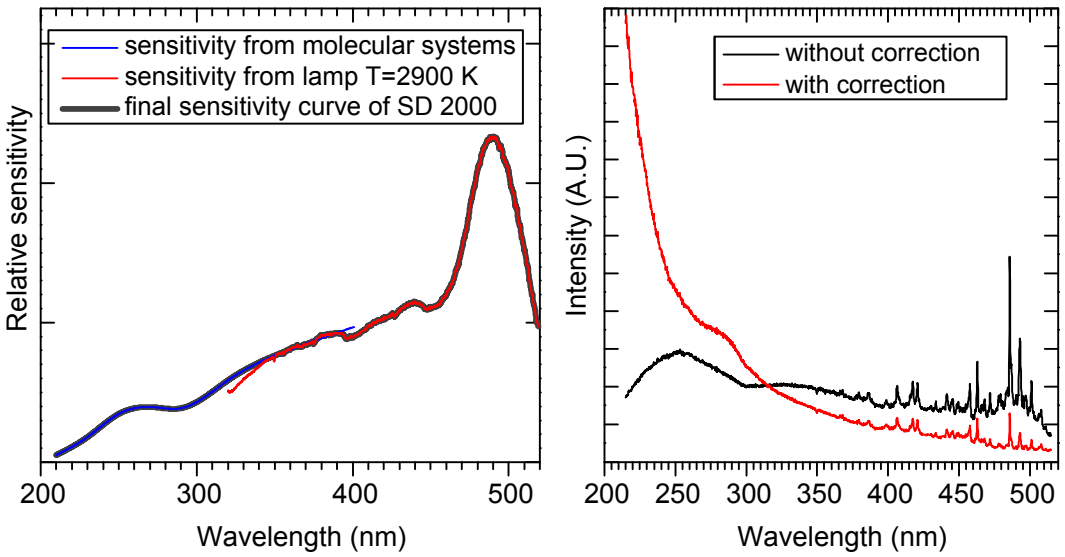

Figure 3.14: There are spectral response curves in the left figure. The final one is composed in VIS part of sensitivity derived from a tungsten filament lamp and in UV region of sensitivity determined by NO_γ and 2PS simulation. In the right figure the spectrum of a deuterium lamp radiation is shown.

ative radiation of the deuterium lamp was determined. Difference before and after correction can be seen in the right fig.3.14.

Echelle calibration Radiation from the filament and deuterium lamp was measured with spectrograph ME 5000 equipped with iStar ICCD camera. A previous calibration of lamps was used to calibrate the Echelle spectrometer in two separate parts. Those parts were joined to create one spectral response curve for the whole spectrometer spectral range of 215–950 nm. Zoomed overlap region of both spectral responses is shown in the left top corner of fig.3.15. Joining point is ≈360 nm. Notice decrease of spectral response derived from filament lamp below 340 nm caused by bulb glass absorption.

3.5.5 Results

The calibration of an Echelle type of spectrograph coupled with ICCD camera was presented. Quality of its spectral response determination is dependent on a quality of Czerny-Turner SD2000 spectrometer calibration and filament temperature determination. The simulation and the fit of vibration-rotation bans of spectra were separated in three regions. Quality of fit in all parts of spectra was affected by background and emission bands of undefined and not

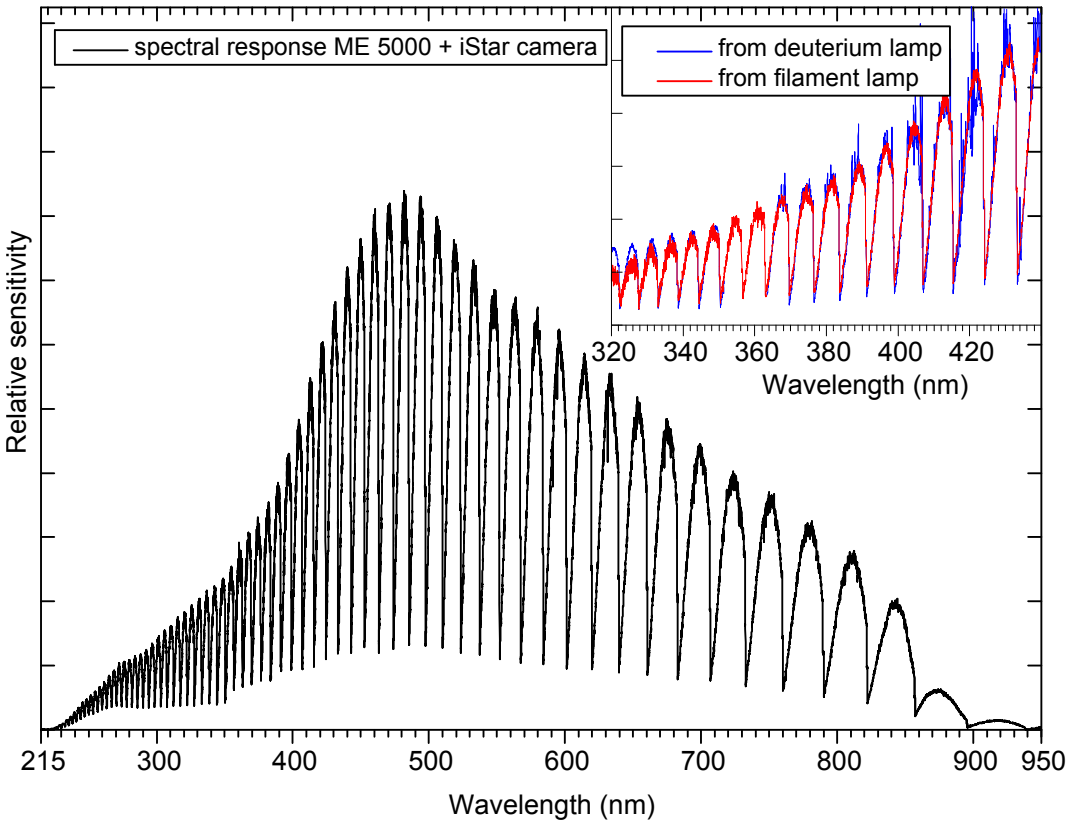

Figure 3.15: Spectral response curve of ME 5000 coupled with iStar ICCD camera composed from two parts. In the left top corner, a connection region of two spectral response curves is shown.

simulated transitions. The critical part for the fit is overlapped one, because it assesses ratio between the UV and VIS parts. The simulation and fit of OH system was performed to improve fit in this part. Shape and width of the instrumental function was measured for two different spectra region, and its convolution with simulated spectra were applied. In the case of filament temperature valuation, the used method was limited by bulb glass absorption.

For relative intensity measurement of atomic lines in LIBS experiments, it is important to know the spectral response of spectrometer?. By presented calibration process, usage of an expensive calibrated UV radiation source was bypassed. Less than 10 % error was reached in the region of 215-273 nm. An error in between UV in IR part is even higher, mainly because of uncertainty in fit of the overlapped part of NO gamma and 2PS. It is estimated to be not higher than 30 %. This precision is satisfactory for many LIBS applications. For example, one need to consider up to 30 % error coming from Einstein spontaneous emission coefficients in order to determine electron state population. Additional improvement can be done by better reference radiation sources.

3.6 Analyse of aluminium alloys

3.6.1 Introduction

In the previous section the measurement of spectrometer's spectral response was presented. The spectral response is needed for LIP temperature determination by Saha-Boltzmann plot method as well as for the composition estimation of samples by CF-LIBS. Following section will present application of the measured spectral response for the temperature and composition determination on aluminium alloys samples with various nominal composition.

Apparatus was set up to acquire spectra only from a small part of LIP. Considerable difference was noticed in shape of some spectral line profiles and their intensities acquired from different plasma locations above the sample surface. Such a behaviour was assumed to have important influence on quality of obtained results from CF-LIBS. Two different location distant 1 mm and 2 mm from the sample surface have been measured and the obtained results were compared.

Because of big amount of data, the software programmed for developed LIBS portable device presented in section 2.2 has been extended for a further functionality. For fitting of partly overlapped peaks the single peak fit was extended to multi peak fit. Additionally, immediate usage of the fitted

intensities for SB plot construction and consecutive composition calculation was also implemented. Functionality is very interactive with respect to adding and removing lines included to calculations and checking their fit quality. The extension uses the same spectroscopic database as the base software.

3.6.2 Experimental

The used apparatus was similar to that one shown in figure 1.1. The Nd^{+3}:YAG laser BRILIAN from company Quantel was used as laser source. It is equipped with second harmonic generation able to deliver maximum energy 165 mJ at 532 nm with pulse duration ≈5 ns. All measurements have been performed by laser energy 57 mJ with repetition rate 0.3 Hz (laser offers repetition rates up to 10 Hz). The laser beam was focused on the surface by lens with anti-reflection coating on 532nm, with focal length 70 mm.

Light coming form LIP was collected by CaF_2 lens with diameter 1" with focal length 40 mm to the optical fibre connected to the spectrometer. The distance of the lens from the fibre and from sample was adjusted to produce image of plasma 2x magnified in plane of fibre. The magnification was chosen for better location of site observed in LIP and to prevent integration of light from big volume, even the integration in line of sight was not eliminated. The fibre diameter was 635 μm what theoretically means ≈300μm spot production by fibre aperture imagined by the lens in plane of sample. But because of geometric and chromatic aberration, the image was not sharp. Aperture with diameter ≈6 mm had been placed in front of the lens to improve disused issue. The Mechelle 5000 spectrometer equipped with iStar DH734 camera both from company Andor was used for spectroscopic measurements. Its calibration process is described in 3.5. The camera of spectrometer has been synchronized with laser by trigger pulse generated by the laser.

All measurements have been done in air atmosphere under normal pressure without gas flowing. Every spectra has been acquired with exposition time of 200 ns and delay of 1500 ns after laser trigger. In measuring process, accumulation of 10 shots to 5 different sides has been used to prevent influence of inhomogeneity and too deep crater production and so to avoid change of plasma parameters from first to last shot. The spectra from first shot is usually much more intensive than spectra from following shots, additionally we suppose that there is difference on a flat surface and in a crater in early plasma formation. So first two shots have been rejected as too different in respect to plasma parameters and consequent spectra intensity. For horizontal moving of

sample a translation stage was used .

Aluminium alloy samples have been used in the presented analysis. They were collected from various sources with aim to cover the highest possible composition range for magnesium. The table 3.1 shows a list of used samples with their nominal compositions in percentage for five elements. The nominal composition was obtained by measuring of samples by scanning electron microscope (SEM) in other laboratory. The method of energy-dispersive x-ray spectroscopy (EDS or EDX) was used with processing of spectra by commercial software delivered with the electron microscope. To eliminate influence of samples dimensions to experiment, every sample was prepared to have the same dimensions (4x4x10 mm). Additionally, the samples have been cleaned in ultrasound cleaner to eliminate pollutions coming from grease during machining.

Sample	Mg	Al	Si	Mn	Cu
S1	0.78	96.05	0.37	0.52	2.25
S2	1.67	95.68	0.08	0.25	2.28
S3	4.08	95.09	0.37	0.41	0.02
S4	0.50	98.81	0.55	0.02	0.03
S5	3.20	96.30	0.24	0.17	0.00
S6	3.32	95.88	0.49	0.20	0.05
S7	0.62	96.53	0.49	0.61	1.71
S8	5.13	94.63	0.07	0.12	0.02
S9	3.01	96.64	0.19	0.08	0.02

Table 3.1: Used samples with their nominal composition in percentage measured by SEM.

3.6.3 Data processing

All spectra have been divided by the spectral response of spectrometer presented in 3.5. Emission lines presented in the spectra have been identified and if line profile quality was sufficient for fit, they have been selected for further processing. All selected lines have been fitted to pseudo-Voigt profile. The fit provide possibility to determine intensity of lines without background determination even for lines partly interacting with other lines. Additionally, information about Lorentz width was obtained by fit. Lorentz width is caused by Stark effect and it was used for determination of electron's density number as it is written later. Instrumental function of spectrometer, considered as Gauss profile, was set steady in fitting process and set for every line as

$\Delta\lambda = \lambda/4200$. The Gauss width caused by Doppler broadening was neglected as it is much more lower than instrument function.

		λ (nm)	A_{21} (s^{-1})	E_1 (eV)	E_2 (eV)	g_2
Mg	I	277.669	1.31E+08	2.71	7.18	5
Mg	I	277.827	1.78E+08	2.71	7.17	3
Mg	I	277.982	1.31E+08	2.71	7.17	3
Mg	I	277.983	3.95E+08	2.72	7.18	5
Mg	I	278.142	5.31E+08	2.71	7.17	1
Mg	I	278.297	2.18E+08	2.72	7.17	3
Mg	I	285.213	5.09E+08	0.00	4.35	3
Mg	I	516.732	7.77E+06	2.71	5.11	3
Mg	I	517.268	3.29E+07	2.71	5.11	3
Mg	I	518.36	5.46E+07	2.72	5.11	3
Mg	II	279.078	4.08E+08	4.42	8.86	4
Mg	II	279.553	2.69E+08	0.00	4.43	4
Mg	II	279.8	4.81E+08	4.43	8.86	6
Mg	II	280.271	2.62E+08	0.00	4.42	2
Mg	II	292.863	1.12E+08	4.42	8.66	2
Mg	II	293.651	2.22E+08	4.43	8.66	2
Mg	II	448.132	2.15E+08	8.86	11.63	6
Mg	II	448.113	2.28E+08	8.86	11.63	8
Al	I	265.248	1.34E+07	0.00	4.67	2
Al	I	266.039	2.65E+07	0.01	4.67	2
Al	I	305.007	3.21E+07	3.60	7.67	6
Al	I	305.468	4.49E+07	3.60	7.66	4
Al	I	305.714	7.50E+07	3.61	7.67	6
Al	I	306.429	8.92E+07	3.60	7.65	2
Al	I	306.614	4.77E+07	3.61	7.66	4
Al	I	308.215	6.27E+07	0.00	4.02	4
Al	I	309.271	7.55E+07	0.01	4.02	6
Al	I	394.401	5.11E+07	0.00	3.14	2
Al	I	396.152	1.01E+08	0.01	3.14	2
Al	II	281.618	3.93E+08	7.42	11.82	1
Al	II	466.306	5.30E+07	10.60	13.26	3
Al	II	704.206	5.90E+07	11.32	13.08	5
Al	II	705.66	5.80E+07	11.32	13.07	3

		λ (nm)	A_{21} (s^{-1})	E_1 (eV)	E_2 (eV)	g_2
Al	II	706.364	5.80E+07	11.32	13.07	1
Cu	I	324.754	1.37E+08	0.00	3.82	4
Cu	I	327.395	1.36E+08	0.00	3.79	2
Cu[1]	I	515.323	1.03E+08	3.79	6.19	4
Cu[1]	I	521.82	1.22E+08	3.82	6.19	6
Mn[2]	I	353.211	1.99E+08	2.28	5.79	4
Mn[2]	I	353.199	1.28E+08	2.28	5.79	6
Mn[2]	I	353.183	5.34E+07	2.28	5.79	8
Mn	I	403.075	1.74E+07	0.00	3.08	8
Mn	I	403.306	1.65E+07	0.00	3.07	6
Mn	I	403.448	1.58E+07	0.00	3.07	4
Mn[3]	I	404.135	7.87E+07	2.11	5.18	10
Mn[3]	I	404.874	7.54E+07	2.16	5.23	4
Mn[3]	I	405.554	4.31E+07	2.14	5.20	8
Mn	II	259.372	2.64E+08	0.00	4.78	7
Mn	II	260.568	2.71E+08	0.00	4.76	5
Mn	II	262.561	2.83E+08	3.42	8.14	11
Mn[4]	II	270.17	2.59E+08	3.42	8.00	13
Mn[4]	II	270.573	2.26E+08	3.42	8.00	11
Mn[4]	II	270.845	2.03E+08	3.42	8.00	9
Mn[4]	II	271.033	1.91E+08	3.42	7.99	7
Mn[4]	II	271.162	2.08E+08	3.42	7.99	5
Mn	II	293.305	1.96E+08	1.17	5.40	3
Mn[4]	II	293.931	1.86E+08	1.17	5.39	5
Mn	II	294.921	1.86E+08	1.17	5.38	7
Mn	II	346.032	3.21E+07	1.81	5.39	5
Si	I	251.432	6.11E+07	0.00	4.93	3
Si	I	288.158	1.89E+08	0.78	5.08	3

Table 3.2: Spectroscopic data.

The selected lines with spectroscopic data are presented in the table 3.2.

[1]not selected for S3, S4, S5, S6, S8 and S9

[2]not selected for S2, S4, S5, S6, S8 and S9; not at all selected for 1 mm distance measurement

[3]not selected for S4, S5, S6, S8 and S9

[4]not selected for S4

Notice foot notes marking lines which have not been used for in case of all samples. The restricted lines were not possible to be identified or fitted because of low concentration of related elements in the samples. Some lines related to the same specie and to the same upper energetic level, even completely interacting, were also selected and fitted by one Voigt profile which included the interacting lines. The intensities of included lines were obtained by splitting of the fitted area in ratios proportional to their $A_{21}g_2$ product.

The composition of samples have been determined by CF-LIBS method as it is described in 3.4. For this purpose SB plots have been created. The electron density incoming to calculation of SB was determined by using of Stark broadening coefficients for two selected lines. The first one, Hα line has been treated in accordance of Advance Generalized Theory (AGT) of Stark broadening by using of tabulated coefficient [102]. The AGD is more accurate for the reached electron densities than usually used Kepple-Griem theory [53]. As the second one, the line Cu 521.82 nm has been selected and density was determined by a coefficient published in [55]. The LIP was considered to have equal electron density number for all samples and average of all spectra have been performed in order to Lorentz width determination. Such an approximation is correct, because the samples are mainly composed of aluminium (>94%) and its relative abundance is changing <2%. Additionally, the left figure 3.16 shows that for the lowest experiment temperature 1 eV aluminium ion abundance does not fall under 80 %1 eV, so the electron density is mainly ordered by aluminium. The determined densities are tabulated in table 3.3. In further analysis we used average of two values.

	n_e 1 mm $10^{17}(cm^{-1})$	n_e 2 mm $10^{17}(cm^{-1})$
Hα 656.285	2.84	2.37
Cu 521.820 nm	2.68	2.09
average	2.76	2.23

Table 3.3: Electron densities obtained for two different lines for two locations in LIP.

The error presented in temperature and composition results has been estimated as error in slope and interception resulting from linear fit of points with exact E_i value and with uncertainty σ_i in intensity values. The standard deviation of measured intensities have been considered as source of uncertainty. For uncertainty in the slope and the interception, the following expressions

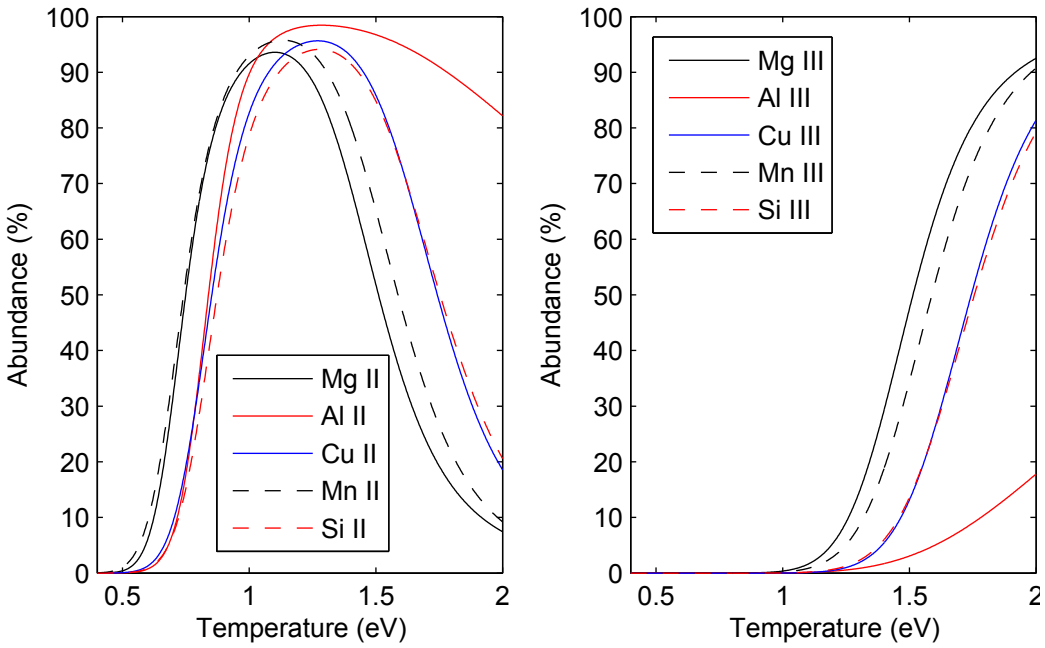

Figure 3.16: Abundance of singly and doubly ionized ions for different elements dependent on temperature for electrons density number 2.23 10^{17} cm^{-3}.

have been used [85]:

$$\begin{aligned} \sigma_q^2 &= S_{xx}/\Delta \\ \sigma_k^2 &= S/\Delta \end{aligned} \tag{3.16}$$

where:

$$S_{xx} = \sum_{i=1}^{N} \frac{x_i^2}{\sigma_{i^2}} \quad S = \sum_{i=1}^{N} \frac{1}{\sigma_{i^2}} \quad \Delta = SS_{xx} - \left(\sum_{i=1}^{N} \frac{x_i}{\sigma_{i^2}} \right)^2$$

where x_i is ith x coordinate and $i = 1 \ldots N$ where N is number of points.

Quality of CFLIBS results has been considered in accordance of [100]:

$$dist = \sum_{i=1}^{N} abs \mid M_i - C_i \mid \tag{3.17}$$

as distance of concentration vector $\overrightarrow{M}$ determined by LIBS and vector of nominal concentrations $\overrightarrow{C}$ both in %.

3.6.4 LTE considerations

As it was described in section 1.5, the LTE is very important to be satisfied in LIP during measurement of emission spectra. Usually McWhirter's 1.14 expression is used to asses LTE. The value calculated from the criteria was

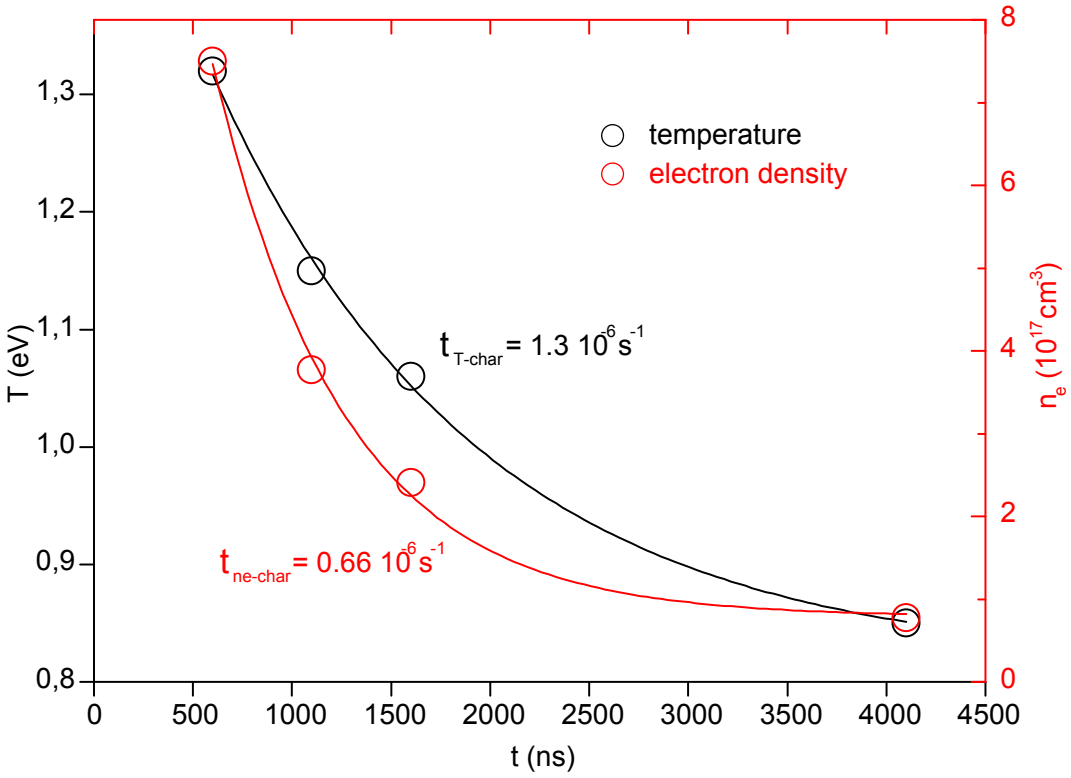

Figure 3.17: The evolution of temperature and electron density number in LIP. The characteristic times are obtained from a fit to exponential function.

estimated to $\approx 10^{15}$ cm^{-3} what is at least 100 times smaller value than measured electron number density and therefore the criteria is fulfilled.

But McWhirter's expression is valid only in case of homogeneous and stationary plasma conditions. Such an approach should be verified and time of processes responsible for re-equilibrium of plasma and diffusion lengths of particles have to be much more lower than characteristic time of plasma temperature evolution and dimensions of LIP respectively. For estimation of the slowest collisional rates, the transitions to ground state from lowest upper energy state have to be selected. For evaluation of such collisional rates, the expression 1.16 has been used. Its results are shown in table 3.4 (Effective Gaun factor $\langle \bar{g} \rangle$ was estimated to be 0.04 from plot in [104]). The change in temperature and electron density number must be slow within the time τ_{rel} as it is expressed by 1.15. To consider the time evolution, the temperature and electron density number of LIP have been determined. For this purpose spectra have been acquired for different delay times from laser pulse. The evolution of temperature and electron density is shown in the figure 3.17. The measured values have been fitted to exponential function to obtain decay con-

stant n_{e-char} and T_{char}. The higher value $1.3{\cdot}10^6$ s is much more higher than any value τ_{rel} from table 3.4 what means that evolution of plasma is slow enough to re-equilibrate via collisions.

		λ (nm)	E_2 (eV)	g_1	g_2	f_{12}	M	τ_{rel} (s)	λ_D (cm)
Mn	I	403.448	3.07	6	4	2.57E-02	55	1.5E-08	1.9E-04
Al	I	394.401	3.14	2	2	1.15E-01	27	3.6E-09	1.3E-04
Cu	I	327.395	3.79	2	2	2.20E-01	63.5	4.3E-09	9.5E-05
Mg	I	285.213	4.35	1	3	1.80E+00	24.3	1.1E-09	7.6E-05
Mg	II	280.271	4.42	2	2	3.03E-01	24.3	6.9E-09	2.0E-04
Mn	II	260.568	4.76	7	5	2.00E-01	55	1.6E-08	2.0E-04
Si	I	251.432	4.93	1	3	2.10E-01	28.1	1.8E-08	3.0E-04

Table 3.4: Spectroscopic data for estimation of relaxation time and diffusion length of different species in LIP.

For estimation of the diffusion length, expressions 1.18 and 1.19 have been used. The results are shown in the table 3.4 in column λ_D. As N_{II} density number of electron in time 1.5 μs was used even it can be very different from real values. But the precision is sufficient which can be seen later in the comparison process. Determined diffusion lengths have been compared with dimensions of plasma to asses LTE. Dimensions of plasma were estimated by spectra measuring in different location transversal to plasma plum. The intensity decrease to 1 % was considered to be plasma border. The plasma plum dimension was estimated to value ≈1 mm. The diffusion lengths presented in table 3.4 are much lower than plasma dimension, hence the plasma can be considered to be in LTE.

The previous results suggest that the plasma is in LTE and this assumption can be used in further analyses.

3.6.5 Results and discussion

The measurement of spectra have been performed in two different positions 1 mm and 2 mm above the sample surface. The intensities of emission lines differ in these two positions. Additionally, different line profiles have been observed for some transitions. In figure 3.18 such a behaviour is presented for part of spectra. The change in profile shape for two spectra is obvious for Mg I 285.213, Mg II 279.553 and Mg II 280.271 nm lines. All mentioned lines relate to transition to ground state (resonance lines). Such lines are very tent to be self absorbed (see section sec:plasmaAbsorption). The temperature

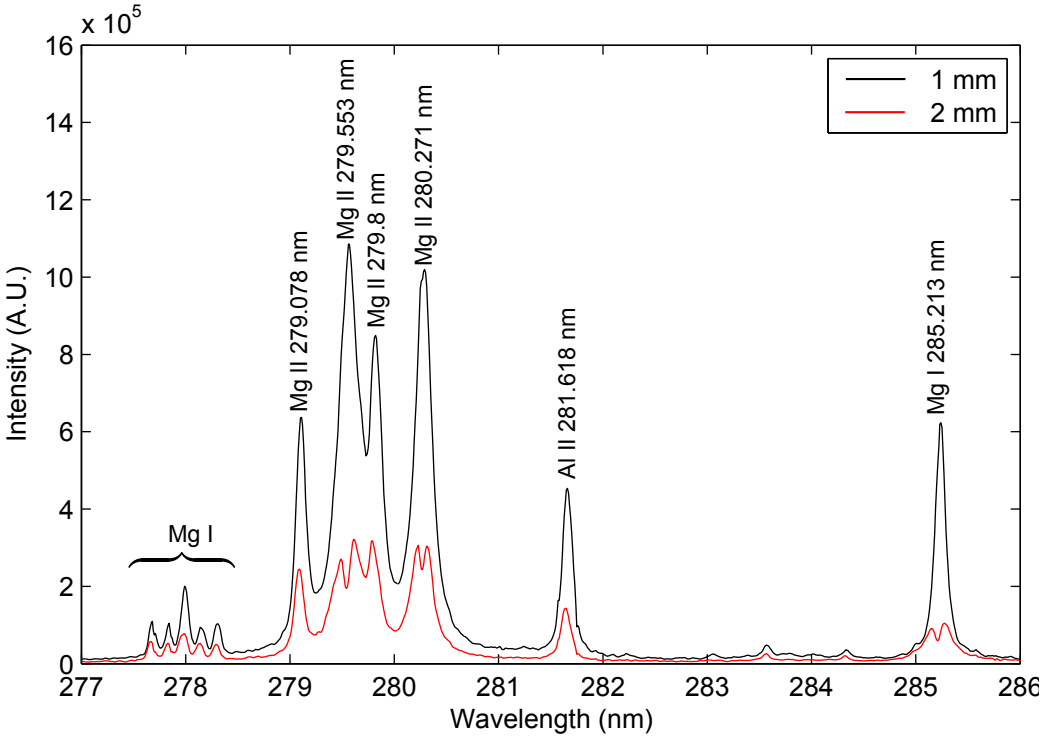

Figure 3.18: Two spectra acquired from positions of 1 and 2 mm above the sample surface with same experimental conditions.

is lower in the upper part of plasma and there is probably a thick layer of cold outer plasma which causes self-absorption so strong that lines become self-reversal.

All lines whose lower transition level is ground or is very close to ground have been rejected from SB plot construction. In table 3.2 those lines have been rejected whose $E_1 < 0.02$ eV. The SB plots for all samples in two positions are presented in figure 3.19, 3.20 and 3.21. Even if resonance transitions have not been included in SB, their intensities are presented in the plots as solid circle. Their intensities are evidently decreased and all are located under the line.

Temperature of LIP for Mg, Al, Mn have been determined from slope of SB plot with related errors. The slopes are similar and in accordance of LTE assumption. As it can be seen, the plasma located in 1 mm distance from the surface is hotter than the one in 2 mm distance. The error caused by fluctuation of line intensities is negligible. If obtained temperatures are not good, the source of error has to be different. Intensities represented by points in SB plot are not perfectly located on the line. This can be caused by interaction of used lines with some other lines which was not identified, by error coming

from Einstein coefficient, by not perfect LTE, or by some physical process (self-absorption).

Atoms and single ionized ions have been included in concentration calculation. Double ionized ions have been excluded from calculation and their contribution to results have been considered as negligible. In left figure 3.16 doubly ionized ions abundance dependent on temperature is presented for every analysed elements. The magnesium is the most critical and for maximum experiment temperature 1.1 eV, relative abundance ≈1.7 % is reached. Such an abundance was considered in further CF-LIBS calculations as negligible.

1 mm									
	S1	S2	S3	S4	S5	S6	S7	S8	S9
Mg	0.52	0.84	2.18	0.3	1.8	1.95	0.54	2.63	2.08
Al	98.53	98.5	97.54	99.49	97.99	97.8	98.33	97.25	97.71
Cu	0.64	0.53	0.01	0	0.01	0.01	0.61	0.01	0.01
Mn	0.16	0.11	0.14	0.02	0.07	0.07	0.21	0.05	0.05
Si	0.15	0.02	0.13	0.19	0.13	0.16	0.31	0.06	0.15
distance	4.92	5.61	4.86	1.27	3.32	3.79	3.56	5.21	2.08
2 mm									
	S1	S2	S3	S4	S5	S6	S7	S8	S9
Mg	0.82	1.36	2.88	0.45	2.43	2.4	0.83	3.11	2.71
Al	97.52	97.58	96.73	99.15	97.32	97.29	97.55	96.71	97
Cu	1.04	0.81	0.01	0.01	0.01	0.01	0.9	0.01	0.01
Mn	0.31	0.17	0.22	0.02	0.11	0.11	0.3	0.12	0.08
Si	0.32	0.08	0.17	0.38	0.13	0.18	0.41	0.05	0.2
distance	2.98	3.77	3.23	0.58	1.98	2.77	2.43	4.14	0.68

Table 3.5: Composition of aluminium alloy samples in % determined by CFLIBS method for two different locations in LIP 1 mm and 2 mm above the samples surface.

Table 3.5 and figures 3.22 and 3.23 contains composition of the samples determined for 1 mm and 2 mm location distance from sample surface in LIP. Distances from nominal concentrations are also presented calculated by 3.17. The results are closer to the nominal composition for 2 mm measurement. They are spread in range 0.58–4.14 %. In [100] some results from [97, 61, 101] are presented, shown in table 3.6. The distances are in a range 0.9–5.4 with values slightly worse than are presented in above results. The errors bars presented in figures originate from intensity variation of spectral lines and are mostly lower than deviations of resulted from nominal compositions. This should be cause by some other source of error, probably originate in not conserved stoichiometry of the sample in the plasma in the observed location. Probably,

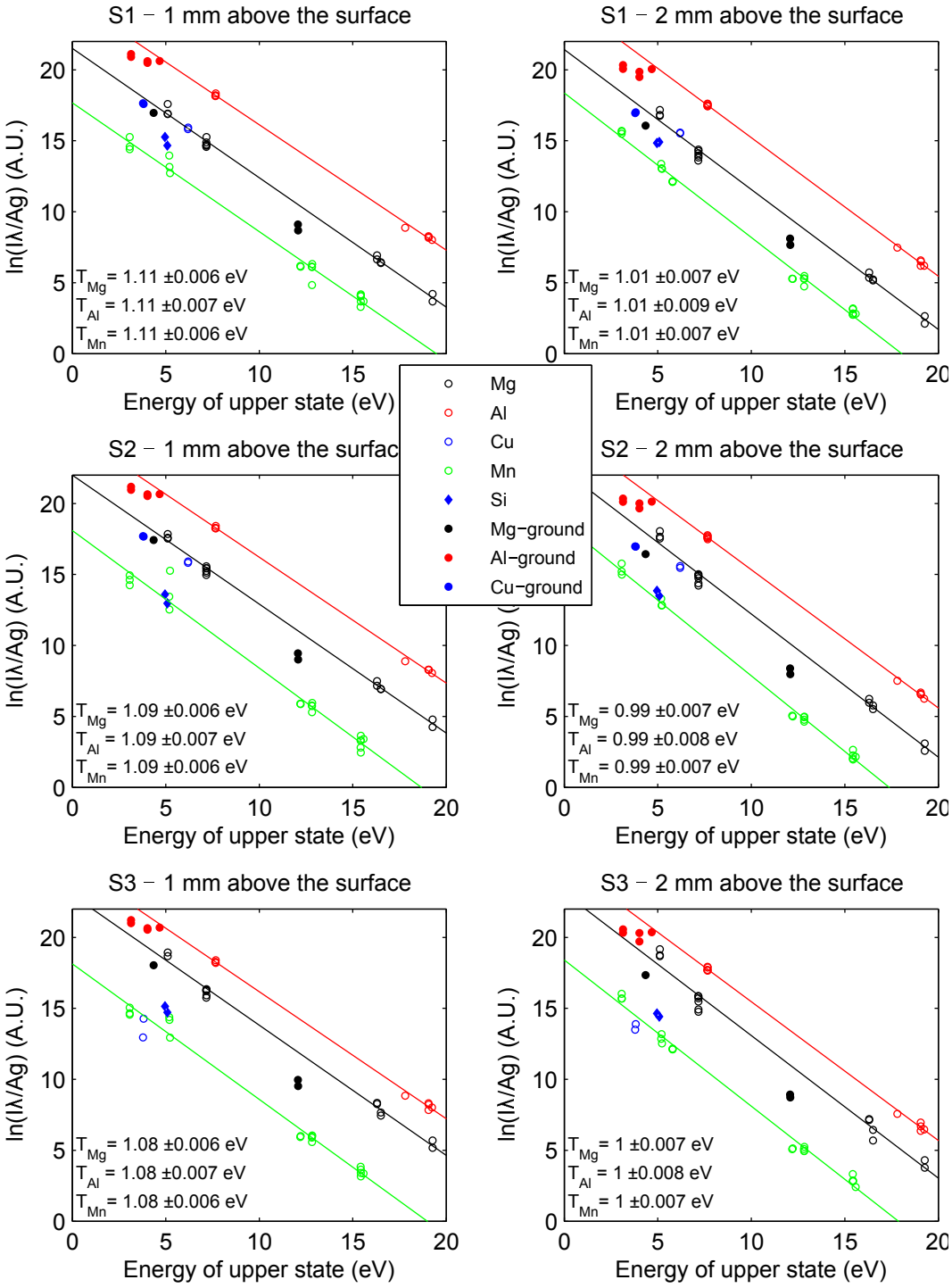

Figure 3.19: Saha-Boltzmann plots for S1–S3 aluminium alloy samples. The plots for two different distances (1 mm and 2 mm) from the surface are presented for every sample. The intensities from transitions to ground levels are not included in fitting process for Mg, Al and Cu, but they are presented in the figures as solid circles.

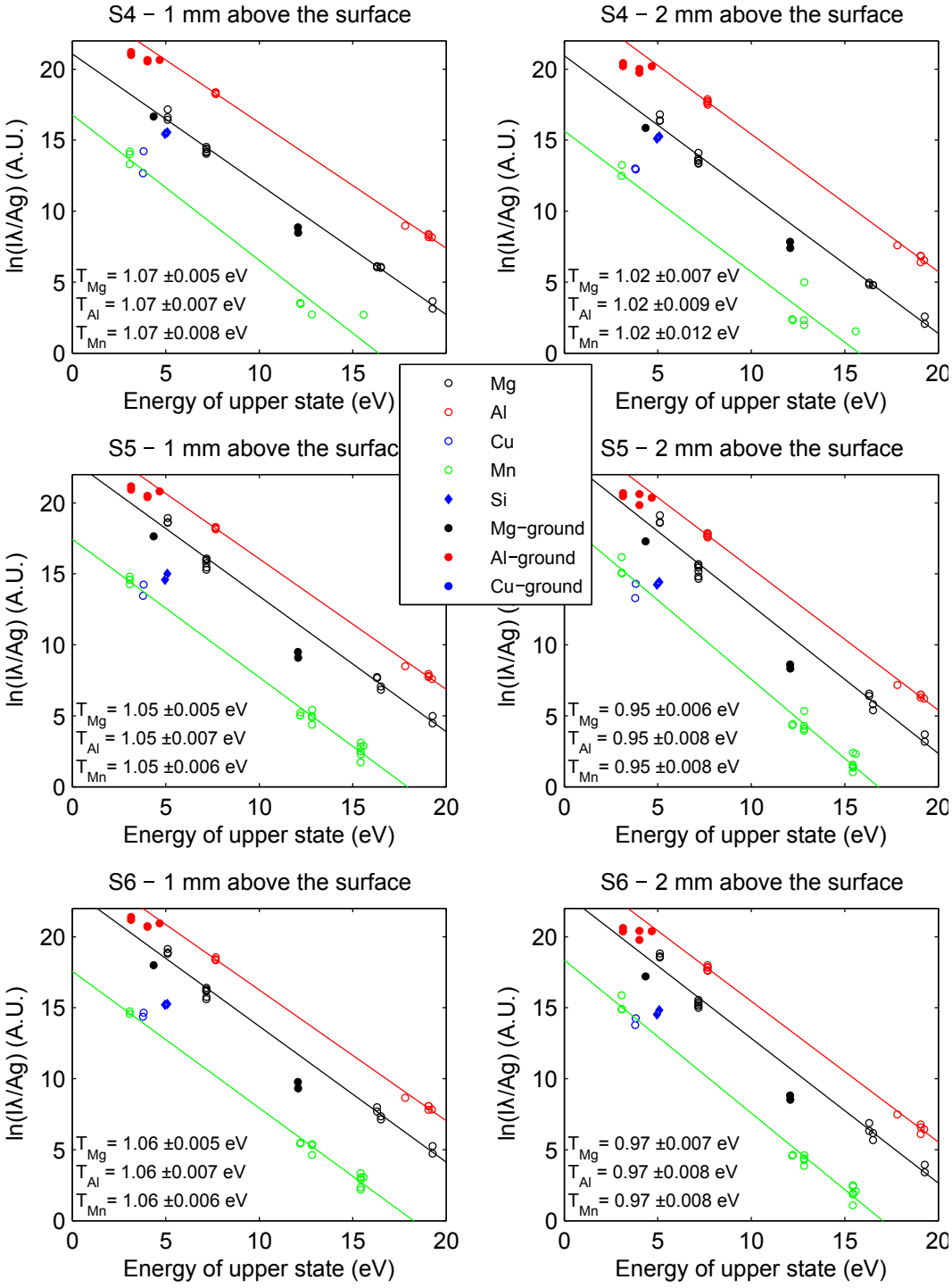

Figure 3.20: Saha-Boltzmann plots for S4–S6 aluminium alloy samples. The plots for two different distances (1 mm and 2 mm) from the surface are presented for every sample. The intensities from transitions to ground levels are not included in fitting process for Mg, Al and Cu, but they are presented in the figures as solid circles.

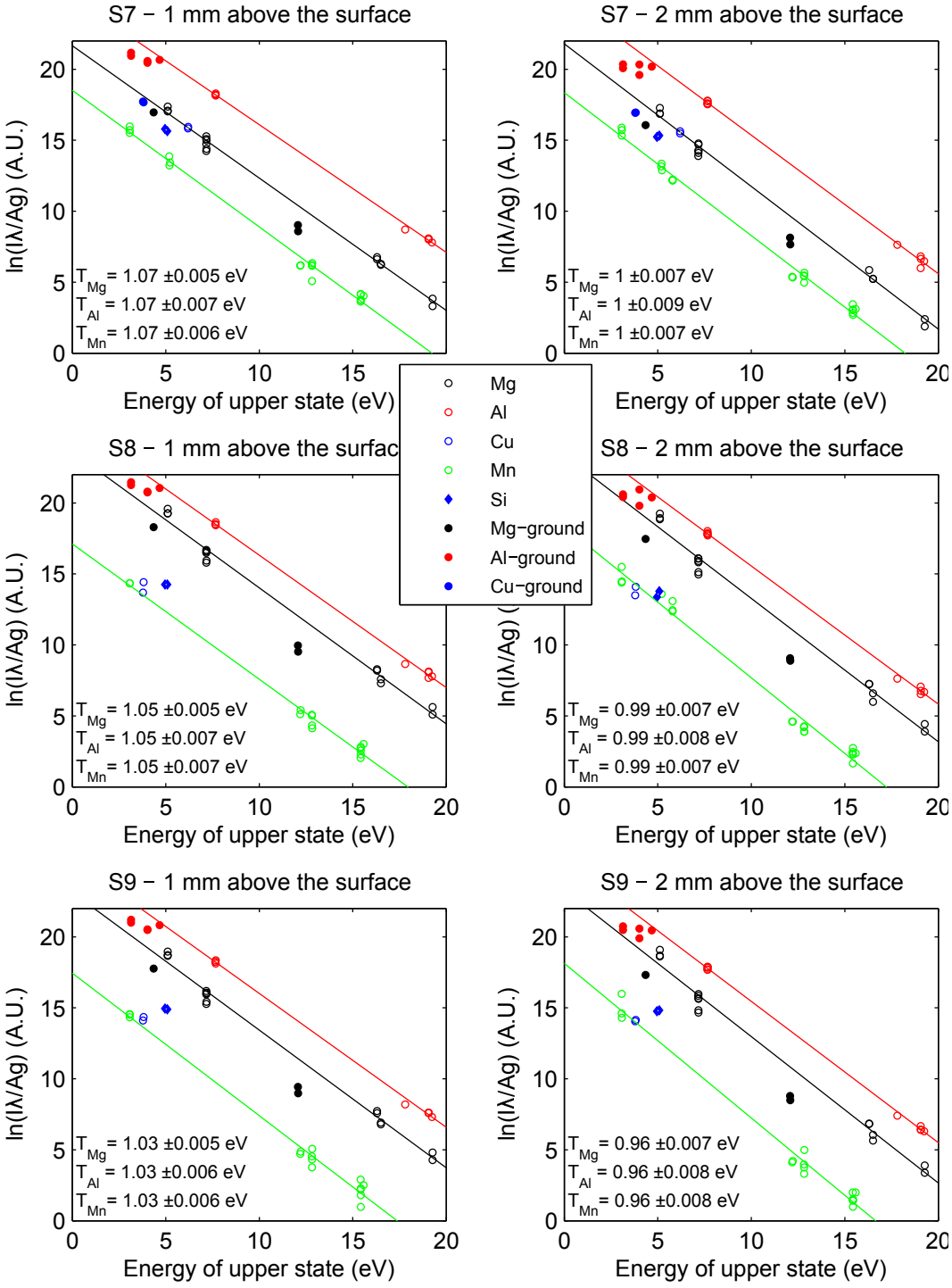

Figure 3.21: Saha-Boltzmann plots for S7–S9 aluminium alloy samples. The plots for two different distances (1 mm and 2 mm) from the surface are presented for every sample. The intensities from transitions to ground levels are not included in fitting process for Mg, Al and Cu, but they are presented in the figures as solid circles.

error can be eliminate by finding better location in the plasma in which the stoichiometry can be conserved. Even if such a location exists it will probably change with sample type. To consider CF-LIBS as universal analytical method the further research is needed.

samples number	element number	distance	reference
1	7	0.9	[23]
1	5	1.8	[101]
1	3	5.4	[61]
1	3	2.8	[97]

Table 3.6: Published results for aluminium alloys measured by CFLIBS.

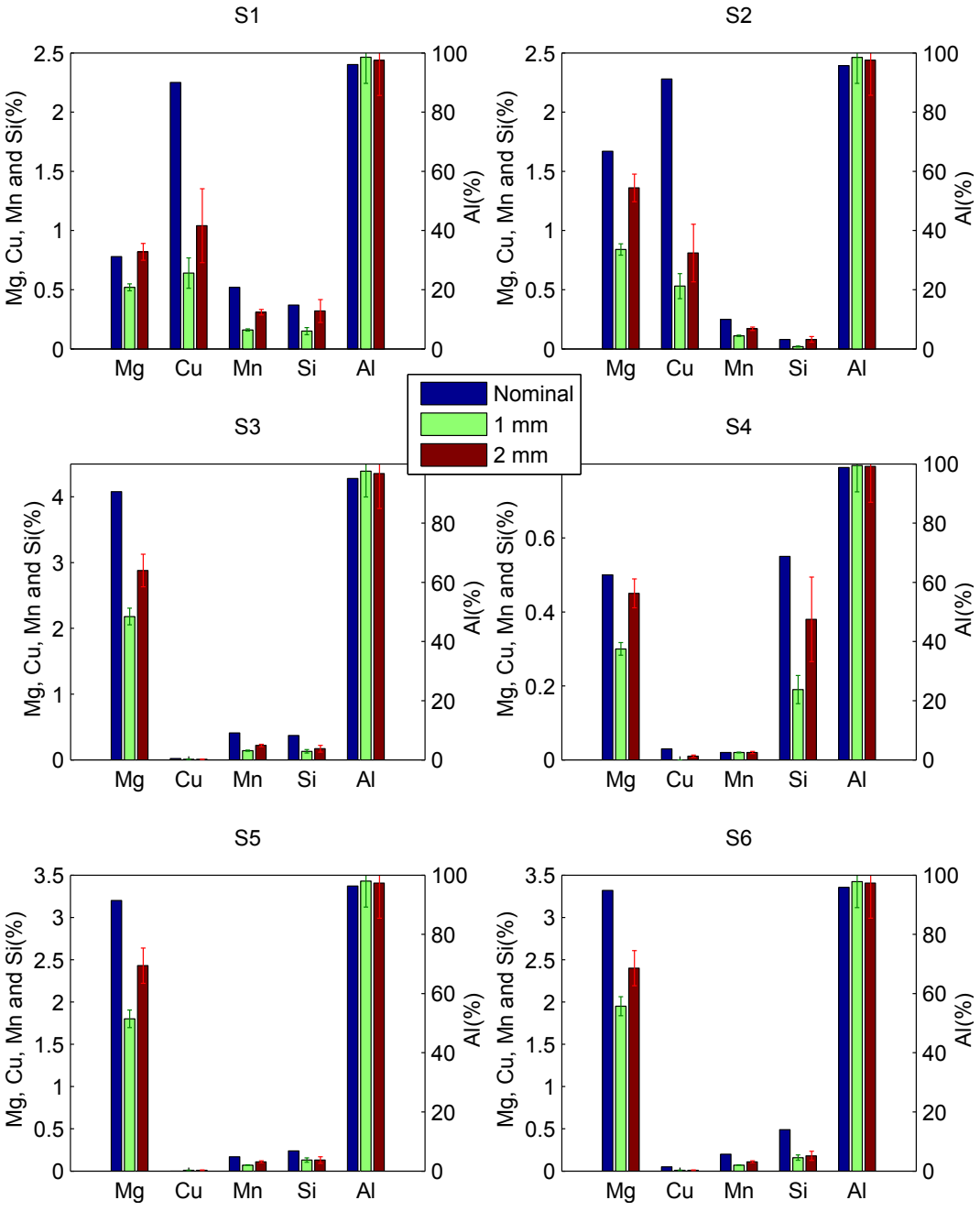

Figure 3.22: S1–S6 aluminium alloy sample compositions. The composition has been determined by CF-LIBS collecting light from two different distances above the surface (1 mm and 2 mm). Black bars show the nominal composition.

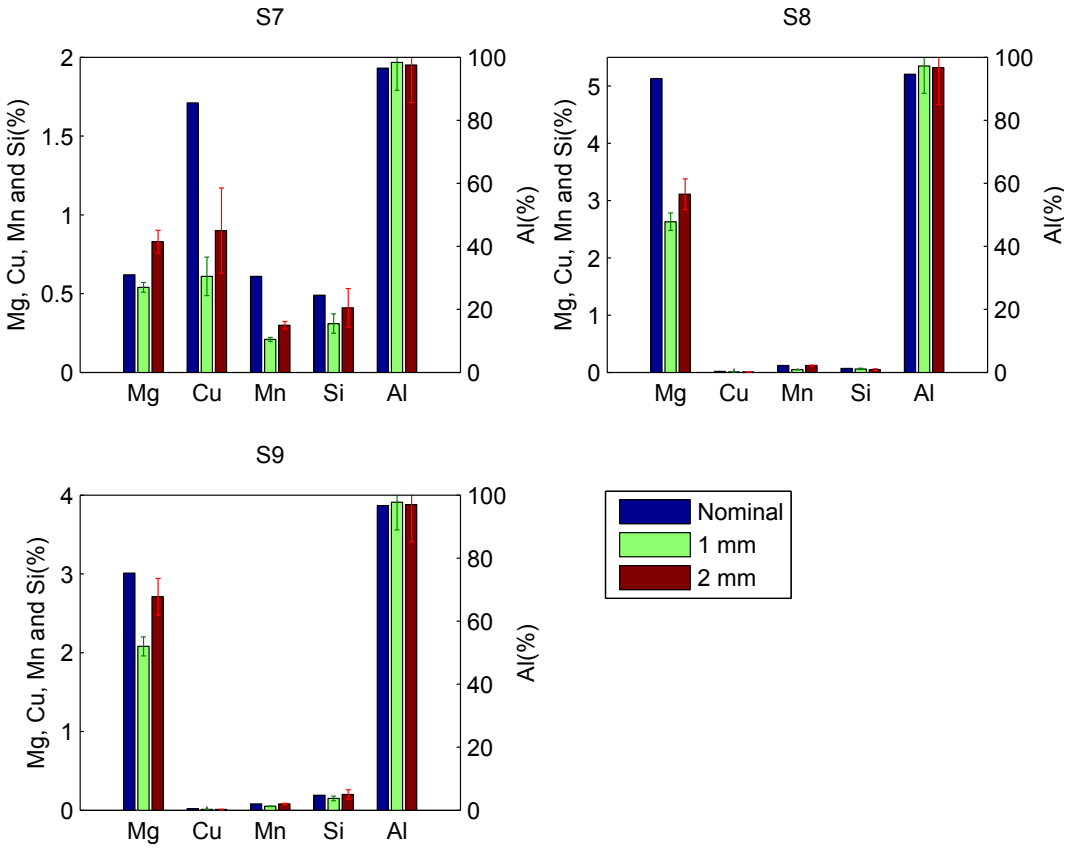

Figure 3.23: S7–S9 aluminium alloys sample compositions. The composition has been determined by CF-LIBS collecting light from two different distances above the surface (1 mm and 2 mm). Black bars show the nominal composition.

Chapter 4

Self-absorption

4.1 Introduction

In the last stage of my thesis the research of self-absorption in LIP has been started. In section 3.6 the emission lines coming from resonance transition have been excluded from temperature and composition determination of aluminium alloys. The rejected lines have been strongly influenced by self-absorption and their intensities were therefore decreased. As it can be seen in the figure 3.19, 3.20 and 3.21 all resonance lines marked by the solid markers are under the line presenting the SB plot, what means that their intensities are lower than they should be. If the self-absorption is too strong, line profile becomes self-reversed as it is presented in the figure 4.1. In the left figure resonance line is presented for four different locations in the LIP. As location is increasing, the line becomes broadener and finally self-reversed for the largest distance from the sample surface. In case of no resonance lines, with lower energy level value 2.7 eV (right figure), self-absorptions is probably negligible.

As it can be seen, self-absorption is considered as negative phenomena in LIBS analyses. The simplest way how to avoid self-absorption in LIBS is exclude lines suspected to be self-absorbed from analyses. Fast method for checking of self-absorption of the line is the determination of the parameter $SA = (\Delta\lambda/2w_s n_e)^{-1.582}$ where $\Delta\lambda$ is experimental line's Stark width, w_s FWHM of Stark broadening parameter and n_e is electron number density [93, 30]. If SA is near 1, it indicates no self-absorption, but $SA \ll 1$ indicates that line is self-absorbed. For determination of the SA parameter one needs to know w_s coefficients.

Other possibility how to consider self-absorption is usage of the "duplicate factor" approach which was used in some plasma works and which is described

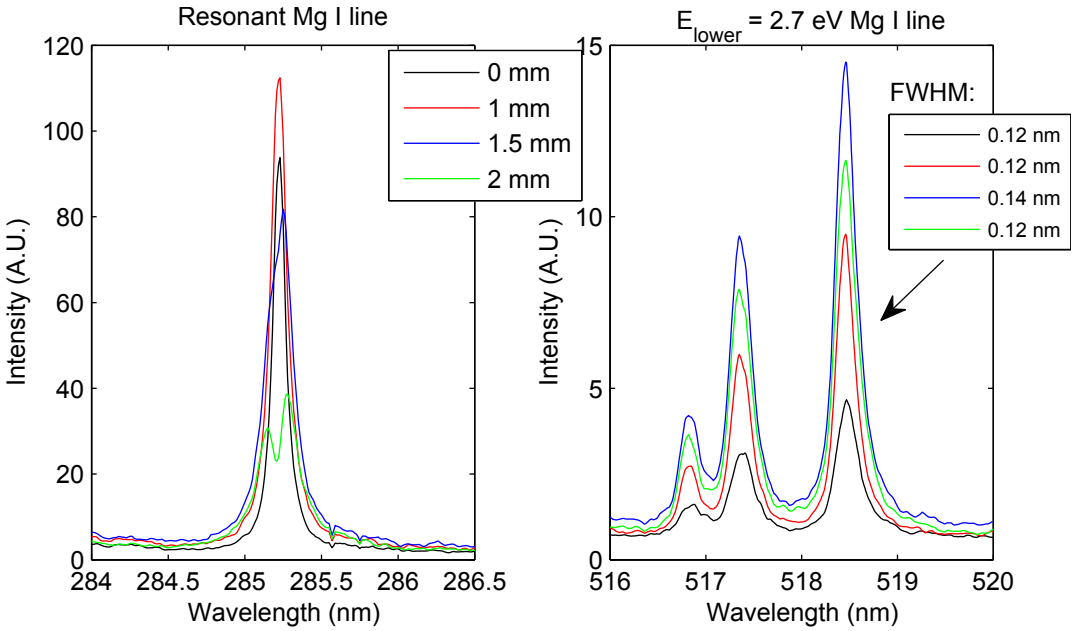

Figure 4.1: Comparison of resonance line profiles and lines of transitions to 2.7 eV as lower state for Mg I. In both cases LIP was observed in four different locations 0, 1, 1.5 and 2 mm above the sample surface in which abundance of Mg in the sample was 1.76 %. Notice FWHM of fitted Voigt profile for non resonance Mg I 518.36 nm line.

in [54, 41, 99]. The concave mirror is used for reflecting of the light coming from plasma back to the plasma (see figure 4.2). The light passes plasma and sum of two different light sources is detected. By measuring with and without mirror, one can obtain two signals. Signals are different and self-absorption can be estimated by their comparison. The method was successfully used in LIBS and presented in [73]. Additionally, the method has been used for profile and intensity correction of self-absorbed lines which have been included into analyses. The correction of lines suffered by self-absorption are also presented in some papers by using of other methods [84, 97, 21, 7, 19].

In following sections the simple model will be presented and fitted to experimental data. The effect of self-absorption will be used as positive phenomena and possibility of density determination of magnesium in the aluminium alloy samples will be sketched out. For this purpose two resonance lines of Mg I and Mg II with they profiles will be used.

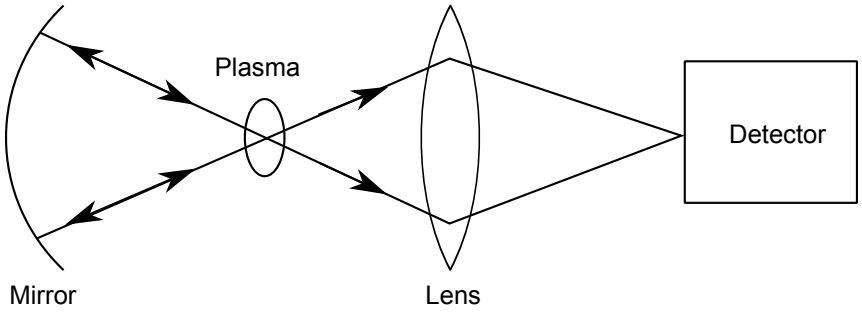

Figure 4.2: Geometry of apparatus for self-absorption determination by concave mirror.

4.2 Emission and absorption of plasma

In the following the radiance I is considered to be isotropic per unit wavelength interval with the unit $\mathrm{Wm^{-2}nm^{-1}sr^{-1}}$. All related expressions as Einstein coefficients or Planck radiation low will be used in such a context. As source for the following derivations the books [41, 99] have been used.

When the light with radiance $I(x, \lambda)$ passes an absorption medium with infinitesimal thickness dx and with absorption coefficient $\kappa(\lambda)$, its radiance will be decreased and in $x + dx$ it can be expressed as:

$$I\left(x + dx, \lambda\right) = I\left(x, \lambda\right) - \kappa\left(\lambda\right) I\left(x, \lambda\right) dx \tag{4.1}$$

In case of the homogeneous media when κ is constant with respect to location, the solution of the equation eventuates to Beer-Lambert law:

$$I\left(\lambda\right) = I_0\left(\lambda\right) e^{-\kappa(\lambda) l} \tag{4.2}$$

where l is the length of absorbed medium and $I_0(\lambda)$ is radiance before it enters to the medium .

Because absorption is in microscopic level related to transitions from lower energetic levels of atoms to higher levels, the decrease in radiance can be expressed as

$$dI\left(x, \lambda\right) = -\left(n_1 B_{12} - n_2 B_{21}\right) I\left(x, \lambda\right) \frac{hc}{4\pi\lambda} P\left(\lambda\right) dx \tag{4.3}$$

where B_{12}, B_{21} are Einstein coefficients for absorption and stimulated emission respectively, n_1 and n_2 are density numbers of lower and upper energetic levels respectively ready to absorb or emit photons and $P(\lambda)$ is absorption line profile normalized to 1. Notice that stimulated emission is included even

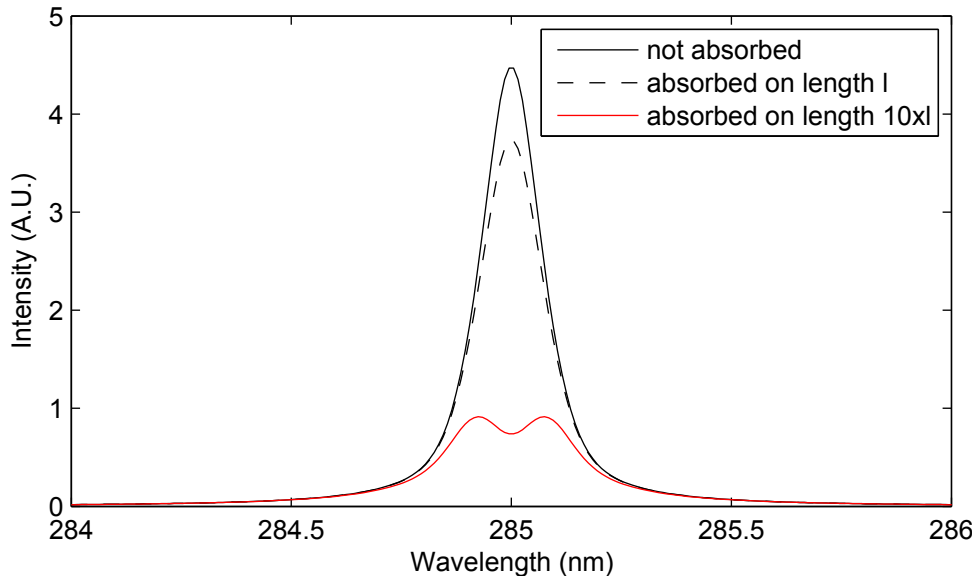

Figure 4.3: Not absorbed and absorbed on l and $10 \times l$ length emission profiles in the absorption medium.

it produces reverse process to absorption, sometimes referenced as negative absorption. Decrease of the radiance can be also expressed from equation 4.1 as:

$$dI\left(x,\lambda\right) = -\kappa\left(\lambda\right) I\left(x,\lambda\right) dx \tag{4.4}$$

From two equations 4.4 and 4.3 by eliminating of I and dx the $\kappa(\lambda)$ can be expressed as:

$$\kappa\left(\lambda\right) = \left(n_1 B_{12} - n_2 B_{21}\right) \frac{hc}{4\pi\lambda} P\left(\lambda\right) \tag{4.5}$$

The example of calculated profiles by using equation 4.2 is shown in figure 4.3. The absorption coefficient is assumed to have the same shape as line emission profile which is presented as not absorbed one in the figure. Whereas intensity of the line absorbed on the length l is slightly decreased, the intensity of the line absorbed on the length 10 times longer is strongly decreased and the shape becomes self-reversed.

If plasma will be considered as medium, the emission has to be included to expression 4.1. This can be done by adding emission term ϵdx:

$$I\left(x+dx,\lambda\right) = I\left(x,\lambda\right) - \kappa\left(\lambda\right) I\left(x,\lambda\right) dx + \epsilon\left(\lambda\right) dx \tag{4.6}$$

where $\epsilon(\lambda)$ is emission coefficient. The emission coefficient can be expressed by Einstein coefficient for spontaneous emission A_{21} as:

$$\epsilon(\lambda) = n_2 A_{21} \frac{hc}{4\pi\lambda} P(\lambda) \tag{4.7}$$

where n_2 is density of upper energetic state of atom emitting photon by transition from this state to lower state. The $P(\lambda)$ is profile of the emission line normalized to 1. The same profile is used in both absorption and emission coefficients.

For case of the homogeneous plasma, equation 4.6 can be solved and expressed as:

$$I(\lambda) = I_0(\lambda) e^{-\kappa(\lambda)l} + \frac{\epsilon(\lambda)}{\kappa(\lambda)} \left(1 - e^{-\kappa(\lambda)l}\right) \tag{4.8}$$

The expression consists of two parts. The first one indicates absorption of the external radiance entering the plasma with intensity I_0 and the second one presents the mix of emission and absorption of the plasma itself. The term $\epsilon(\lambda)/\kappa(\lambda)$ can be rewritten by equation 4.5 and 4.7 to:

$$\frac{\epsilon(\lambda)}{\kappa(\lambda)} = \frac{n_2 A_{21}}{n_1 B_{12} - n_2 B_{21}} \tag{4.9}$$

and further by using of relation between Einstein coefficients [99]:

$$\begin{aligned} g_1 B_{12} &= g_2 B_{21} \\ A_{21} &= \frac{2hc^2}{\lambda^5} B_{21} \end{aligned} \tag{4.10}$$

where g_1 and g_2 are lower and upper state degeneracy respectively and by using of Boltzmann expression 3.2 to well known Planck formula 3.15. So expression 4.8 can be rewritten to form:

$$I(\lambda) = I_0(\lambda) e^{-\kappa(\lambda)l} + B(\lambda, T) \left(1 - e^{-\kappa(\lambda)l}\right) \tag{4.11}$$

Figure 4.4 shows the radiance of Mg I 285.213 nm line from plasma, calculated by using of expression 4.11. In the left figure the line profiles are shown for three different Mg I element densities in the plasma. As the density is rising the self-absorption is more evident. In the case when density is 10^{18} cm^{-3}, the top part of the profile starts to be flat and tends to radiation of black body. In the calculation the external source of radiation I_0 was set to be 0. For the case shown in the right figure, the I_0 was set to the values obtained by calculation from the left figure for the case $n_e = 10^{17}$. The temperatures have been set to values 1 and 0.6 eV and the length of plasma to 1 mm as previously.

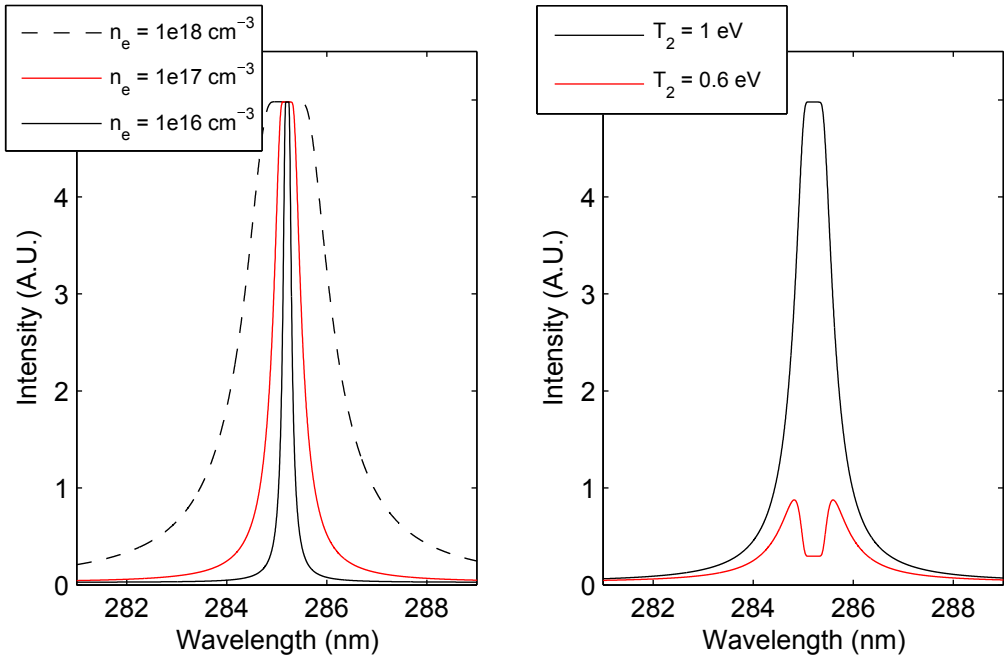

Figure 4.4: Left figure: Radiance of Mg I 285.213 nm line from 1 mm thick homogeneous plasma in LTE. The line profile for three different Mg I densities with temperature of the plasma 1 eV is presented. In the case of n_e =1e18 cm^{-3} upper part of the profile is part of black body radiation curve. Right figure: Profile if two plasma layers are considered with the same temperature of 1 eV for first layer and with different temperatures $T_2 = 1$ eV and 0.6 eV for second layer.

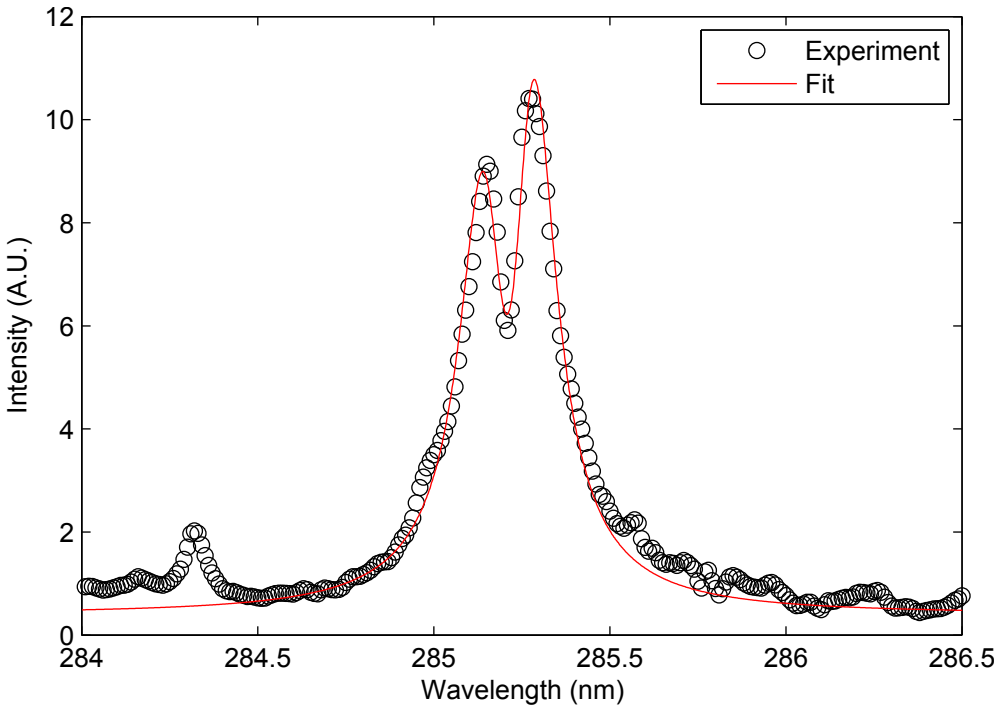

Figure 4.5: Example of simulation fit to measured line profile for Mg I 285.231 nm line.

Whereas for the temperature 1 eV, profile is broadened and flatted on its top, for the temperature value 0.6 eV profile is self-reversed. Such a behavior can be explained by higher densities of the lower energetic states in the plasma as a consequence of lower temperature. These states are ready to absorb photons emitted by the reverse transitions. Additionally, probability of absorption is proportional to values derived from the line shape. So absorption maximum is in the maximum of the line shape.

4.3 Experimental

In the following experiment, the simple model has been used to simulate line profiles to obtain density numbers. The expression 4.11 and related expressions have been used in the model. The calculated profiles have been fitted to the experimentally measured data as it can be seen in example figure 4.5.

The expression 4.11 can be rewritten to the recursive form for the case of many layer plasma:

$$I_i(\lambda) = I_{i-1}(\lambda)\, e^{-\kappa_i(\lambda) l_i} + B(\lambda, T_i)\left(1 - e^{-\kappa_i(\lambda) l_i}\right) \tag{4.12}$$

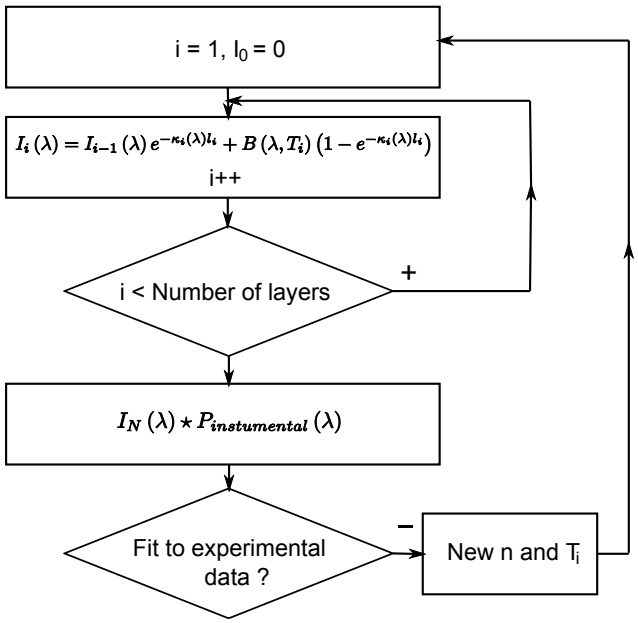

Figure 4.6: Block diagram for the calculation and fit of profile for lines radiated from many layer plasma.

where index i indicates the layer for which the radiance is calculated. The index equal to 1 indicates first layer of the plasma for which $I_0 = 0$. As it comes out form previous section, the every plasma layer is homogeneous, stationary and in LTE defined by temperature T_i, with the thickness l_i. The above expression have been used in developed program in order to fit calculations to measured profiles. The block diagram of the program is depicted in the figure 4.6. The program in iterative process fit calculated to experimental data, by varying temperatures and density numbers for the individual plasma layers. Before the fit sequence and after the profile calculation, line shape is corrected by convolution with the instrument function. Such a procedure is necessary for the instrument function broadening, which is much higher than the broadening caused by physical processes in the plasma.

Two layer plasma have been considered for a start with the presented model. With connection to real LIP, the first layer was considered as inner and hotter part of LIP and the second layer as outer, colder part of LIP. Temperature of the inner part has been set in the program and it was not fitted. Its value has been determined from the SB plot. The temperature of the outer layer was determined in the fitting process for first sample and used as constant for other samples. The plasma parameters were assumed to be same within all samples. The density number was supposed to be equal in the

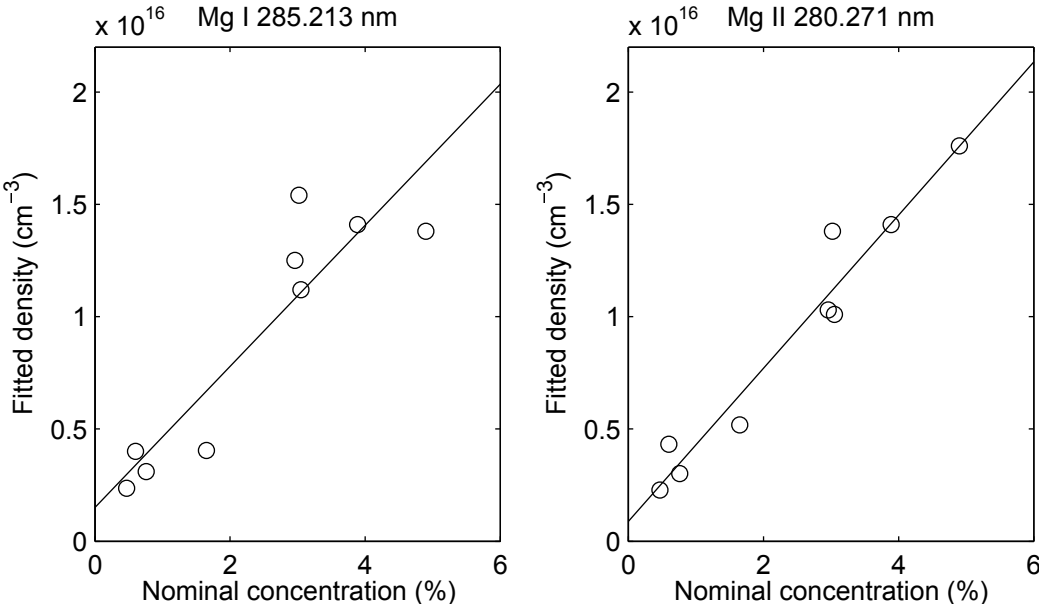

Figure 4.7: The evolution of fitted density of plasma vs. nominal composition of the samples, determined for Mg I 285.213 nm and Mg II 280.271 nm lines. Results are obtained from average of 50 measurements.

both layers, therefore it was fitted as one parameter.

The samples and apparatus were the same as they have been used for aluminium alloy analyses, presented in the section 3.6. The data from measurement in the location 2 mm above the sample have been used. As it can be seen in the figure 3.18 and 4.1, big difference in line profile can be observed for 1 mm and 2 mm measurement above the sample for resonance transition. The location of 2 mm is supposed to be better for presented method, mainly because of spectrometer's resolution. All measured spectra have been acquired with exposition time of 200 ns and delay after laser pulse 1.5μs.

The Mg I 285.213 nm and Mg II 280.271 nm profiles have been simulated with aim to fit them to the experimentally measured profiles. The density numbers of Mg I or Mg II can be obtain by finding its optimum. Determined density numbers have been compared with the nominal compositions, which are presented in the table 3.1.

4.4 Results and discussion

The values of the fitted densities of Mg I and Mg II have been compared with nominal composition for different magnesium concentrations in the aluminium alloys. The results are shown in figure 4.7. Two different spectral lines have

been used for calculation fits to experimental profiles. Whereas neutral line has been fitted in wide range of 283–287 nm, the ionic line has been fitted in smaller range of 280.17–280.37 nm. The ionic line interacts with other magnesium lines, so only top of the line has been fitted.

The plotted line in the figure indicates the result after the linear regression of the presented points. The points indicate calculated value of density fitted to the experimental line profile related to concentration of some sample. The evolution of points for neutral line Mg 285.213 shown, in the right figure, is not very linear and it contains lot of out-layers. For working model one should expect the linear dependency. As it can be seen, the difference between 3, 4 and 5 % in composition is not reliably resolvable. In the case of results for which the ionic line has been used (see right figure 4.7), the dispersion of the point around the line is not so high and out-layer are not so evident. Also difference in the composition of sample is more evident, nevertheless the smaller fitting range has been used. The small fitting range has been tested also in case of the neutral lines but without considerable improvement in the linearity.

The presented results have been obtained by fit to experimental data averaged from 50 measurements. Other results, that have been obtained from data averaged from 10 measurements for 5 series are presented in figure 4.8 for ionic line. The good reproducibility can be seen except of series 3. But even linear regression for series 3 has R closer to 1 than in case of neutral line presented in left figure 4.7). The abundance around 10 % for neutral and 90 % for ions for magnesium can be deducted from figure 3.16 for temperature 1eV. The 10 times lower density produces higher uncertainties. Also variation of the temperature influences the relative change of the neutral's density more than the ion's one. These are probably reasons for difference in quality of density determinations from neutral and ionic lines.

The presented method for determination of densities in the plasma by using of self-absorption is potentially working when ion line Mg II 280.271 nm is used. In the case when neutral line Mg I 285.213 is used, it is not possible to make linear relations between composition in the sample and the density determined from plasma. The measurement and calculations are aimed to be preliminary for further research. As it was shown, the profile of lines radiated from plasma contains information about the plasma composition. For further research we plan to use higher resolution of spectrometer $\approx$0.015 nm to decrease negative influence of instrumental function and to get line profile with higher quality.

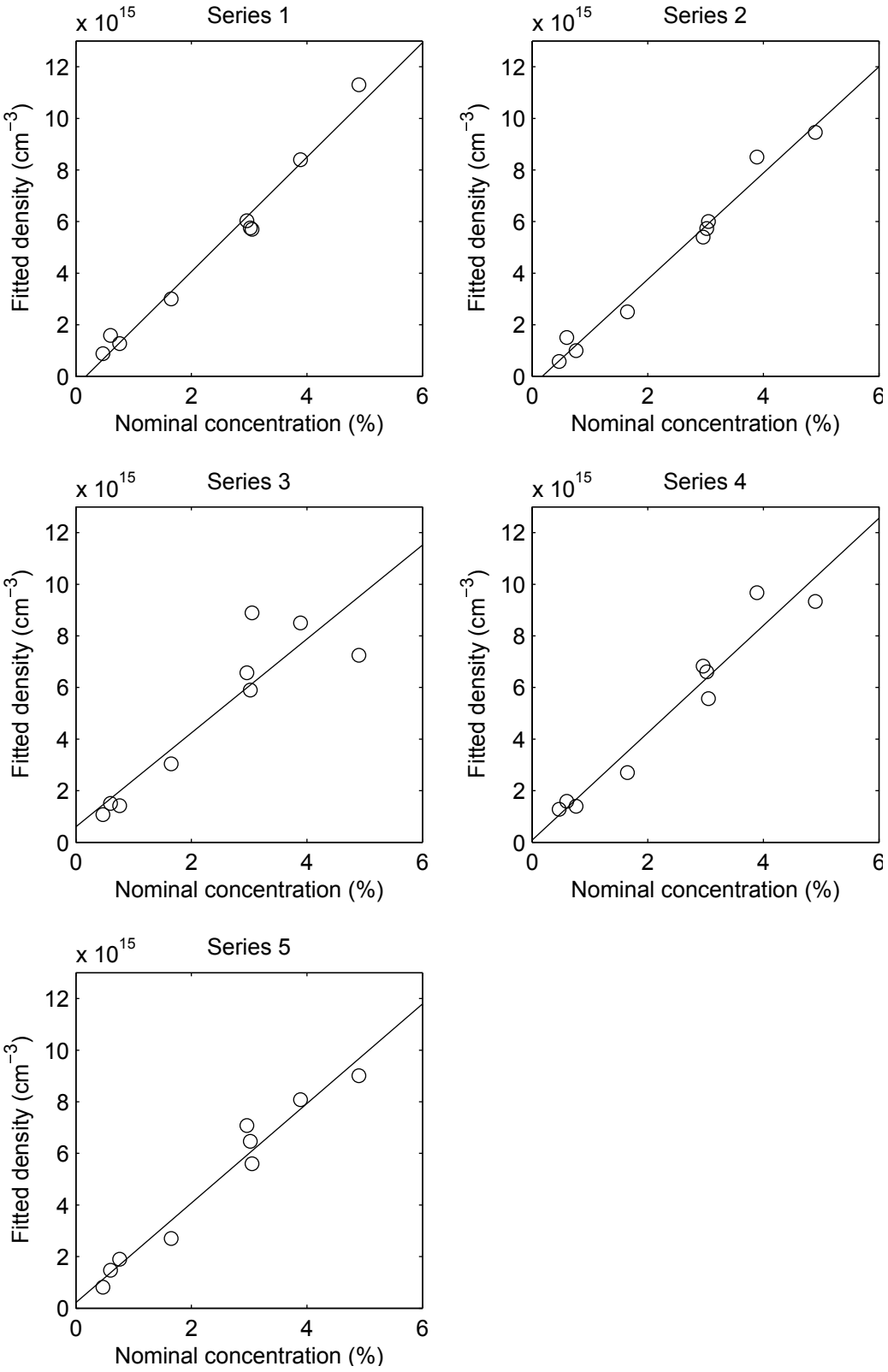

Figure 4.8: The evolution of fitted density of plasma vs. nominal composition of the samples, determined for Mg II 280.271 nm lines for five different measurement series. Results in every series are obtained from 10 measurements.

Spatial deconvolution is planned for more precise temperature and plasma layer thickness determination. Consequently their values can be used in many instead of two layer plasma model.

Conclusions and perspectives

The presented work deals with application of the LIBS techniques in both portable and laboratory conditions. The research in the laboratory is usually only part of process before full implementation to real application. The LIBS technique is potential candidate to be used in small and light portable form, however the full implementation of the idea is not finished yet. One part of this work presents developed portable device with appropriate software support. The device is really portable with respect to its weight and with respect to its independence from external power supply. The weight of 5 kg and 6 hours of working time allow someone to use the device out of laboratory for on-site measurements. The developed software offers real time corrections of unwanted behavior of implemented compact spectrometer and fast preliminary spectra processing.

The described experiment illustrates the potentialities of the developed portable LIBS instrument in Earth sciences, more particularly in geochemically recognizing (i) tephra layers in lacustrine sediments and (ii) fossilization processes in ammonites. Abundances for selected lines of Al, Ca, Fe, Ti, Ba and Na were determined in lacustrine chalk sediments of the Jura, where the Laacher See Tephra (LST) layer was recorded. The thickness of the ash layer appears different when assessed with Na and Ti (5 mm) and Al, Ca and Ba (10 mm). A second layer, previously considered to be of organic origin was associated to volcanic origin however verification of such a conclusion is needed.

Our portable LIBS system can already be considered as a useful and practical on-site tool for geology. Semi-quantitative or quantitative measurements, long sought after by geoscientists, could be the next improvement to our portable LIBS.

In the part related to laboratory LIBS, the possibilities of CF-LIBS and self-absorption phenomena was studied. The spectral response of optical system was determined in order to obtain spectra not influenced by spectral response of the optical system. The compositions of various aluminium alloys

were determined by using of calibration free technique for two different locations in the plasma. More accurate results have been obtained from upper part of plasma located 2 mm above the sample surface then from 1 mm location. The resonance lines of Mg and Al elements are self-absorbed so much in this part of plasma that they become self-reversed. Self-absorption phenomena was studied for same samples in order to check possibility to use the phenomena for composition determination. Result suggests that self-reversed profile potentially contains information about the density of the related element in the plasma. In further research we plan to increase the resolution of spectrometer for the better line profile measurement. Additionally we plan to use many layer plasma model with exact temperature and layer thickness values obtained from spatial deconvolution of the transversally measured plasma plum.

Abbreviations

EDS	Energy-Dispersive X-Ray Spectroscopy
EDX	Energy-Dispersive X-Ray Spectroscopy
EPR	Electron Paramagnetic Resonance
FUS-ICP	Fusion Inductively Coupled Plasma
FWHM	Full Width at Half Maximum
ICCD	Intensified Charge Couple Device
ICP	Inductively Couplet Plasma
LIB	Laser Induced Breakdown
LIBS	Laser Induced Breakdown Spectroscopy
LIP	Laser Induced Plasma
LIPS	Laser Induced Plasma Spectroscopy
LSC	Laser Support Combustion
LSD	Laser Support Detonation
LST	Laache See Tephra
LTE	Local Thermodynamics Equilibrium
MPI	Multiphoton Ionization
MS	Mass Spectroscopy
NMR	Nuclear Magnetic Resonance
OES	Optical Emission Spectroscopy
PC	Pockel Cell
PCB	Printed Circuit Board
pLTE	partly in Local Thermodynamic Equilibrium
SB	Saha-Boltzmann
SEM	Scanning Electron Microscope
UMT	Ulmener Maar Tephra
XRF	X-Ray Fluorescence

Appendix A

Manual for XYZ transition program

Main application window and its parts see fig.A.1:

1. Load program (file of commands) for XYZ system controlling.
2. Save program.
3. Check whole program command by command if it is correct. If it is not correct write error message.
4. Quit XYZ.vi application.
5. Actual position of x, y, and z coordinate of stage position.
6. Name of actual loaded file of program.
7. Program list box is split into two columns. The label can be written into the left column and it can be used by GT (go to) command for jumping within the program. Right column contain commands which are going to be executed.
8. Change units from steps to micrometers and vice-versa. If units are changed it cause conversation of units in positions 5 and as well in all arguments of command in program which are related.
9. Execute a command at an actual position of cursor and move the cursor to next command (except GT command which cause program jump).
10. Execute a command by command until and of program or if *Stop* button (11) is pressed.

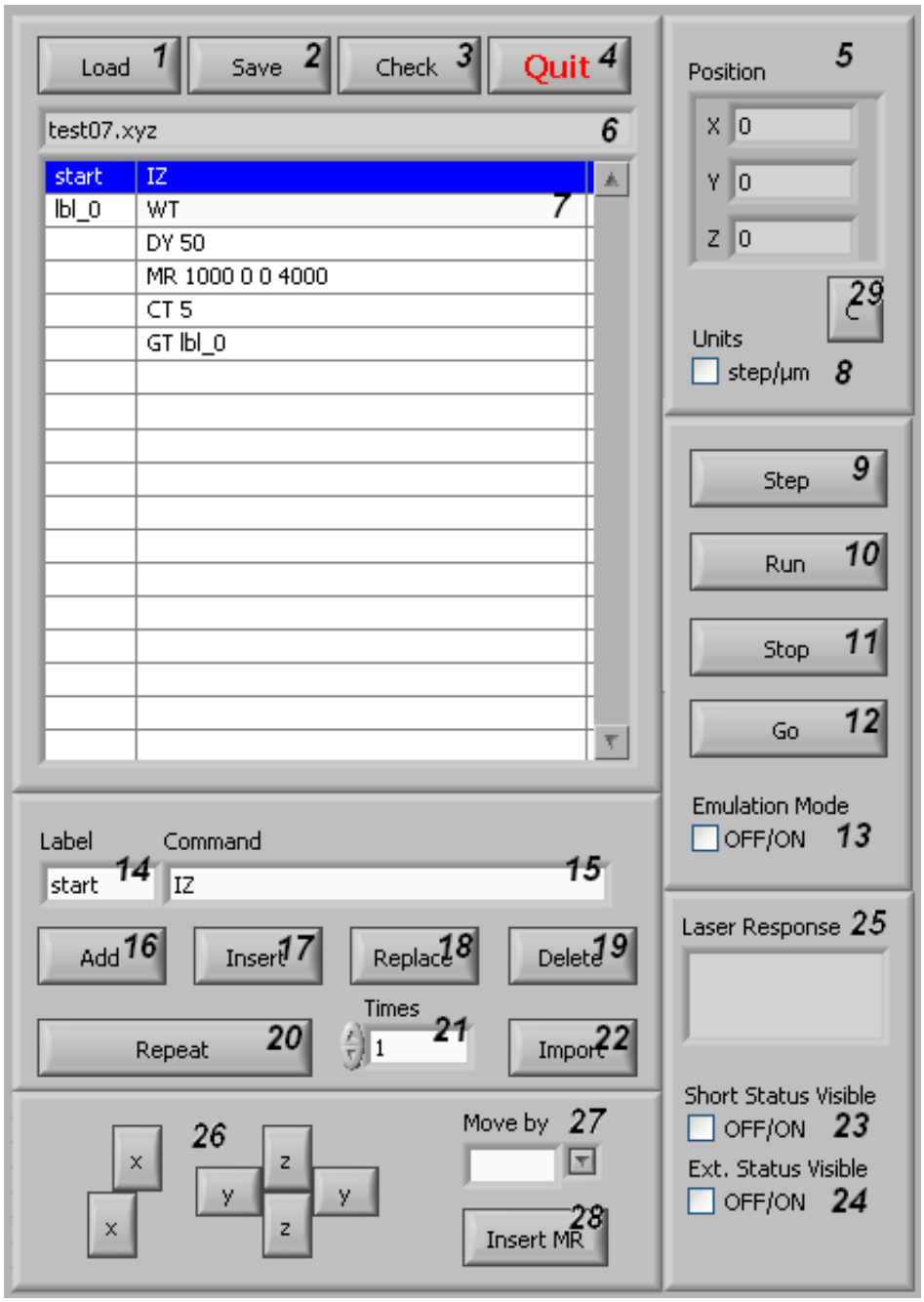

Figure A.1: Main application window

11. Stop execution of the program when it runs in that way that the command currently in execution will be finished.

12. Continue execution of program if it stops because of command WB (wait for button). Text on the button is red when this event occurs.

13. Switch on emulation mode of program execution behaviour. All commands which would be send to driver of motor via RS422 will be emulated and not really executed. Additionally 3D graph will be show with simulated moving of stage (fig.A.2).

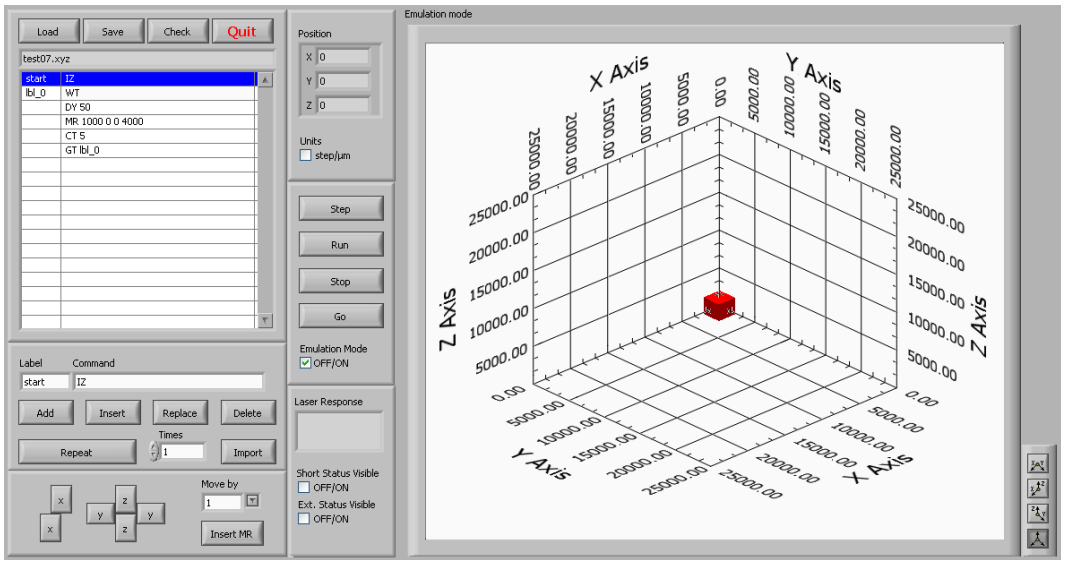

Figure A.2: Program in test mode.

14. Text box for editing actual label.

15. Text box for editing actual command.

16. Add new line after actual position of cursor and make it editable in command text box 15. *Ctrl + Enter* short cut can be used when you are in label or command text box (14, 15) with same effect.

17. Add new line before actual position of cursor and make it editable in command text box 16. *Shift + Enter* short cut can be used when you are in label or command text box (14, 15) with same effect.

18. Replace the label and the command in program list box 7 at actual position with that in the label and the command text boxes (14, 15).

19. Delete actual line in program list box 7.

20. Insert loop into program for part of program which is highlighted by cursor by using *Shift + mouse click* selection see fig.A.3. In text box 21 chose number of repeating for loop.

21. Number of loop repeating created from part of program by button 20.

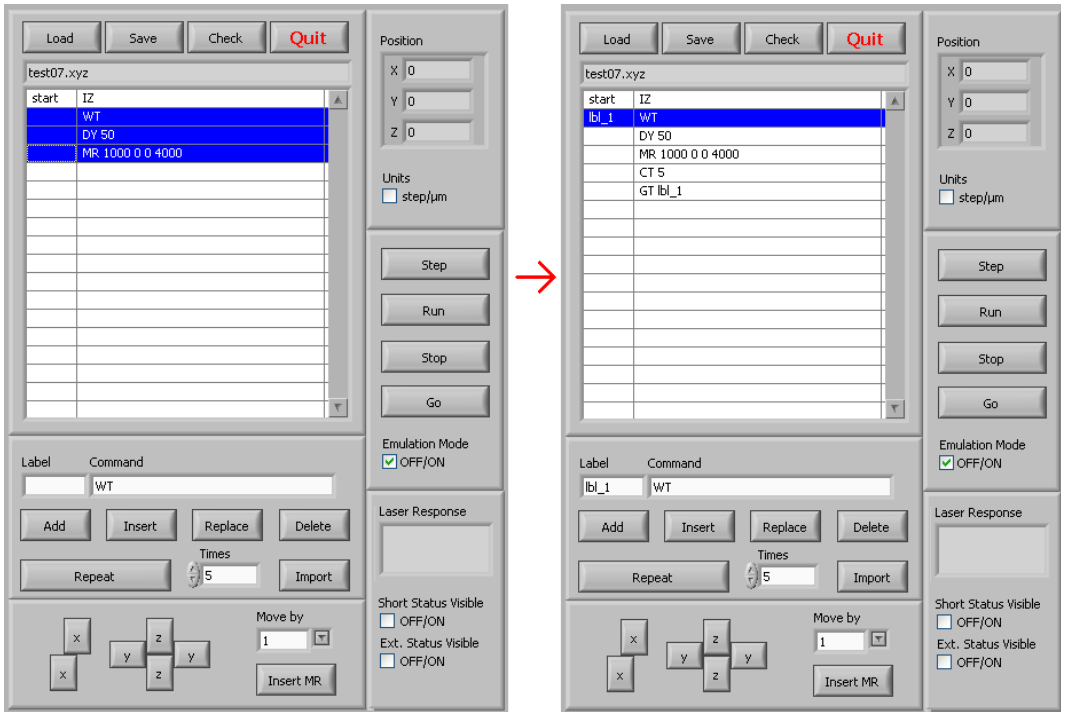

Figure A.3: Loops creating.

22. Import the coordinates and the velocity from ASCI file to the program converted to MR command. File has to be in such format that all lines contains x, y , z and speed separated by space or tab. For example line from file 1000 200 3000 1000 will be converted to MR 1000 200 3000 1000 (fig.A.4).

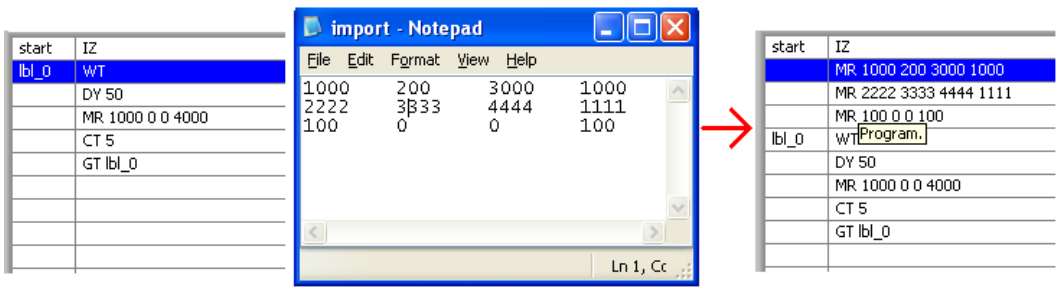

Figure A.4: Importing of coordinates from a text file.

23. Show short status of X, Y, Z, drivers (fig.A.5).

24. Show extended status of X, Y, Z, drivers (fig.A.5).

25. Response of laser to command.

26. Buttons for manual moving of stage. After click on button stage will move by number of steps which are defined by 27.

27. See 26.

28. Insert MR command to Program list box to cursor position. Coordinated in the command will be same as in 5. and velocity parameter will be 300.

29. Clear 5. to zero values.

Command **IZ (initialize)**

Syntax: IZ

Description: Go to zero position.

Example: `IZ`

Command **MR (move relatively)**

Syntax: MR arg_x arg_y arg_z arg_s

Description: Is used as order for relative moving from actual position. First three arguments are coordinates (X, Y and Z in order as they are) and last one is a speed of moving for these coordinates. Units of arguments are in steps or μm with respect to check box 8 on fig.A.1.

Example: `MR 1000 2000 0 1500`

Command **DY (delay)**

Syntax: DY arg

Description: Wait arg microseconds and go to next command. arg has to be integer.

Example: `DY 100`

Command **WB (wait for button)**

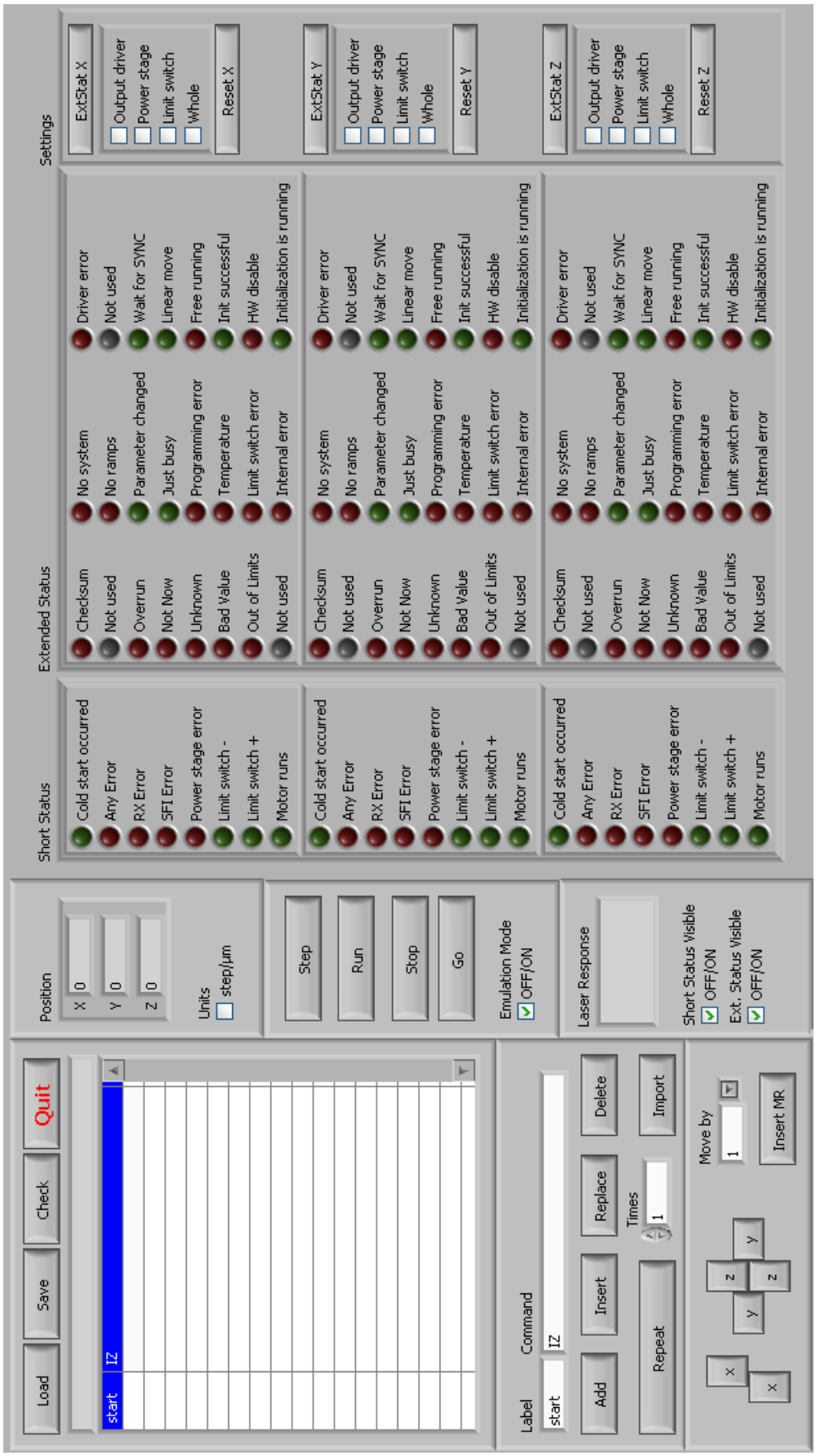

Figure A.5: Status panel.

Syntax: WB

Description: Program stops and is waiting until button 12 figure.1. is pressed. Until it's waiting button has red label *Go*.

Example: `WB`

Command **WT (wait for trigger)**

Syntax: WT

Description: Program stops and is waiting until trigger event will occur. That means rising edge of TTL signal on input of DAQ card.

Example: `WT`

Command **GT (go to)**

Syntax: GT arg

Description: Program jumps from actual line to line marked with label arg.

Example:
```
. . . . . .
. . . . . .
lbl_0 MR 100 0 0 200
GT lbl_0
. . . . . .
. . . . . .
```

Command **CT (counter)**

Syntax: CT arg

Description: It increments arg by 1 and goes to command at next line. If arg has value 1 it resets it to its initial value (before its first execution), skips the next command and continues execution after the skipped command.

Example:
```
. . . . . .
. . . . . .
lbl_0 MR 100 0 0 200
CT 10
GT lbl_0
MR 0 0 100 100
```

```
. . . . . .
```

Command **$1 (BigSky laser command)**

Syntax: $1 arg

Description: It sends BigSky laser's command to RS232 and it will wait to laser response. Response will be written to text box 25. (fig.A.1) and program will continue to next command. The BigSky laser's commands are described in BigSky laser manual.

Example:

```
. . . . . .
. . . . . .
MR 2800 2500 10600 300
$1 LPM0
$1 F1000
$1 ASM0
$1 QSF1
$1 VQ-20
$1 A
MR 800 500 1000 300
. . . . . .
```

Appendix B

Manual for portable LIBS software

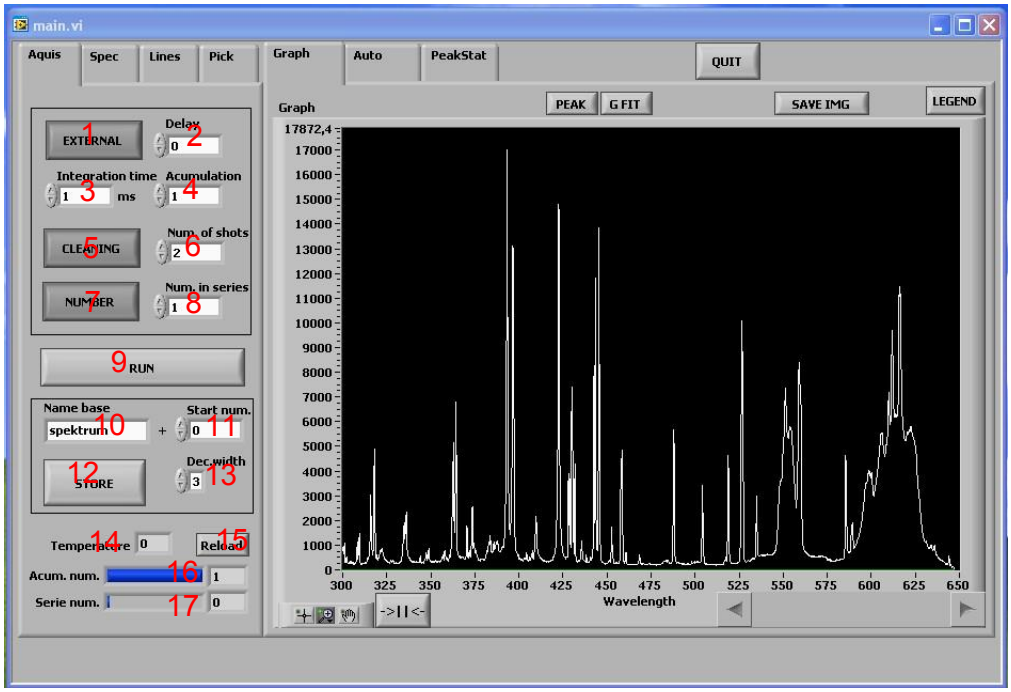

Figure B.1: Acquisition tabulator

Acquisition tabulator fig.B.1:

1. External or internal trigger.
2. Delay after trigger event in ms.
3. Integration time in ms.

4. Accumulation number.
5. Cleaning shots ON/OFF.
6. Number of cleaning shots (will be not stored)
7. Continuous or series mode.
8. Number of series (series mode have to be chosen).
9. Run or stop acquisition.
10. Name of acquired spectra.
11. Spectra counter (is appended to spectra name).
12. Store last acquired spectra (will be loaded to Spectra tabulator).
13. Width of counter 11.
14. Temperature of the spectrometer.
15. Reload spectrometer's temperature.
16. Actual accumulation number.
17. Actual series number.

Spectra tabulator fig.B.2:

1. List of loaded spectra.
2. Show or hide selected spectra on the graph.
3. Select all spectra in the list box.
4. Normalize selected spectra to spectra intensity.
5. Normalize selected spectra to yellow cursor position.
6. Open spectra.
7. Delete selected spectra.
8. Save selected spectra.

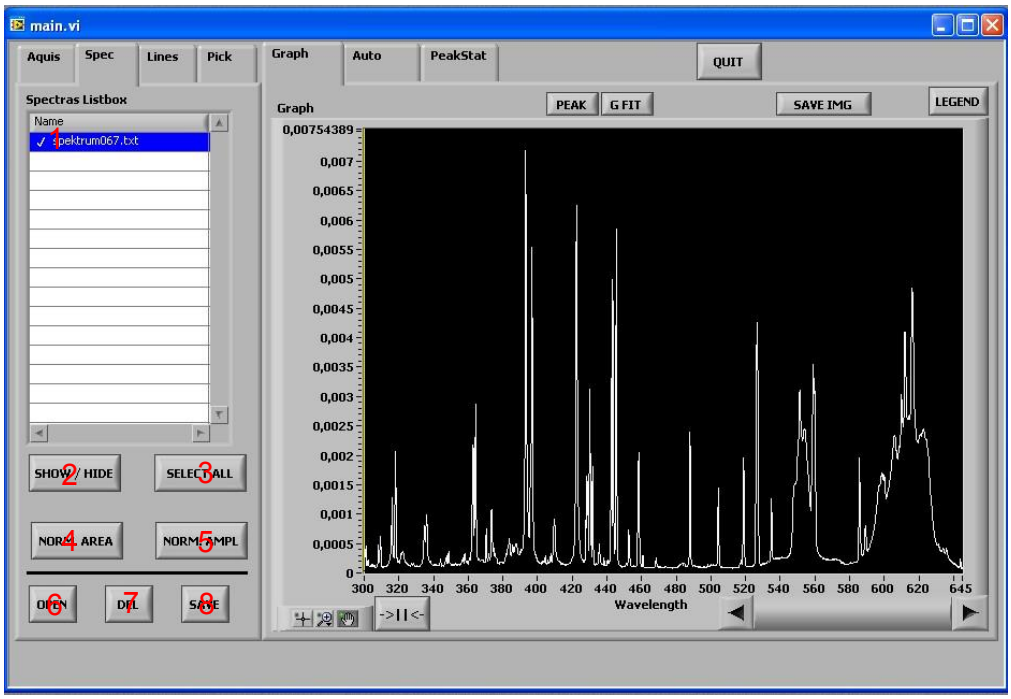

Figure B.2: Spectra tabulator

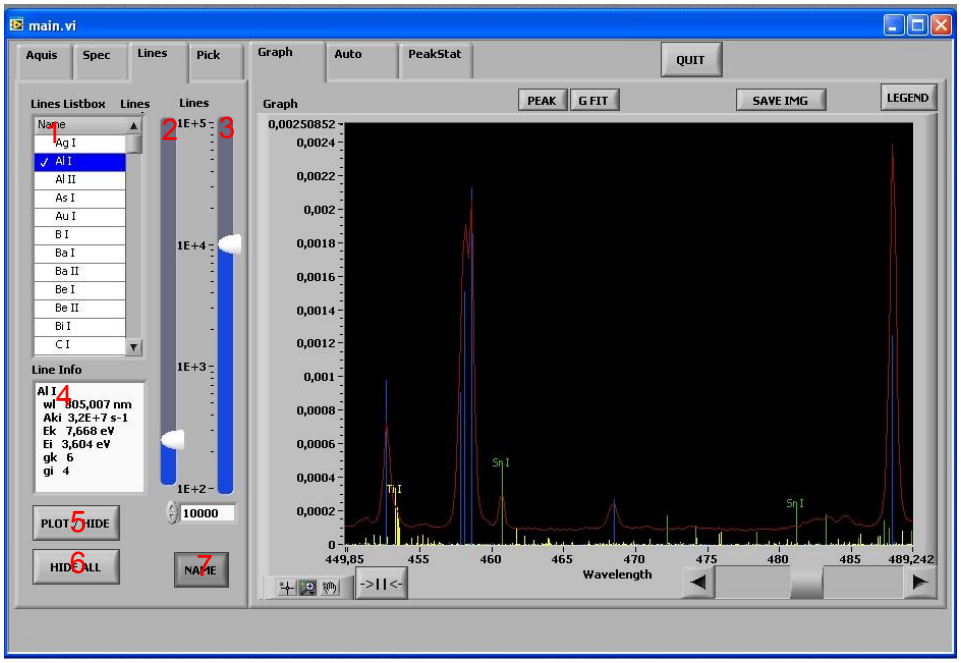

Figure B.3: Lines tabulator

Lines tabulator fig.B.3:

1. List of atomic lines for different element.
2. Scale of actual selected element lines.
3. Temperature Boltzmann distribution.
4. Spectroscopic data of selected line.
5. Hide or show selected element lines on the graph.
6. Hide all element lines shown on the graph.
7. Name 10 most intensive shown lines for each element.

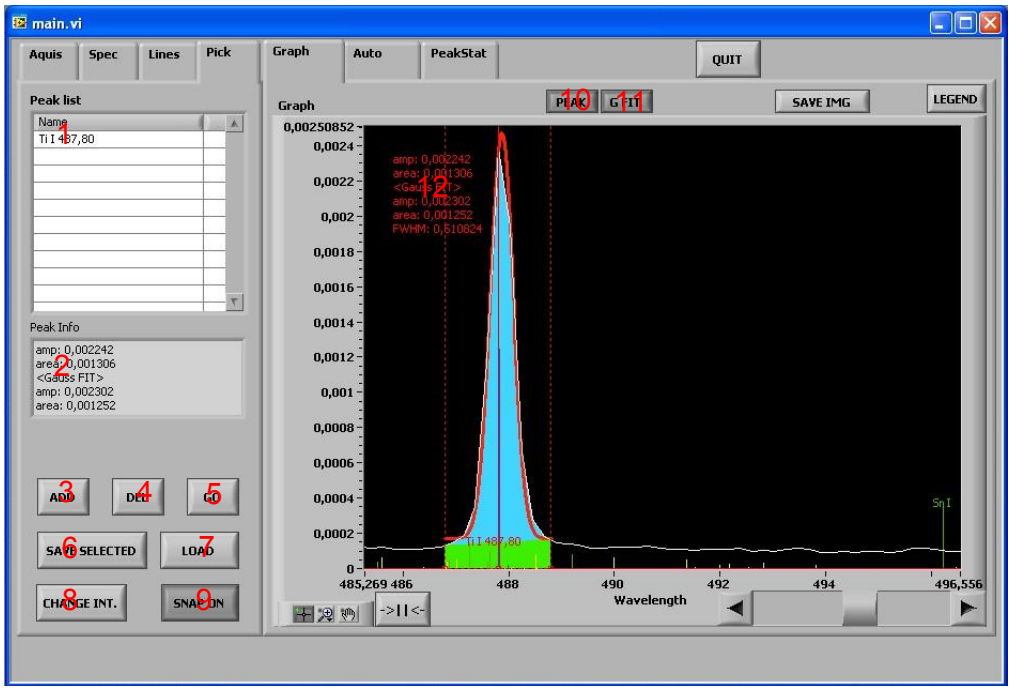

Figure B.4: Pick tabulator

Pick tabulator fig.B.4:

1. List of presented peaks.
2. Information about the fit.
3. Add selected peak from graph.
4. Delete selected peak from list box.

5. Show selected peak from list box on the graph.
6. Save selected peak with data.
7. Load peaks.
8. Chance peak interval.
9. Snap on displayed element lines selected in the Lines tabulator.
10. Calculate area of selected peak.
11. Fit selected peak by Gauss profile (later extended to Lorentz and Voigt profile).
12. Information abut fit.

Figure B.5: Auto tabulator

Auto tabulator fig.B.5:

1. Indication panel for automatically detected element line.
2. Duplicate of 1.
3. Setup for search criteria for automatic line detection.

4. Duplicate of 3 for setup related to panel 2.
5. Scroll panel up.
6. Scroll panel down.
7. Show detected line in the graph.

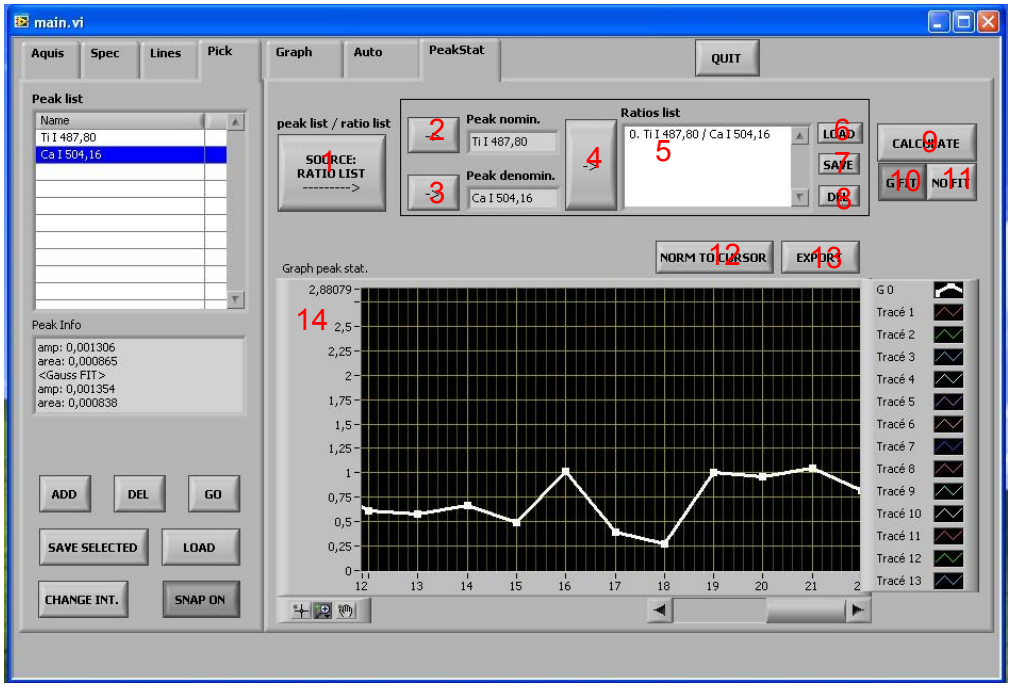

Figure B.6: Peak statistic tabulator

Peak statistic tabulator fig.B.6:

1. Switch for source list selection for used peaks.
2. Add selected peak to nominator.
3. Add selected peak to denominator.
4. Add ratio to list.
5. List of ratios.
6. Load ratios.
7. Save ratios.
8. Delete ratios.

9. Calculate evolution selected peaks or for selected ratios.
10. Calculations will be performed for fit.
11. Calculations will be performed for area determination.
12. Normalize evolution to selected position.
13. Export evolutions.
14. Screen to show calculated evolutions.

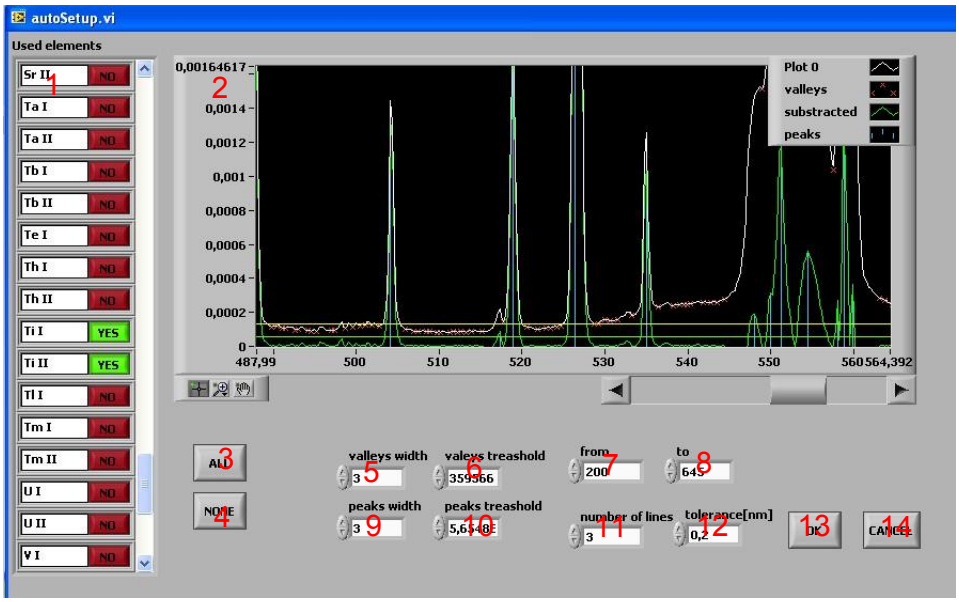

Figure B.7: Window for automatic line detection settings

Window for automatic line detection settings fig.B.7:

1. List of elements included in automatic line detection.
2. Screen for indicating of fond peaks in the spectra.
3. Select all elements from list.
4. Select none element form list.
5. Width of valleys (in points).
6. Valleys threshold.
7. Global setting for spectral range used by program.

8. Global setting for spectral range used by program.
9. Width of peaks (in points).
10. Peaks threshold.
11. Number of most intensive lines which will be detected for selected elements.
12. Tolerance for interval in nm to consider line as detected.
13. Save settings.
14. Cancel settings.

Bibliography

[1] LIFBASE 2.0. http://www.sri.com/psd/lifbase.

[2] Applied Photonics LIBSCAN 25. http://www.appliedphotonics.co.uk.

[3] J A Aguilera and C Aragón. Apparent excitation temperature in laser-induced plasmas. *Journal of Physics: Conference Series*, 59(1):210, 2007.

[4] J.A Aguilera and C. Aragón. Characterization of a laser-induced plasma by spatially resolved spectroscopy of neutral atom and ion emissions.: Comparison of local and spatially integrated measurements. *Spectrochimica Acta Part B: Atomic Spectroscopy*, 59(12):1861 – 1876, 2004.

[5] J.A Aguilera and C. Aragón. Multi-element saha-boltzmann and boltzmann plots in laser-induced plasmas. *Spectrochimica Acta Part B: Atomic Spectroscopy*, 62(4):378 – 385, 2007.

[6] J.A. Aguilera, C. Aragón, G. Cristoforetti, and E. Tognoni. Application of calibration-free laser-induced breakdown spectroscopy to radially resolved spectra from a copper-based alloy laser-induced plasma. *Spectrochimica Acta Part B: Atomic Spectroscopy*, 64(7):685 – 689, 2009.

[7] Hssaine Amamou, Andre Bois, Belkacem Ferhat, Roland Redon, Bruno Rossetto, and Marc Ripert. Correction of the self-absorption for reversed spectral lines: application to two resonance lines of neutral aluminium. *Journal of Quantitative Spectroscopy and Radiative Transfer*, 77(4):365 – 372, 2003.

[8] C. Aragón and J.A. Aguilera. Characterization of laser induced plasmas by optical emission spectroscopy: A review of experiments and methods. *Spectrochimica Acta Part B: Atomic Spectroscopy*, 63(9):893 – 916, 2008.

[9] N. Arnold, J. Gruber, and J. Heitz. Spherical expansion of the vapor plume into ambient gas: an analytical model. *Applied Physics A: Materials Science & Processing*, 69:S87–S93, 1999.

[10] George Asimellis, Aggelos Giannoudakos, and Michael Kompitsas. Phosphate ore beneficiation via determination of phosphorus-to-silica ratios by laser induced breakdown spectroscopy. *Spectrochimica Acta Part B: Atomic Spectroscopy*, 61(12):1253 – 1259, 2006.

[11] V.I. Babushok, F.C. DeLucia Jr., J.L. Gottfried, C.A. Munson, and A.W. Miziolek. Double pulse laser ablation and plasma: Laser induced breakdown spectroscopy signal enhancement. *Spectrochimica Acta Part B: Atomic Spectroscopy*, 61(9):999 – 1014, 2006.

[12] G. Baravian, J. Godart, and G. Sultan. Multiphoton ionization of molecular nitrogen by a neodymium-glass laser. *Phys. Rev. A*, 25:1483–1495, Mar 1982.

[13] R Barbini, F Colao, V Lazic, R Fantoni, A Palucci, and M Angelone. On board libs analysis of marine sediments collected during the xvi italian campaign in antarctica. *Spectrochimica Acta Part B: Atomic Spectroscopy*, 57(7):1203 – 1218, 2002.

[14] N Bibinov, H Halfmann, P Awakowicz, and K Wiesemann. Relative and absolute intensity calibrations of a modern broadband echelle spectrometer. *Measurement Science and Technology*, 18(5):1327, 2007.

[15] Annemie Bogaerts and Renaat Gijbels. Fundamental aspects and applications of glow discharge spectrometric techniques. *Spectrochimica Acta Part B: Atomic Spectroscopy*, 53(1):1 – 42, 1998.

[16] G. Bossuet, H. Richard, M. Magny, and M. Rossy. Nouvelle occurrence du laacher see tephra dans le jura central. etang du lautrey (france). *Comptes Rendus de l'Academie des Sciences*, 325:43 – 48, 1997.

[17] Paul v.d. Bougaard and Hans-Ulrich Schmincke. Laacher see tephra: A widespread isochronous late quaternary tephra layer in central and northern europe. *Geological Society of America Bulletin*, 96(12):1554–1571, December, 1985.

[18] F. Brech and L. Cross. Optical microemission stimulated by a ruby laser. *Appl. Spectrosc.*, 16:59, 1962.

[19] F. Bredice, F.O. Borges, H. Sobral, M. Villagran-Muniz, H.O. Di Rocco, G. Cristoforetti, S. Legnaioli, V. Palleschi, L. Pardini, A. Salvetti, and E. Tognoni. Evaluation of self-absorption of manganese emission lines

in laser induced breakdown spectroscopy measurements. *Spectrochimica Acta Part B: Atomic Spectroscopy*, 61(12):1294 – 1303, 2006.

[20] N Britun, M Gaillard, A Ricard, Y M Kim, K S Kim, and J G Han. Determination of the vibrational, rotational and electron temperatures in n2 and ar-n2 rf discharge. *Journal of Physics D: Applied Physics*, 40(4):1022, 2007.

[21] D Bulajic, M Corsi, G Cristoforetti, S Legnaioli, V Palleschi, A Salvetti, and E Tognoni. A procedure for correcting self-absorption in calibration free-laser induced breakdown spectroscopy. *Spectrochimica Acta Part B: Atomic Spectroscopy*, 57(2):339 – 353, 2002.

[22] Kiris V.V. Naumenkov P.A. Raikov S.N. Burakov, V.S. Calibration-free laser spectral analysis of glasses and copper alloys. *Journal of Applied Spectroscopy*, 71(5):740–746, 2004.

[23] A. Ciucci, M. Corsi, V. Palleschi, S. Rastelli, A. Salvetti, and E. Tognoni. New procedure for quantitative elemental analysis by laser-induced plasma spectroscopy. *Appl. Spectrosc.*, 53(8):960–964, Aug 1999.

[24] F. Colao, R. Fantoni, P. Ortiz, M.A. Vazquez, J.M. Martin, R. Ortiz, and N. Idris. Quarry identification of historical building materials by means of laser induced breakdown spectroscopy, x-ray fluorescence and chemometric analysis. *Spectrochimica Acta Part B: Atomic Spectroscopy*, 65(8):688 – 694, 2010.

[25] A. Cousin, O. Forni, S. Maurice, O. Gasnault, C. Fabre, V. Sautter, R.C. Wiens, and J. Mazoyer. Laser induced breakdown spectroscopy library for the martian environment. *Spectrochimica Acta Part B: Atomic Spectroscopy*, 66(11–12):805–814, 2011.

[26] D.A. Cremers and L.J. Radziemski. *Handbook of laser-induced breakdown spectroscopy*. John Wiley, 2006.

[27] David A. Cremers. The analysis of metals at a distance using laser-induced breakdown spectroscopy. *Appl. Spectrosc.*, 41(4):572–579, May 1987.

[28] David A. Cremers, Monty J. Ferris, and Mathew Davies. Transportable laser-induced breakdown spectroscopy (libs) instrument for field-based soil analysis. *Proc. SPIE*, 2835:190 – 200, 1996.

[29] G. Cristoforetti, A. De Giacomo, M. Dell'Aglio, S. Legnaioli, E. Tognoni, V. Palleschi, and N. Omenetto. Local thermodynamic equilibrium in laser-induced breakdown spectroscopy: Beyond the mcwhirter criterion. *Spectrochimica Acta Part B: Atomic Spectroscopy*, 65(1):86 – 95, 2010.

[30] G. Cristoforetti, G. Lorenzetti, S. Legnaioli, and V. Palleschi. Investigation on the role of air in the dynamical evolution and thermodynamic state of a laser-induced aluminium plasma by spatial- and time-resolved spectroscopy. *Spectrochimica Acta Part B: Atomic Spectroscopy*, 65(9 - 10):787 – 796, 2010.

[31] E. K. Damon and R. G. Tomlinson. Observation of ionization of gases by a ruby laser. *Appl. Opt.*, 2(5):546–546, May 1963.

[32] C.M. Davies, H.H. Telle, D.J. Montgomery, and R.E. Corbett. Quantitative analysis using remote laser-induced breakdown spectroscopy (libs). *Spectrochimica Acta Part B: Atomic Spectroscopy*, 50(9):1059 – 1075, 1995.

[33] Jr. DeLucia, F.C., A.C. Samuels, R.S. Harmon, R.A. Walters, K.L. McNesby, A. LaPointe, Jr. Winkel, R.J., and A.W. Miziolek. Laser-induced breakdown spectroscopy (libs): a promising versatile chemical sensor technology for hazardous material detection. *Sensors Journal, IEEE*, 5(4):681 – 689, aug. 2005.

[34] H. W. Drawin. Validity conditions for local thermodynamic equilibrium. *Zeitschrift für Physik A Hadrons and Nuclei*, 228:99–119, 1969.

[35] M. Darby Dyar, Jonathan M. Tucker, Seth Humphries, Samuel M. Clegg, Roger C. Wiens, and Melissa D. Lane. Strategies for mars remote laser-induced breakdown spectroscopy analysis of sulfur in geological samples. *Spectrochimica Acta Part B: Atomic Spectroscopy*, 66(1):39 – 56, 2011.

[36] Andrew J. Effenberger and Jill R. Scott. Effect of atmospheric conditions on libs spectra. *Sensors*, 10(5):4907–4925, 2010.

[37] Kristine L. Eland, Dimitra N. Stratis, J. C. Carter, and S. M. Angel. Development of a dual-pulse fiber optic libs probe for in-situ elemental analyses. *Environmental Monitoring and Remediation Technologies II*, 3853(1):288–294, 1999.

[38] C. Fabre, S. Maurice, A. Cousin, R.C. Wiens, O. Forni, V. Sautter, and D. Guillaume. Onboard calibration igneous targets for the mars science laboratory curiosity rover and the chemistry camera laser induced breakdown spectroscopy instrument. *Spectrochimica Acta Part B: Atomic Spectroscopy*, 66(3–4):280 – 289, 2011.

[39] M. Ferretti, G. Cristoforetti, S. Legnaioli, V. Palleschi, A. Salvetti, E. Tognoni, E. Console, and P. Palaia. In situ study of the porticello bronzes by portable x-ray fluorescence and libs. *Spectrochim. Acta Part B*, 62:1512–1518, 2007.

[40] L. Fornarini, F. Colao, R. Fantoni, V. Lazic, and V. Spizzicchino. Calibration analysis of bronze samples by nanosecond laser induced breakdown spectroscopy: A theoretical and experimental approach. *Spectrochimica Acta Part B: Atomic Spectroscopy*, 60(7–8):1186 – 1201, 2005.

[41] T. Fujimoto. *Plasma Spectroscopy*. International Series of Monographs on Physics. Clarendon Press, 2004.

[42] A. De Giacomo, M. Dell'Aglio, O. De Pascale, S. Longo, and M. Capitelli. Laser induced breakdown spectroscopy on meteorites. *Spectrochimica Acta Part B: Atomic Spectroscopy*, 62(12):1606 – 1611, 2007.

[43] Jennifer L. Gottfried, Frank C. De Lucia Jr., Chase A. Munson, and Andrzej W. Miziolek. Double-pulse standoff laser-induced breakdown spectroscopy for versatile hazardous materials detection. *Spectrochimica Acta Part B: Atomic Spectroscopy*, 62(12):1405 – 1411, 2007.

[44] J. Goujon, A. Giakoumaki, V. Pi non, O. Musset, D. Anglos, E. Georgiou, and J.P. Boquillon. A compact and portable laser-induced breakdown spectroscopy instrument for single and double pulse applications. *Spectrochimica Acta Part B: Atomic Spectroscopy*, 63(10):1091 – 1096, 2008.

[45] H.R. Griem. *Principles of plasma spectroscopy*. Cambridge Monographs on Plasma Physics. Cambridge University Press, 2005.

[46] Rasmus Grönlund, Mats Lundqvist, and Sune Svanberg. Remote imaging laser-induced breakdown spectroscopy and remote cultural heritage ablative cleaning. *Opt. Lett.*, 30(21):2882–2884, Nov 2005.

[47] R Harmon, F Delucia, C Mcmanus, N Mcmillan, T Jenkins, M Walsh, and A Miziolek. Laser-induced breakdown spectroscopy – an emerging chemical sensor technology for real-time field-portable, geochemical, mineralogical, and environmental applications. *Applied Geochemistry*, 21(5):730–747, 2006.

[48] Russell. S. Harmon, Frank C. De Lucia, Andrzej W. Miziolek, Kevin L. McNesby, Roy A. Walters, and Patrick D. French. Laser-induced breakdown spectroscopy (libs) – an emerging field-portable sensor technology for real-time, in-situ geochemical and environmental analysis. *Geochemistry: Exploration, Environment, Analysis*, 5(1):21–28, 2005.

[49] W.M. Haynes and D.R. Lide. *CRC Handbook of Chemistry and Physics*. CRC Handbook of Chemistry and Physics. Taylor & Francis, 2011.

[50] T. Ida, M. Ando, and H. Toraya. Extended pseudo-Voigt function for approximating the Voigt profile. *Journal of Applied Crystallography*, 33(6):1311–1316, Dec 2000.

[51] IVEA. Easylibs, http://www.ivea-solution.com.

[52] Étienne Juvigné, Stefan Kozarski, and Boleslaw Nowaczyk. The occurrence of laacher see tephra in pomerania, nw poland. *Boreas*, 24(3):225–231, 1995.

[53] P. Kepple and Hans R. Griem. Improved stark profile calculations for the hydrogen lines Hα, Hβ, Hγ, and Hδ. *Phys. Rev.*, 173:317–325, Sep 1968.

[54] N. Konjevic. Plasma broadening and shifting of non-hydrogenic spectral lines: present status and applications. *Physics Reports*, 316(6):339 – 401, 1999.

[55] N. Konjevic and W. L. Wiese. Experimental stark widths and shifts for spectral lines of neutral and ionized atoms. *Journal of Physical and Chemical Reference Data*, 19(6):1307–1385, 1990.

[56] Bernd Kromer, Michael Friedrich, Konrad A Hughen, Felix Kaiser, Sabine Remmele, Matthias Schaub, and Sahra Talamo. Late glacial ^{14}c ages from a floating, 1382-ring pine chronology. *Radiocarbon*, 46(3):1203 – 1209, 2004.

[57] R.L. Kurucz. Atomic spectral line database, available at: http://www.cfa.harvard.edu/amp/ampdata/kurucz23/sekur.html.

[58] Bansi Lal, Hongbo Zheng, Fang-Yu Yueh, and Jagdish P. Singh. Parametric study of pellets for elemental analysis with laser-induced breakdown spectroscopy. *Appl. Opt.*, 43(13):2792–2797, May 2004.

[59] Neil H. Landman, K. Tanabe, and R.A. Davis. *Ammonoid Paleobiology*. Topics in Geobiology. Plenum Press, 1996.

[60] J. Lasue, R. Wiens, T. Stepinski, O. Forni, S. Clegg, S. Maurice, and . Nonlinear mapping technique for data visualization and clustering assessment of libs data: application to chemcam data. *Analytical and Bioanalytical Chemistry*, 400:3247–3260, 2011.

[61] V. Lednev and S. Pershin. Plasma stoichiometry correction method in laser-induced breakdown spectroscopy. *Laser Physics*, 18:850–854, 2008.

[62] Y.I. Lee, K. Song, and J. Sneddon. *Laser-induced breakdown spectrometry*. Nova Science Publishers, 2000.

[63] D. E. Lencioni. The effect of dust on 10.6 μm laser-induced air breakdown. *Applied Physics Letters*, 23(1):12–14, 1973.

[64] Peter Lindblom. New compact echelle spectrographs with multichannel time-resolved recording capabilities. *Analytica Chimica Acta*, 380:353–361, 1999.

[65] C. Lopez-Moreno, S. Palanco, and J. J. Laserna. Remote laser-induced plasma spectrometry for elemental analysis of samples of environmental interest. *J. Anal. At. Spectrom.*, 19(11):–, 2004.

[66] Dan MacIsaac, Gary Kanner, and Graydon Anderson. Basic physics of the incandescent lamp (lightbulb). *The Physics Teacher*, 37(9):520–525, 1999.

[67] T. H. MAIMAN. Stimulated optical radiation in ruby. *Nature*, 187(4736):493–494, August 1960.

[68] Brian J. Marquardt, Scott R. Goode, and S. Michael Angel. In situ determination of lead in paint by laser-induced breakdown spectroscopy using a fiber-optic probe. *Analytical Chemistry*, 68(6):977–981, 1996.

[69] Viktor Martišovitš. *Základy fyziky plazmy.* Univerzita Komenského Bratislava vo Vydavateľstve UK, 2004.

[70] Z. Marton, P. Heszler, A. Mechler, B. Hopp, Z. Kantor, and Z. Bor. Time-resolved shock-wave photography above 193-nm excimer laser-ablated graphite surface. *Applied Physics A-materials Science & Processing*, 69:S133–S136, December 1999.

[71] K.H. Meldahl. *1. Fossilized Materials - Shells. In Palaeobiology II.* Blackwell Science Ltd, Oxford, 2001.

[72] A.W. Miziolek, V. Palleschi, and I. Schechter. *Laser-induced breakdown spectroscopy (LIBS): fundamentals and applications.* Cambridge University Press, 2006.

[73] Heh-Young Moon, Kathleen K. Herrera, Nicoló Omenetto, Benjamin W. Smith, and J.D. Winefordner. On the usefulness of a duplicating mirror to evaluate self-absorption effects in laser induced breakdown spectroscopy. *Spectrochimica Acta Part B: Atomic Spectroscopy*, 64(7):702–713, 2009.

[74] J. Cu nat, F. J. Fortes, L. M. Cabalín, F. Carrasco, M. D. Simón, and J. J. Laserna. Man-portable laser-induced breakdown spectroscopy system for in situ characterization of karstic formations. *Appl. Spectrosc.*, 62(11):1250–1255, Nov 2008.

[75] National Institute of Standards and Technology. Atomic spectra database.

[76] National Institute of Standards and Technology. Ground levels and ionization energies for the neutral atoms.

[77] Ocean Optics. Hr2000+ http://www.oceanoptics.com/products /hr2000+.asp.

[78] Santiago Palanco, Cristina López-Moreno, and J. Javier Laserna. Design, construction and assessment of a field-deployable laser-induced breakdown spectrometer for remote elemental sensing. *Spectrochimica Acta Part B: Atomic Spectroscopy*, 61(1):88 – 95, 2006.

[79] Rai A.K. Pandhija, S. In situ multielemental monitoring in coral skeleton by cf-libs. *Applied Physics B: Lasers and Optics*, 94(3):545–552, 2009.

[80] Colao F. Spizzichino V. Pershin, S.M. Quantitative analysis of bronze samples by laser-induced breakdown spectroscopy (libs): A new approach, model, and experiment. *Laser Physics*, 16(3):455–467, 2006.

[81] SONY ILX51 2048 pixel CCD Linear Image Sensor (B/W). http://www.oceanoptics.com/technical/detectorsonyilx511.pdf.

[82] Applied Spectra PL100-GEO. http://www.appliedspectra.com.

[83] S D Popa. Vibrational distributions in a flowing nitrogen glow discharge. *Journal of Physics D: Applied Physics*, 29(2):411, 1996.

[84] B. Praher, V. Palleschi, R. Viskup, J. Heitz, and J.D. Pedarnig. Calibration free laser-induced breakdown spectroscopy of oxide materials. *Spectrochimica Acta Part B: Atomic Spectroscopy*, 65(8):671 – 679, 2010.

[85] William H. Press, Saul A. Teukolsky, William T. Vetterling, and Brian P. Flannery. *Numerical Recipes 3rd Edition: The Art of Scientific Computing*. Cambridge University Press, New York, NY, USA, 3 edition, 2007.

[86] L.J. Radziemski and D.A. Cremers. *Laser-induced plasmas and applications*. Optical engineering. M. Dekker, 1989.

[87] Awadhesh K Rai, Hansheng Zhang, Fang Yu Yueh, Jagdish P Singh, and Arel Weisburg. Parametric study of a fiber-optic laser-induced breakdown spectroscopy probe for analysis of aluminum alloys. *Spectrochimica Acta Part B: Atomic Spectroscopy*, 56(12):2371 – 2383, 2001.

[88] J. Rakovský, J. Krištof, P. Čermák, M. Kociánová, P. Veis, and O. Musset. Measurement of echelle spectrometer spectral response in UV. *WDS'11 Proceedings of Contributed Papers: Part III - Physics (eds. J. Safrankova and J. Pavlu), Prague, Matfyzpress*, pages 257–262, 2011.

[89] Sylvestre Maurice Roger C. Wiens and the ChemCam team. The chemcam instrument suite on the mars science laboratory rover curiosity: Remote sensing by laser-induced plasmas, 2011.

[90] S Rosenwasser, G Asimellis, B Bromley, R Hazlett, J Martin, T Pearce, and A Zigler. Development of a method for automated quantitative analysis of ores using libs. *Spectrochimica Acta Part B: Atomic Spectroscopy*, 56(6):707 – 714, 2001.

[91] B. Sallé, J.-L. Lacour, P. Mauchien, P. Fichet, S. Maurice, and G. Manhés. Comparative study of different methodologies for quantitative rock analysis by laser-induced breakdown spectroscopy in a simulated martian atmosphere. *Spectrochimica Acta Part B: Atomic Spectroscopy*, 61(3):301 – 313, 2006.

[92] Craig J. Sansonetti, Marc L. Salit, and Joseph Reader. Wavelengths of spectral lines in mercury pencil lamps. *Appl. Opt.*, 35(1):74–77, Jan 1996.

[93] A.M. El Sherbini, Th.M. El Sherbini, H. Hegazy, G. Cristoforetti, S. Legnaioli, V. Palleschi, L. Pardini, A. Salvetti, and E. Tognoni. Evaluation of self-absorption coefficients of aluminum emission lines in laser-induced breakdown spectroscopy measurements. *Spectrochimica Acta Part B: Atomic Spectroscopy*, 60(12):1573 – 1579, 2005.

[94] J.P. Singh and S.N. Thakur. *Laser-induced breakdown spectroscopy*. Elsevier, 2007.

[95] Jean-Baptiste Sirven, Beatrice Salle, Patrick Mauchien, Jean-Luc Lacour, Sylvestre Maurice, and Gerard Manhes. Feasibility study of rock identification at the surface of mars by remote laser-induced breakdown spectroscopy and three chemometric methods. *J. Anal. At. Spectrom.*, 22(12):1471–1480, 2007.

[96] Specair. http://www.specair-radiation.net.

[97] Lanxiang Sun and Haibin Yu. Correction of self-absorption effect in calibration-free laser-induced breakdown spectroscopy by an internal reference method. *Talanta*, 79(2):388 – 395, 2009.

[98] P. Thompson, D. E. Cox, and J. B. Hastings. Rietveld refinement of Debye–Scherrer synchrotron X-ray data from Al_2O_3. *Journal of Applied Crystallography*, 20(2):79–83, Apr 1987.

[99] A.P. Thorne, U. Litzén, and S. Johansson. *Spectrophysics: principles and applications*. Springer, 1999.

[100] E. Tognoni, G. Cristoforetti, S. Legnaioli, and V. Palleschi. Calibration-free laser-induced breakdown spectroscopy: State of the art. *Spectrochimica Acta Part B: Atomic Spectroscopy*, 65(1):1 – 14, 2010.

[101] E. Tognoni, G. Cristoforetti, S. Legnaioli, V. Palleschi, A. Salvetti, M. Mueller, U. Panne, and I. Gornushkin. A numerical study of expected accuracy and precision in calibration-free laser-induced breakdown spectroscopy in the assumption of ideal analytical plasma. *Spectrochimica Acta Part B: Atomic Spectroscopy*, 62(12):1287 – 1302, 2007.

[102] J.E. Touma, E.A. Oks, S. Alexiou, and A. Derevianko. Review of the advanced generalized theory for stark broadening of hydrogen lines in plasmas with tables. *Journal of Quantitative Spectroscopy and Radiative Transfer*, 65(1–3):543–571, 2000.

[103] J. Uebbing, J. Brust, W. Sdorra, F. Leis, and K. Niemax. Reheating of a laser-produced plasma by a second pulse laser. *Appl. Spectrosc.*, 45(9):1419–1423, Sep 1991.

[104] H. van Regemorter. Rate of collisional excitation in stellar atmospheres. *Astrophys. J.*, 136:906–915, 1962.

[105] R.T Wainner, R.S Harmon, A.W Miziolek, K.L McNesby, and P.D French. Analysis of environmental lead contamination: comparison of libs field and laboratory instruments. *Spectrochimica Acta Part B: Atomic Spectroscopy*, 56(6):777 – 793, 2001.

[106] A.-V. Walter-Simonnet, G. Bossuet, C. Develle, A.L.and Bégeot, P. Ruffaldi, M. Magny, T. Adatte, M. Rossy, J.P. Simonnet, J.L. de Beaulieu, B. Vannière, M. Thivet, L. Millet, B. Regent, and C. Wackenheim. Chronologie et spatialisation des retombées de cendres volcaniques tardiglaciaires dans les massifs des vosges et du jura et le plateau suisse. *Quaternaire*, 19:117 – 132, 2008.

[107] Official web site of NASA's project ChemCam. http://www.msl-chemcam.com, 2012.

[108] G.E.G. Westermann. *The Jurassic of the Circum-Pacific*. World And Regional Geology. Cambridge University Press, 2005.

[109] A.I. Whitehouse, J. Young, I.M. Botheroyd, S. Lawson, C.P. Evans, and J. Wright. Remote material analysis of nuclear power station steam generator tubes by laser-induced breakdown spectroscopy. *Spectrochimica Acta Part B: Atomic Spectroscopy*, 56(6):821 – 830, 2001.

[110] StellarNet Inc. Tampa Florida USA Will Pierce, Sean M. Christian. Portable libs instrumentation can identify trace levels of environmental pollutants., 2005.

[111] Karen Y. Yamamoto, David A. Cremers, Monty J. Ferris, and Leeann E. Foster. Detection of metals in the environment using a portable laser-induced breakdown spectroscopy instrument. *Appl. Spectrosc.*, 50(2):222–233, Feb 1996.